10-1-2011

Photon manipulation in silicon nanophotonic circuits

Ali Elshaari

PHOTON MANIPULATION IN SILICON NANOPHOTONIC CIRCUITS

by

ALI WANIS ELSHAARI

A DISSERTATION

Submitted in partial fulfillment for the requirements
For the degree of Doctor of Philosophy
in
Microsystems Engineering
at the
Rochester Institute of Technology

Oct 2011

Author:
_____
Microsystems Engineering Program

Certified by:
_____
Stefan F. Preble, Ph.D.
Assistant Professor of Microsystems Engineering

Approved by:
_____
Bruce W. Smith, Ph.D.
Director of Microsystems Engineering Program

Certified by:
_____
Harvey J. Palmer, Ph.D.
Dean, Kate Gleason College of Engineering

NOTICE OF COPYRIGHT

REPRODUCITON PERMISSION STATEMENT

Permission Granted

TITLE:

"Photon Manipulation in Silicon Nanophotonic Circuits"

I, *Ali Wanis Elshaari*, hereby grant permission to the Wallace Library of Rochester Institute of Technology to reproduce my dissertation in whole or part. Any reproduction will not be for commercial use or profit.

Signature of Author: _____ Date:_____

PHOTON MANIPULATION IN SILICON NANOPHOTONIC CIRCUITS

By

Ali Wanis Elshaari

Submitted by Ali Wanis Elshaari in partial fulfillment of the requirements for the degree of Doctor of Philosophy in Microsystems Engineering and accepted on behalf of the Rochester Institute of Technology by the dissertation committee.

We, the undersigned members of the Faculty of the Rochester Institute of Technology, certify that we have advised and/or supervised the candidate on the work described in this dissertation. We further certify that we have reviewed the dissertation manuscript and approve it in partial fulfillment of the requirements of the degree of Doctor of Philosophy in Microsystems Engineering.

Dr. Stefan F. Preble _____
(Committee Chair and Dissertation Advisor)

Dr. Seth Hubbard _____

Dr. Jayanti Venkataraman _____

Dr. Zhaolin Lu _____

Dr. Bruce W. Smith _____
(Director, Microsystems Engineering)

Dr. Harvey J. Palmer _____
(Dean, Kate Gleason College of Engineering)

MICROSYSTEMS ENGINEERING PROGRAM
ROCHESTER INSTITUTE OF TECHNOLOGY

ABSTRACT

Kate Gleason College of Engineering
Rochester institute of Technology

Degree Doctor of Philosophy **Program** Microsystems Engineering

Name of Candidate Ali Wanis Elshaari

Title Photon Manipulation in Silicon Nanophotonic Circuits

Quantum-based communication systems can potentially achieve the ultimate security from eavesdropping and greatly reduce the operating powers on chip. Light-speed transmission, noise immunity, and low noise properties make photons indispensable for quantum communication to transfer a quantum state through a transmission line. Furthermore, the field of silicon nanophotonics is fast growing field which is driven by the attractive and promising improvements it has to offer in high speed communication systems and on chip optical interconnects. Consequently, there is a high demand to develop the building blocks for photon manipulation in silicon nanophotonic circuits.
The goal of the work is to enable high performance optoelectronic computing and communication systems that overcome the barriers of electronics and dramatically enhance the performance of circuits and systems. We will focus our attention on solving some of the issues with the current systems regarding photon storage, routing, isolation, switching, and energy conversion. We realize a continuously tunable optical memory which breaks the time-bandwidth limit by more than thirty times. This enabled the storage of ultra-short pulses of light for hundreds of picoseconds. Also, we investigate on-chip photon scattering when transmitted through micro-scale optical cavities. In addition, we develop novel dynamic quantum mechanical models that predict quantum-like behavior of single and multi-photon wavepackets.
Furthermore, we report for the first time that efficient red shifts in silicon are achievable with free carrier injection which generally produces blue wavelength shifts. We realize adiabatic wavelength conversion and discrete photonic transitions of single photons in silicon cavities. Moreover, we demonstrate a basic quantum network on chip with an on-chip photon source. We present a novel design for CMOS compatible optical isolator on silicon chip using a system of active cavities. And finally, we analyze a novel ultra-fast broadband modulator in silicon based on free-carrier absorption effect in SOI waveguides integrated with Schottky diodes.

Abstract Approval: Committee Chair _____

Program Director _____

Dean KGCOE _____

To my mother, father, Brother and his family

ACKNOWLEDGEMENTS

I would like to express my gratitude to Allah (God) for providing me the blessings to complete this work. You have given me the power to believe in my passion and pursue my dreams. I could never have done this without the faith I have in you, the Almighty.

I submit my highest appreciation to my advisor Dr. Stefan Preble for his guidance, understanding, patience, and most importantly, his friendship during my graduate studies at RIT. His mentorship was paramount in providing a well rounded experience. He encouraged me to not only grow as an experimentalist and an engineer but also as an instructor and an independent thinker. I am not sure many graduate students are given the opportunity to develop their own individuality and self-sufficiency by being allowed to work with such independence. His warm, enthusiastic demeanor along with infinite patience has made it an immense pleasure to conduct my research with him. For everything you've done for me, Dr. Preble, I thank you.

I would like to express my sincere gratitude to Dr. Edwin Hach. He is one of the best trained physicist/mathematician (and the funniest too) I have worked with. I fell in love with quantum optics and theoretical physics in general after collaborating with him to solve the photon transport problem.

I would like to thank Dr. Mustafa Abushagur for introducing me to RIT and the program of Microsystems. I thank him for his guidance; he was like a father to me during the time I spent at RIT.

I would like to acknowledge my dissertation committee members, Professor Seth Hubbard, Professor Jayanti Venkataraman, Professor Zhaolin Lu and Professor Bruce Smith for taking their time to assess my progress through the dissertation process. I also thank Sharon Stevens for keeping a watchful eye over my administrative responsibilities.

To the RIT Nanophotonics Group members: Abdelsalam Aboketaf, Liang Cao, and Karthik Narayanan. I would like to express my gratitude for fostering a cordial, friendly and vibrant atmosphere in the group.

To my mother, I dedicate this thesis to you. I express my most sincere appreciation for all that you have done for me. I was never able to finish this without your support and prayers. May Allah bless you.

To my father, I thank him for guiding me, instilling in me the value of education, believing in my abilities and being patient during the time we spent together. I ask Allah to have mercy on his soul, and I hope I fulfilled his dream by becoming a professor.

Finally, I thank my brother and his family for their support.

TABLE OF CONTENTS

LIST OF FIGURES

THESIS ORGANIZATION

Chapter 1: review of silicon photonics is provided with emphasis on traveling wave cavities and their simulation methods.

Chapter 2: a fully quantum mechanical study of steady state and dynamic single photon-cavity interaction is provided with experimental demonstration of photon interference and generation of photon pairs.

Chapter 3: full theoretical analysis of photon eigenenergy state manipulation with experimental demonstration of adiabatic shifts and discrete transitions.

Chapter 4: proposal, analysis, and experimental demonstration of photonic memory on chip using EIT like system.

Chapter 5: theoretical and numerically analysis of controlling transitions in a molecule-like photonic structure.

Chapter 6: proposal and numerical analysis of an optical isolator using a system of active cavities to break the time reversibility.

Chapter 7: analysis of a novel broadband photon switch by integrating Schottky diodes with silicon wires.

Chapter 8: concludes the dissertation and states major contributions along with future direction.

CHAPTER ONE

INTRODUCTION

1.1 Silicon Photonics Overview

Quantum-based Silicon photonic communication systems can potentially achieve the ultimate security from eavesdropping and greatly reduce the operating powers. Light speed transmission, noise immunity, and low noise properties make photons indispensable for quantum communication to transfer a quantum state through a transmission line. As a result, more work needs to done to develop the building blocks for photon manipulation in silicon nanophotonic circuits. This is also driven by the attractive and promising improvements this field has to offer in high speed communication systems and on chip optical interconnects. Silicon has been the main platform for electronic integrated circuits due to its desirable electronic properties, high isolation of its native oxide, low cost, and well developed processing schemes. It also has desirable optical properties to work as a platform for integrated optical systems at the telecommunication wavelength of 1550nm. Some of these properties are the low optical loss and the high index contrast with its native oxide. This provides high mode confinement for optical waveguides, which enables the integration of high density systems relying on the already developed technologies in the CMOS processes. Fig.1.1 shows a Scanning Electron Microscope (SEM) image of silicon on insulator (SOI) waveguide and its mode profile. Furthermore, silicon wires can serve as a photon source. As shown in Fig.1.1 there is a strong light confinement due to the high refractive-index contrast.

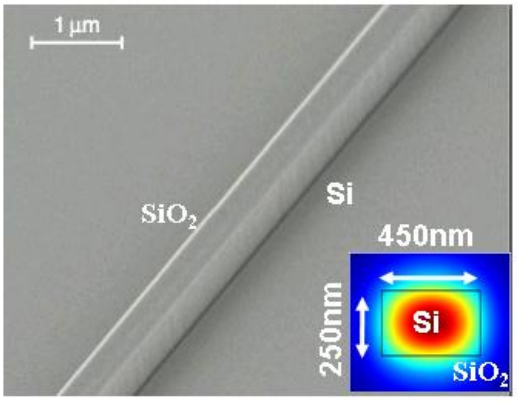

Fig. 1.1 SEM image of SOI waveguide with the mode profile adapted from [1]

Research has been conducted extensively in this area demonstrating many passive devices such as splitters [2], ring resonator based filter [3,4], disk resonator based filters [5], and slow light photonic band-gap waveguides [6,7], to name few. But in order to broaden the functionalities of these devices, active control of the optical properties of silicon is needed. Fig.1.2 shows some examples of SOI based passive devices.

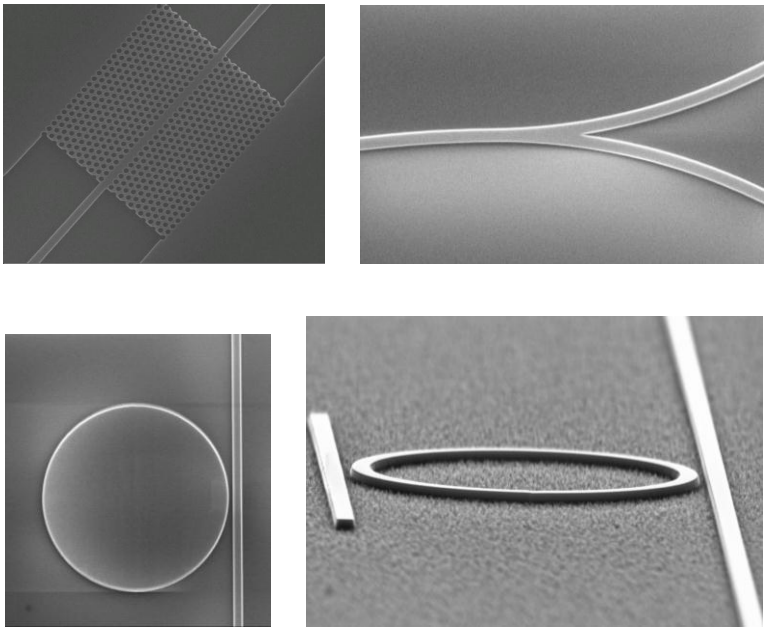

Fig. 1.2 SEM images of some passive SOI device (i.e. ring resonators, disk resonators, photonics crystal waveguides, and splitters).

1.1.1 Tuning the optical properties of silicon

In order to add dynamic control of the passive devices, we need to tune the optical properties of silicon. There are three main effects to manipulate the refractive index of silicon:

- Thermo-optic effect
- Third order non-linearity ($\chi 3$)
- Free carrier dispersion effect.

The first effect results in a desirable high refractive index change per degree which enables broadband tuning of the optical system [8,9]. But the drawback is the slow switching time thermo-optic effect based devices suffer from. This is due to the limitations of how fast heat can be transferred in and out from the active region. Typical switching times are in the order of microseconds [10]. Equation (1.1) relates the change in the refractive index to the change in temperature.

$$dn/dT = 1.84 \times 10^{-4} K^{-1} \quad (1.1)$$

The third order nonlinearity $\chi 3$ on the other has an ultra-fast response of less than 10fs [11,12]. The Centro-symmetric structure of silicon gives rise to two types of them namely: Franz-Keldysh and Kerr effects. The first manifests itself as an electro-optic absorption effect where the band gap of the silicon (E_g=1.12 e.V.) shifts with an applied electric field. The wavelengths affected by this phenomena lie near the absorption wavelength of ~1.1µm with no pronounced changes at the desirable telecom wavelength of 1.3 µm or 1.55µm.

On the other hand, Kerr effect enables different exciting phenomena such as self-phase modulation, cross-phase modulation, continuum generation [13,14], and ultrafast all-optical switching [14,15]. The refractive index change of silicon can be converted to a change of the optical transmission using an interferometer or a resonator structure [16] to build switches. The change in the refractive index is related directly to the intensity of the propagating wave in the system. It is worth mentioning here that ultra-fast second order nonlinearities such as Pockels effect can be introduced in silicon by breaking the symmetry of the crystal [17]. This is done by introducing strain to the active part of the silicon device. Such devices are currently far from practical due to the small nonlinear coefficients observed in addition to the complexity of fabrication. The followings are typical values of the third order nonlinearity parameters: n_2 the intensity dependant refractive index and β the two photon absorption coefficient.

$$n_2 = 0.45 \times 10^{-13} (cm^2/W) \quad 1.2$$

$$\beta = 0.79 (cm^2/GW) \quad 1.3$$

The last effect is the free carrier dispersion effect where the refractive index of silicon and its absorption coefficient change with the free-carriers density [18] . Many active devices have been demonstrated and proposed based on this effect such as electro-optic modulators [19-27], storage units [28,29], wavelength converters [30-33], and optical isolators [34]. The main advantage of this effect is providing a direct link between the electronics and optics using simple structures to inject carriers such as *pin* diodes [21,24,27], Schottky diodes [23], and MOS Capacitors [35] . The following equations describe the change in the refractive index of silicon and the absorption coefficient as a function of the carrier density.

$$\Delta n_{fc} = -[8.8\times10^{-22}\times\Delta N + 8.5\times10^{-18}\times\Delta P^{0.8}] \quad (1.4)$$

$$\Delta \alpha_{fc} = [8.5\times10^{-18}\times\Delta N + 6\times10^{-18}\times\Delta P] \quad (1.5)$$

These carriers can also be generated through absorption of high energy photons (i.e 420nm light) with life times on the order of ~500ps depending on the dimension of the waveguide [36]. The life times can be further reduced for ultra-fast all-optical switching by integrating reverse biased *pin* diodes. This generates high *E* field in the active region which sweeps the carriers away from the active region extremely fast with times less than 50ps [37,38].

1.2 Resonant photonic structures

The effects presented above usually result in a small change in refractive index of silicon on the order of *~5E-04.* This requires very long waveguides to accumulate a π phase shift for full intensity modulation in interference based systems such as Maxh-Zhender (MZ) interferometer. On the other hand the foot-print of the devices can be reduced using compact resonators or cavities that circulate light for long effective lengths in a small area on the expense of the bandwidth the cavities can accept. On chip optical resonators (or filters) can be divided into two main categories: (1) traveling wave resonators such as ring and disk resonators, (2) standing wave resonators such as photonic crystal cavities and Fabry-Perot (FP) cavities. We will focus in this work on traveling wave ring resonators due to their attractive properties as explained below [16].

1.2.1 Traveling-Wave Ring Resonators

Traveling wave ring resonators consist of a waveguide looped to form a closed path that usually supports a single transverse optical mode for a given polarization. They are

desirable in optical systems to eliminate coupling between different modes. Ring resonators are completely configurable in terms of the wavelength selectivity and the number of channels they accept in a given bandwidth range. This can be done through changing the size of the rings and the coupling coefficients to/from the bus waveguide. Another advantage is eliminating back reflections in the optical link because of the traveling wave design when coupling to a resonant mode. This is in contrast to Fabry-Perot (FP) and photonic crystal cavities which support standing wave modes. Lastly, the resonator itself consists from a looped single mode waveguide (with same effective index as the bus waveguide) which simplifies the coupling to resonant modes over short coupling lengths (less than 700nm in 5μm radius ring). Fig.1.3 shows an SEM of a ring resonator with input/output fields.

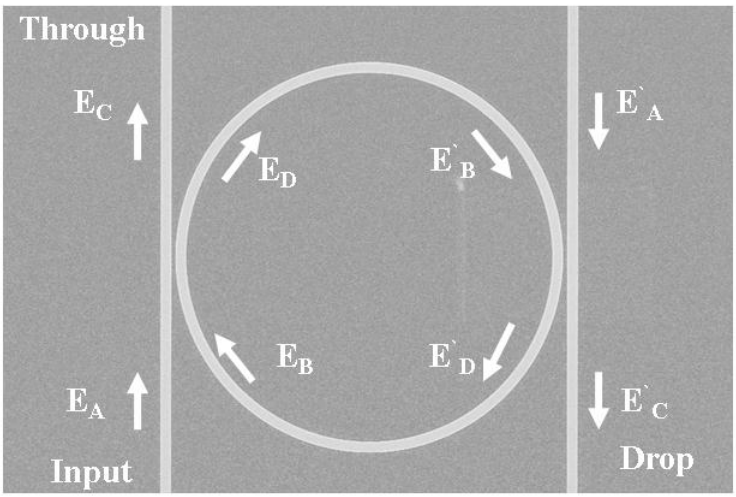

Fig. 1.3 SEM image of a ring resonator with different fields coupling to/from the system

At the resonance condition the circumference of the ring corresponds to integer multiples of the input signal *effective* wavelength as indicated below.

$$2\pi R = m\lambda_0 / n_{eff} \quad 1.6$$

It's important to note here that the effective index of the mode is a function of the input wavelength due to the change in confinement as the wavelength changes. Another important parameter that needs to be presented in dealing with optical time delays and light-matter interaction is the group index. It is related to the speed of the propagating wave inside the waveguide $V_g = v / n_g$ where V_g is the group velocity of the guided wave and n_g is the mode's group index. The proportionality constant n_g can be related to the mode's effective index for different wavelengths as shown in the following equation.

$$n_g(\lambda) = n_{eff}(\lambda) - \lambda_0 \Delta n_{eff} / \Delta\lambda \quad 1.7$$

A typical transmission spectrum (from input port to through port in Fig.1.3) for a ring resonator is shown in Fig.1.4

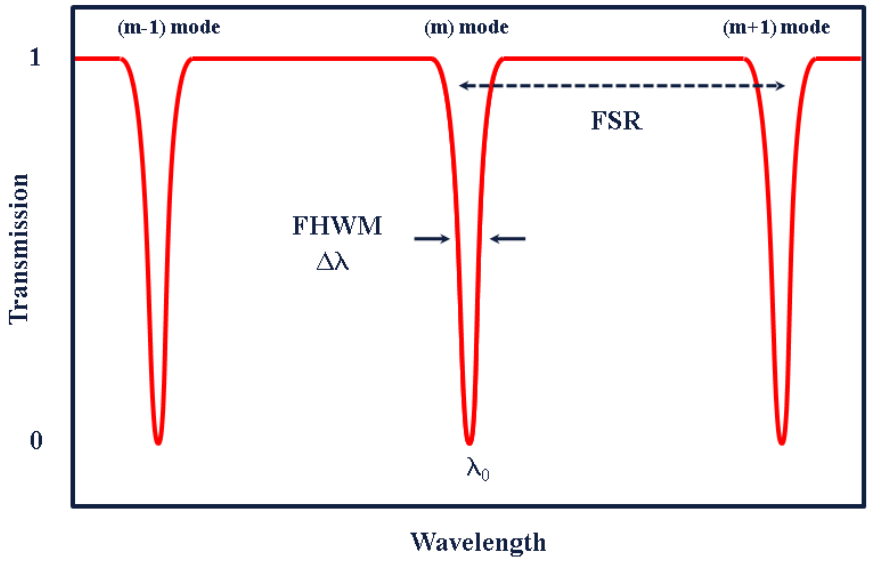

Fig. 1.4 Transmission spectrum of a ring resonator.

We define two quantities to characterize the performance of a ring resonator cavity: the free spectral range (FSR) and the quality factor (Q). The first describes spacing between

the modes and it is inversely proportional to the length of the ring resonator. The smaller the ring the further apart the modes are spaced as shown by the equation below.

$$FSR = \lambda^2 /(n_g 2\pi R) \quad 1.8$$

The second quantity is the quality factor of the resonator which related to the photon life time of the cavity. The smaller the loss in the system, the higher the quality factor. The loss includes waveguide scattering loss, bending radiation loss, and coupling (or leaking) loss to the input/output waveguides from the cavity. The following equations relate the quality factor to the Full Width Half Max (FHWM) of the spectrum and the photon life time τ_p.

$$Q = \lambda_0 / \Delta\lambda \quad 1.9$$

$$\tau_p = Q\lambda_0 /(2\pi c) \quad 1.10$$

Next we will present two methods that are used throughout this work to simulate complex dynamic systems with ring resonators.

1.3 Simulation methods

1.3.1 Time-domain coupled mode equations

Following a similar approach to [16,39] we can describe the coupling between different fields in and out from the resonator of Fig.1.3 at any instant of time t_m through a set of coupling coefficient as shown below.

$$\begin{bmatrix} E_C(t_m) \\ E_D(t_m) \end{bmatrix} = \begin{bmatrix} t_1 & i\kappa_1 \\ i\kappa_1 & t_1 \end{bmatrix} \begin{bmatrix} E_A(t_m) \\ E_B(t_m) \end{bmatrix} \quad 1.11$$

$$\begin{bmatrix} E_C`(t_m) \\ E_D`(t_m) \end{bmatrix} = \begin{bmatrix} t_2 & i\kappa_2 \\ i\kappa_2 & t_2 \end{bmatrix} \begin{bmatrix} E_A`(t_m) \\ E_B`(t_m) \end{bmatrix} \quad 1.12$$

t and κ are the transmission and cross-coupling coefficients of the waveguide-ring coupler. We also set a rule for the field time evolution inside the resonator by defining a prober time step $\Delta t = t_m - t_{m-1}$.

$$E_B(t_m) = E_D`(t_{m-1}) e^{-\frac{\gamma}{2} + \frac{\phi(t,\lambda)}{2}} e^{-j\omega t_m} \quad 1.13$$

$$E_B`(t_m) = E_D(t_{m-1}) e^{-\frac{\gamma}{2} + \frac{\phi(t,\lambda)}{2}} e^{-j\omega t_m} \quad 1.14$$

$\phi(t,\lambda)$ and γ are the accumulated phase and the power loss coefficient per round trip of the resonator. By knowing the effective refractive index of the mode we can easily calculate the round trip phase as shown below.

$$\phi(t_m,\lambda) = n_{eff}(t_m,\lambda)\frac{2\pi}{\lambda} 2\pi R \quad 1.15$$

$$t_m - t_{m-1} = n_g \frac{\pi R}{c} \quad 1.16$$

Using the set of equations presented above we can perform active time domain numerical simulations of arbitrary pulse shapes and time dependant ring-effective index. This will become of great importance when dealing with photon storage and photon isolation when such systems are dynamically tuned from one state to another in time through refractive index tuning.

Lastly the transmission of the ring resonator has a Lorentzian shape [40] as shown in Fig.1.5. The response can be found by solving for the static ratio of the incident electric field E_A and the transmitted electric field E_C.

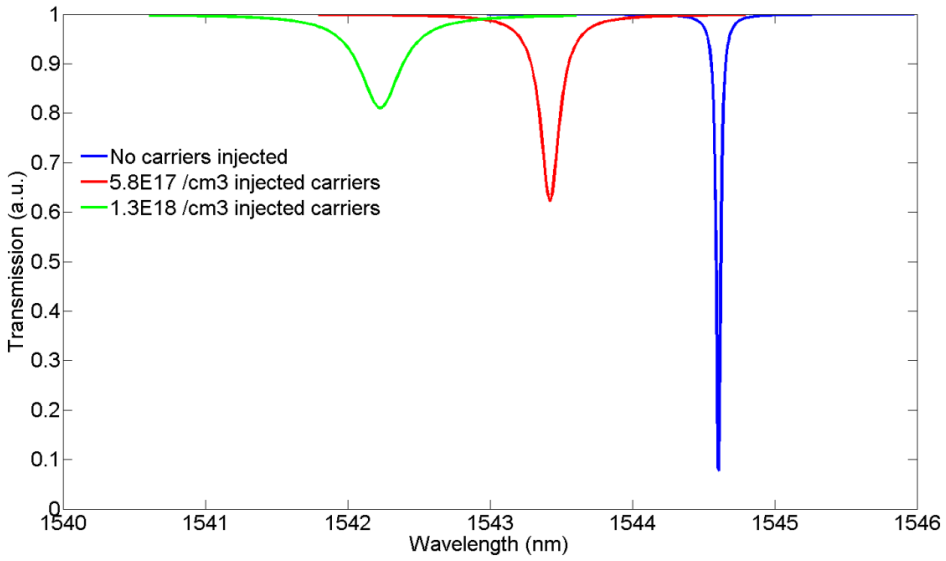

Fig. 1.5 Injected carriers effect on ring resonator transmission.

After injecting carriers in the ring during the switching process (as will be seen in the following sections) we observe a blue shift in the resonance due to the reduction in the effective index of the mode. In addition, the resonance widens due to the increase in the resonator loss from free carriers-light interaction. This is accompanied with a reduction in the extinction ratio and the photon life time of the cavity (shown in Fig.1.5).

$$T = \left|\frac{E_C}{E_A}\right|^2 = 1 - \frac{(1-e^{-2\gamma})(1-t^2)}{(1-t\cdot e^{-\gamma})^2+4\cdot t\cdot e^{-\gamma}sin^2(\phi(\lambda))} \qquad 1.17$$

Critical coupling occurs when the round trip loss equals the power coupling to the cavity $t=e^{-\gamma}$.

1.3.2 Fine Difference time domain equations

Finite-Difference-Time-Domain (FDTD) is a powerful technique for simulating electromagnetic problems using numerical approximations to Maxwell's equations. Applications include nonlinear photonic nano-materials, periodic Bloch problems, scattering, and near-field imaging. The method describes the microscopic spatiotemporal

dynamics of waves inside different media. Unlike the coupled mode equations presented earlier this method is computationally intensive but provides realistic results of the actual behavior of waves in complex photonic structure. Given below is a brief in review of the Yee algorithm used in FDTD simulations.

One dimensional Yee's Algorithm

The algorithm provides the basis of FDTD technique. It relies on the point form of Maxwell's equations to calculate different fields from the derivatives numerically. To demonstrate this we assume for simplicity a one dimensional TEM wave propagating along the *x* axis. We can write the point form of Maxwell's equations as follows.

$$\mu \frac{\partial H_y}{\partial t} = \epsilon \frac{\partial E_z}{\partial x} \tag{1.18}$$

$$\epsilon \frac{\partial E_z}{\partial t} = \mu \frac{\partial H_y}{\partial x} \tag{1.19}$$

We first create nodes in time and space, then using numerical derivatives we can calculate the field evolution at a point *m* in future time (*n+1)* from the spatial information of the surrounding fields *(k+1/2),(k-1/2)* at known times *n,(n+1/2)*. By repeatedly using the same algorithm for different nodes in the problem we can update fields both in time and space. Fig.1.6 shows the order for calculating different fields in one dimensional problem.

$$E_z^{n+1}[k] = E_z^n[k] + \epsilon \frac{\Delta t}{\Delta x}[H_y^{n+\frac{1}{2}}\left[k+\frac{1}{2}\right] - H_y^{n+\frac{1}{2}}\left[k-\frac{1}{2}\right]] \tag{1.20}$$

$$H_y^{n+1}[k] = H_y^n[k] + \frac{1}{\mu}\frac{\Delta t}{\Delta x}[E_z^{n+\frac{1}{2}}\left[k+\frac{1}{2}\right] - E_z^{n+\frac{1}{2}}\left[k-\frac{1}{2}\right]] \tag{1.21}$$

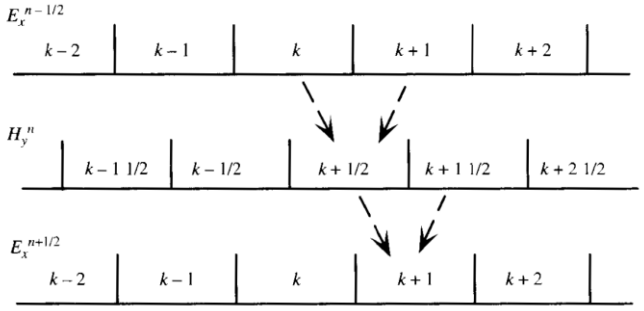

Fig. 1.6. Field evolution order in 1D-FDTD problem, adapted from [41].

The technique can be generalized to 2D and 3D problems by considering their respective derivatives in space. In addition, active control of the system can be introduced by using a time dependent $\epsilon(t)$ and $\mu(t)$ which will be of great importance in considering photon energy lifting structures and photon trapping. Fig.1.7 shows a 2D FDTD simulation of a CW light coupled to SOI ring resonator at resonance.

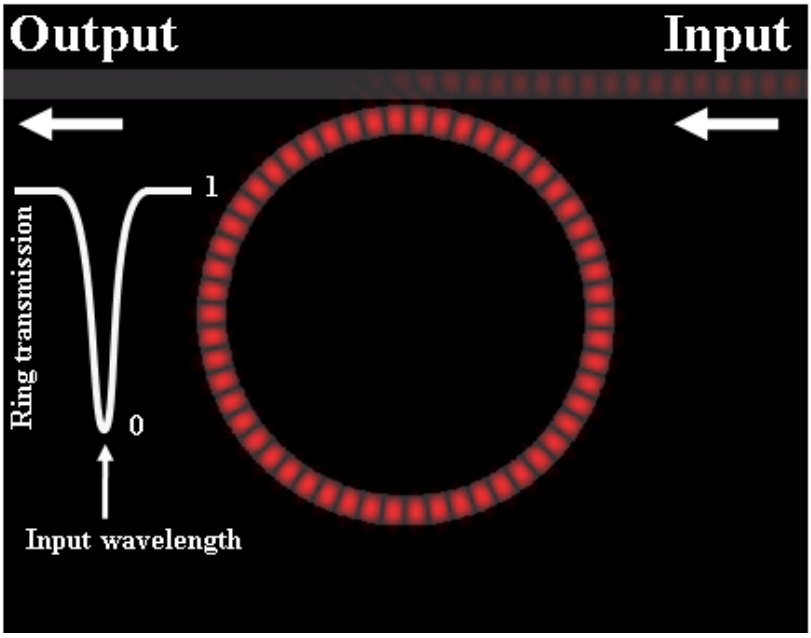

Fig 1.7 2D FDTD simulation of SOI ring resonator on resonance.

CHAPTER TWO

SINGLE PHOTON-CAVITY QUANTUM ELECTRODYNAMICS (QED)

2.1 Introduction

Photons are the main information carriers in quantum based communication systems. In free space optics, a quantum bit (or qubit) of information can be manipulated and encoded in any of several degrees of freedom, notably polarization, in which case this process is usually straightforward using birefringent waveplates [42]. In order to have more functionality in future quantum computing systems, devices need to be scaled down to the micro- and nano- integration level. One potential platform is Silicon, which has desirable optical properties for integrated optical systems at the telecommunication wavelength of 1550 nm. In addition, it is considered as a candidate for generating single photon sources relying on the high third order nonlinearity $\chi(3)$ [43]. Using such sub-Poissonian sources enables revolutionary new technologies [44]- individual photons have been used to dramatically enhance communication security [45], have increased measurement precision beyond the standard quantum limit [46,47], have been used to beat the diffraction limit[48,49], and they hold great promise for quantum computation [50,51]. Surprisingly a quantum mechanical theory describing photon/resonator interactions solved under the steady-state harmonic excitation condition has only recently been formulated [52,53]. Further, the full dynamical behavior of the system needs to be considered in order to describe more complex single photon manipulation processes. In this work we develop a dynamical model for single photon interactions with cavities. As a first application to this approach, we describe the process of single photon energy

lifting in optical cavities, the semi-classical analogue of which has already demonstrated [32,33,54]. We further show that fully quantized model of the process follows the adiabatic condition for dynamical systems and that the process has 100% wavelength conversion efficiency for states trapped in the cavity during the tuning process. As a second application for our solutions we present and analyze single photon trapping analogue to coherent population trapping (CPT) using tunable micro-cavities which presents the building blocks of optical memories on chip [28,55-57]. The adopted design employs a lossless storage unit approach with a tuning mechanism compatible with common silicon photonic circuits.

2.2 Single photon-cavity interaction

2.2.1 Steady state theoretical model

Consider a one-dimensional, single mode waveguide coupled to cavity via an evanescent coupling, as shown in Fig. 2.1. In what follows, we assume that the single photon state is injected into the waveguide from the left and propagates through the waveguide (cavity) in the positive x (counter-clockwise) direction. Specifically, we assume that there is no impurity interaction within the system and therefore no contribution due to reflection, as easily verified by "turning off" the impurities in Ref. [53] by setting $g_a = g_b = h = 0$ in the results presented in that paper. Setting $\hbar = 1$, as we will do throughout unless otherwise stated, the effective Hamiltonian for the system we study takes the form [53]

$$\hat{H}_{\text{eff}} = \int dx c^{+}(x)\left(\omega_0 - iv_g \frac{\partial}{\partial x}\right)c(x) + \left(\omega_c - i\frac{1}{\tau_c}\right)\hat{a}^{+}\hat{a} + \int dx \delta(x)\left[Vc^{+}(x)\hat{a} + V^{*}\hat{a}^{+}c(x)\right] \qquad 2.1$$

where $\left(\hat{c}(x),\hat{c}^{+}(x)\right)$ are the position dependent inverse Fourier representations of the usual Boson ladder operators describing the rightward traveling waveguide mode, and $\left(\hat{a},\hat{a}^{+}\right)$ are the Boson ladder operators describing the counter-clockwise cavity mode. The canonical commutation relations for the system are $\left[\hat{a},\hat{a}^{+}\right]=1$, $\left[\hat{c}(x),\hat{c}^{+}(x')\right]=\delta(x-x')$; $\left[a,\hat{c}^{+}(\hat{x})\right]$ and all other combinations vanish. In using this form of the effective Hamiltonian we are assuming that the waveguide is driven at a frequency within a narrow range far from the cutoff frequency of its dispersion relation, and that v_g is the group velocity for the traveling waveguide mode [52]. The evanescent coupling is represented by the local interaction term having coupling strength $|V|$ where the coupler is situated at x = 0. The cavity lifetime of the ring-resonator is τ_c where cavity losses have been included using the simple model of a complex frequency (energy) shift from the resonance frequency, ω_c, of the ring resonator [58]. This simple model for dissipation results in the explicitly non-Hermitian form of the effective Hamiltonian.

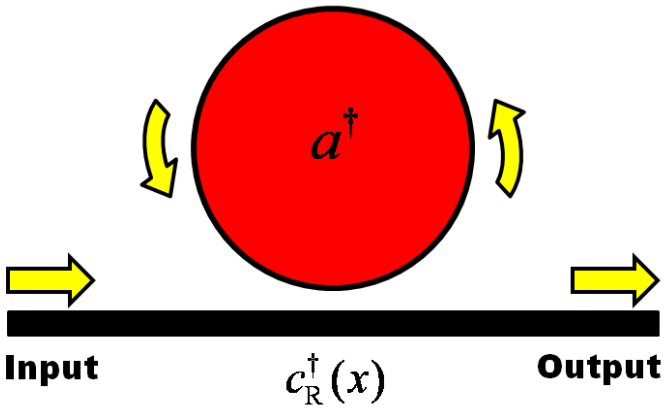

Fig.2.1 Schematic of waveguide-cavity coupled system.

A general one photon state of the system can be written in the form

$$\left|\Phi_1(t)\right\rangle = \left(\int dx \tilde{\phi}(x,t)\hat{c}^{+}(x) + \tilde{e}_{\text{cav}}(t)\hat{a}^{+}\right)\left|0,0\right\rangle \tag{2.2}$$

where $\tilde{\phi}(x,t)$ and $\tilde{e}_{\text{cav}}(t)$ are the time dependent excitation amplitudes for field in the waveguide and the cavity, respectively, and where $\left|0,0\right\rangle \equiv \left|0\right\rangle_{\text{w.g.}} \otimes \left|0\right\rangle_{\text{cav}}$ represents the vacuum state of the field.

The quantum dynamics of the system is described by the Schrödinger Equation

$$i\frac{\partial}{\partial t}\left|\Phi_1(t)\right\rangle = \hat{H}_{\text{eff}}\left|\Phi_1(t)\right\rangle \tag{2.3}$$

Substitution of the second quantized forms in Eqns. (2.1) and (2.2) into Eqn. (2.3) and then projecting alternatively on to the one photon waveguide ("w.g.") and cavity ("cav") subspaces using the single photon basis states $\left|1,0\right\rangle = \hat{c}^{+}(x)\left|0,0\right\rangle$ and $\left|0,1\right\rangle = \hat{a}^{+}\left|0,0\right\rangle$, respectively, yields the coupled set of time evolution equations for the first quantized excitation amplitudes,

$$\left(\omega_0 - iv_g\frac{\partial}{\partial x} - i\frac{\partial}{\partial t}\right)\tilde{\phi}(x,t) + \delta(x)V\tilde{e}(t) = 0 \tag{2.4}$$

$$\left(\omega_{\text{c}} - i\frac{1}{\tau_{\text{c}}} - i\frac{\partial}{\partial t}\right)\tilde{e}_{\text{cav}}(t) + V^{*}\tilde{\phi}(0,t) = 0 \tag{2.5}$$

These are precisely the dynamical equations derived by Shen and Fan in Ref. [53] suitably modified for the system we study here, and, in fact, our choice of notation is intentionally similar to that adopted by Shen and Fan so that the reader can more easily translate between our results and the existing literature in this area.

Stationary state solutions

For ease of reference we now include a brief review of the stationary state analysis of the system we consider. One seeks stationary states of a quantum dynamical system by

seeking solutions to Eqn. (3) having the form $|\Phi_1(t)\rangle = |\phi\rangle e^{-i\omega t}$ where ω is the eigenfrequency for the system, related the energy eigenvalue, ε, in the usual way, $\varepsilon = \hbar\omega$. Doing this results in the coupled set of equations

$$\left(\omega_0 - iv_g \frac{\partial}{\partial x} - \omega\right)\phi(x) + \delta(x)Ve_{\text{cav}} = 0 \qquad 2.6$$

$$\left(\omega_c - i\frac{1}{\tau_c} - \omega\right)e_{\text{cav}} + V^*\phi(0) = 0 \qquad 2.7$$

where the time independent amplitudes are defined via $\tilde{\phi}(x,t) = \phi(x)e^{-i\omega t}$ and $\tilde{e}_{\text{cav}}(t) = e_{\text{cav}}e^{-i\omega t}$. Typically, the stationary state solution for the waveguide excitation amplitude is written in the form $\phi(x) = e^{iQx}\left[\theta(-x) + t\,\theta(x)\right]$, where Q is the wave vector for the traveling mode, t is the transmission coefficient for the traveling mode after interacting with the ring-resonator, and θ(x) is the Heaviside step function. This form follows from the single particle Bethe Ansatz for the interacting eigenstate once the Lipmann-Schwinger formalism is used to identify the input and output amplitudes for the waveguide state vector [59]. In this case the Bethe Ansatz is especially simple as the waveguide state is taken to be a momentum eigenstate $(p = \hbar Q)$, an approximation imposed in order to restrict the waveguide to a single, dominant mode. In the Appendix we present the details of an alternate and, we believe, equally direct and slightly more general method for finding the stationary state solutions for the system and the associated momentum eigenvalue (scaled by $\hbar$) and transmission amplitude. We quote the results here for use in selecting operating parameters for our dynamical simulations below:

$$Q = \frac{\omega - \omega_0}{v_g} \qquad 2.8$$

$$t = \frac{\omega - \omega_c + i\frac{1}{\tau_c} - i\Gamma}{\omega - \omega_c + i\frac{1}{\tau_c} + i\Gamma} \tag{2.9}$$

where $\Gamma \equiv \frac{|V|^2}{2v_g}$.

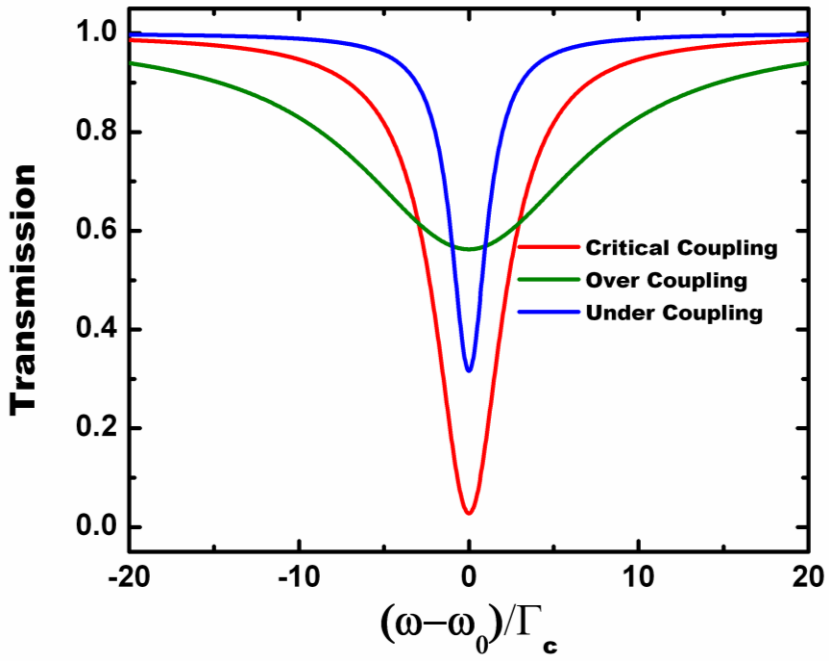

Fig. 2.2 Transmission with different coupling conditions. The transmission at resonance is 0%, 35% and 55% for critically-coupled, under-coupled, and over-coupled system respectively.

We now choose model parameters that expose the salient features of the time evolution of the single photon state. The transmission of the waveguide cavity systems depends on the coupling condition with respect to the internal cavity loss. Fig.2.2 shows the single photon state transmission for critically-coupled ($\Gamma = \frac{1}{\tau_c}$ 0% transmission at resonance), under-coupled ($\Gamma < \frac{1}{\tau_c}$ 35% transmission at resonance) and over-coupled ($\Gamma > \frac{1}{\tau_c}$ 55% transmission at resonance) cavity waveguide system. For demonstration purposes the

cavity is operated slightly in the under-coupled regime to provide high enough photon life times for different dynamic processes. In practical devices, complete capture of the wave packets can be achieved [60].

Calculus of residues

Here we solve for the stationary states of the system without reference to any particular ansatz for the form of the result. We show that the well established results for the stationary states of the system emerge naturally from the mathematical structure of the approach. We anticipate that this method, properly extended, might simplify the significantly more complicated mathematical development of multi-photon transport processes involving quantum electrodynamic couplings between systems having continuous spectra and those having discrete spectra.

The general solution to the differential equation for $\phi(x)$ can be written as $\phi(x)=\phi_{\mathrm{h}}(x)+\phi_{\mathrm{p}}(x)$ where $\phi_{\mathrm{h}}(x)=\phi_{\mathrm{h}}(0)e^{iQx}$ is the homogeneous (viz. V = 0) solution with $Q\equiv\frac{\omega-\omega_0}{v_g}$. We now obtain the particular solution, $\phi_{\mathrm{p}}(x)$.

Introducing the Fourier Transform, $F(\alpha)=\int_{-\infty}^{+\infty}dx\phi(x)e^{i\alpha x}$, and its inverse, $\phi(x)=\frac{1}{2\pi}\int_{-\infty}^{+\infty}d\alpha F(\alpha)e^{-i\alpha x}$, we transform Eqn. (2.6) into Fourier (α) space to obtain

$$(\omega_0-v_g\alpha-\omega)F(\alpha)+Ve_{\mathrm{cav}}=0$$

where, owing to the trivial nature of the Fourier Transform of Eqn. (2.7), we obtain $e_{\mathrm{cav}}=\frac{V^*\phi(0)}{\omega-\omega_{\mathrm{c}}+i\frac{1}{\tau_{\mathrm{c}}}}$. Combining these results we obtain for the Fourier Transform of the

waveguide amplitude function, $F(\alpha)=\left(\frac{\frac{|V|^2}{v_g}\phi(0)}{\omega-\omega_c+i\frac{1}{\tau_c}}\right)\frac{1}{\alpha+\left[\frac{\omega-\omega_0}{v_g}\right]}$. Inverting the Fourier Transform yields a particular solution, $\phi_p(x)=\frac{1}{2\pi}\left(\frac{\frac{|V|^2}{v_g}\phi(0)}{\omega-\omega_c+i\frac{1}{\tau_c}}\right)\int_{-\infty}^{+\infty}\frac{d\alpha e^{-i\alpha x}}{\alpha+\left(\frac{\omega-\omega_0}{v_g}\right)}$, which we evaluate using the calculus of residues after analytically extending $F(\alpha)$ into the a complex z-plane, defined by $z\equiv\alpha+i\beta$ where α and β are each real numbers. Let us work out the details by considering for a moment only the integral and defining, suggestively, $Q\equiv\left(\frac{\omega-\omega_0}{v_g}\right)$. That is, we must ascertain the value of the improper integral, $\int_{-\infty}^{+\infty}\frac{d\alpha e^{-i\alpha x}}{\alpha+Q}$, where q is a real number. Clearly the integrand has a simple pole at $\alpha=-Q$.

In order to apply the residue theorem from complex analysis, we define the contour integral around a closed contour in the z-plane, $\oint\frac{dze^{-izx}}{z+Q}=P\int_{-\infty}^{+\infty}\frac{d\alpha e^{-i\alpha x}}{\alpha+Q}+\lim_{\eta\to 0}\int_{sc}\frac{dze^{-izx}}{z+Q}+\int_C\frac{dze^{-izx}}{z+Q}$, where P indicates the Cauchy Principal Value of the improper integral and C is an infinite semicircle chosen to ensure convergence and therefore vanishing of this contribution to the contour integral. The remaining term represents an infinitesimal semicircular deformation in the contour needed to accommodate a pole such as this one that lies along the path of the integration [61]. The various pieces of the contours for the cases x > 0 and x < 0 are displayed in Figure (10). Referring to Fig 2.3 and using the result that the residue theorem as applied

here gives $\oint \frac{dze^{-izx}}{z+Q} = \pm 2\pi i e^{iQx}$ provided that the pole at α = -Q is encircled by the contour of integration and where the + (-) sign corresponds to a counterclockwise (clockwise) sense of integration. Applying the mean value theorem to the infinitesimal semicircular deformation yields $\lim_{\eta \to 0} \int_{sc} \frac{dze^{-izx}}{z+Q} = \pm \pi i e^{iQx}$ where the + (-) sign corresponds to a counterclockwise (clockwise) sense of integration around the infinitesimal deformation in the contour.

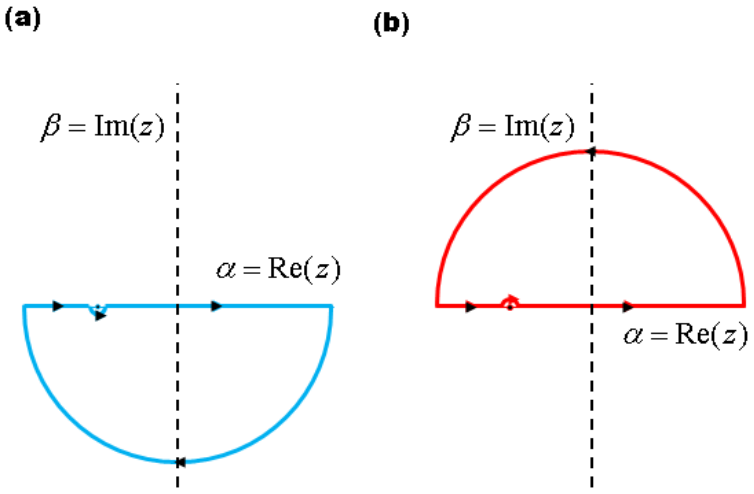

Fig. 2.3 Contours in the complex z plane used for inversion of the Fourier transform of the waveguide amplitude for the cases (a) x > 0 and (b) x < 0.

We now handle the integration in two regions. For x > 0, we choose the clockwise path having the infinite semicircular branch in the β < 0 half plane (see Fig. (10a)). Deforming the contour in a counterclockwise sense relative to the pole at α = -Q excludes the pole from the region encircled by the contour. So, for x > 0, we obtain $P\int_{-\infty}^{+\infty} \frac{d\alpha e^{-i\alpha x}}{\alpha + Q} = -i\pi e^{iQx}$ (note that including the pole with a clockwise deformation yields the same result). For x

< 0, we choose the counterclockwise path having the infinite semicircular branch in the β > 0 half plane (see Fig. (10b)). Deforming the contour in a clockwise sense relative to the pole at α = -Q excludes the pole from the region encircled by the contour. So, for x < 0, we obtain $P\int_{-\infty}^{+\infty}\frac{d\alpha e^{-i\alpha x}}{\alpha+Q}=i\pi e^{iQx}$ (again independent of the choice for the deformation).

Collecting the results from the calculus of residues and combining them in the inverse Fourier form for the particular solution gives $\phi_{\mathrm{p}}(x)=\frac{i}{2}e^{iQx}\left(\frac{\frac{|V|^2}{v_g}\phi(0)}{\omega-\omega_{\mathrm{c}}+i\frac{1}{\tau_{\mathrm{c}}}}\right)\left[\theta(-x)-\theta(x)\right]$. Notice that the residue theorem immediately enforces the appropriate dispersion relation for our rightward traveling wave. Now, it is clear from the forms of $\phi_{\mathrm{h}}(x)$ and $\phi_{\mathrm{p}}(x)$ that $\phi_{\mathrm{p}}(0)=0$ and $\phi_{\mathrm{h}}(0)=\phi(0)$. Defining $\phi(0)\equiv\phi_0$, $\Gamma\equiv\frac{|V|^2}{2v_g}$, and $D\equiv\omega-\omega_{\mathrm{c}}+i\frac{1}{\tau_{\mathrm{c}}}$ to simplify the notation, we can now write the general solution for the stationary state as $\phi(x)=\phi_0 e^{iQx}\left(1+\frac{i\Gamma}{D}\left[\theta(-x)-\theta(x)\right]\right)=\phi_0 e^{iQx}\left[\left(1+\frac{i\Gamma}{D}\right)\theta(-x)+\left(1-\frac{i\Gamma}{D}\right)\theta(x)\right]$. This state has the form

$\phi(x)=e^{iQx}\left[A\theta(-x)+B\theta(x)\right]=\begin{cases}Ae^{iQx} & x<0\\ Be^{iQx} & x>0\end{cases}$, exactly the form of a one dimensional scattering problem in which (i) the target is localized at x = 0, (ii) there is no reflection (r = 0), and (iii) the target has internal structure from which irreversible losses to the environment can occur. In one dimensional scattering theory the transmission coefficient is defined as $t\equiv\frac{B}{A}$ as it relates to this form. In the present case we have $t\equiv\frac{D-i\Gamma}{D+i\Gamma}$

which, upon substitution for D and Γ, is exactly the result given in Eqn. (9) in Section II.

We emphasize that the method we have presented relies on no additional assumption beyond the existence of the Fourier transform pairs we have used. Rather, the form of the interacting eigenstate emerges naturally as the solution to the system of equations determining the stationary states. In fact, the state that we derive as the general solution turns out to be exactly the single particle Bethe ansatz state that one would expect in this simple case. In a future work we will extend this method to cases involving more than one photon, and in so doing provide another mathematical mechanism for backing out the S-matrix for the interaction. In the single photon case and; therefore, for our purposes here, this further sophistication is not necessary.

2.2.2 Experimental results

To verify this result we tested microring resonators with single photons. A scanning electron microscope image of the cavity system we used is shown in Fig. 2.4. It consists of two ring resonators integrated into a Mach-Zehnder interferometer configuration. This configuration was selected as it allows us to observe more complex single photon interference than with just a single cavity. The single photon enters the system from the input port to a 50/50 Y-splitter, which puts the photon into a superposition of being in either the left or right path. In both paths there are ring resonators which will transfer photons across to the output-port side when the photons are in resonance with the cavity. Once across, the paths are recombined where the photon can either constructively or destructively interfere with itself based on the relative phase difference between the left and right paths. We should note that if the photon is not in resonance with one or both of the resonators then system interference would collapse because the path the photon takes

could be determined by its wavelength. In addition, if the duration of the photon is shorter than the photon lifetime of the cavity, then photon interference will not be observed.

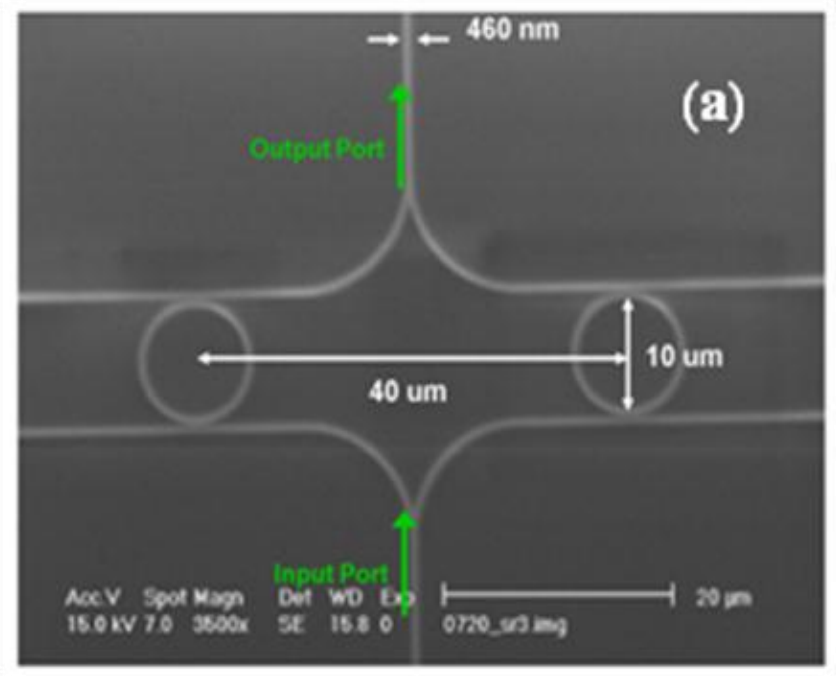

Fig. 2.4 SEM image of a compact MZ interferometer with integrated ring resonators. This system was used to verify single photon interactions with resonant cavities.

The experimental setup used to demonstrate single photon interference is shown in Fig 2.5. It consists of a mode-locked Ti:Sapphire laser which is used to pump an Optical Parametric Oscillator in order to produce ~200femtosecond pulses at a wavelength of ~1550nm. These pulses are then filtered to a 0.25nm bandwidth, which effectively produces a pulse with a ~5picosecond duration. This pulse duration is comparable to the photon lifetime of the ring resonators, therefore the amount of coupling to the cavity is maximized. This pulse is then attenuated to a single photon level as verified by measuring the average power and repetition rate of the pulses. These single photon pulses

are then sent through a variable optical delay line which allows us to synchronize the photons with the detection circuitry. Then the photons are sent into the chip where they interact with the device shown in Fig 2.4. After leaving the chip the photons are detected by a single photon detector.

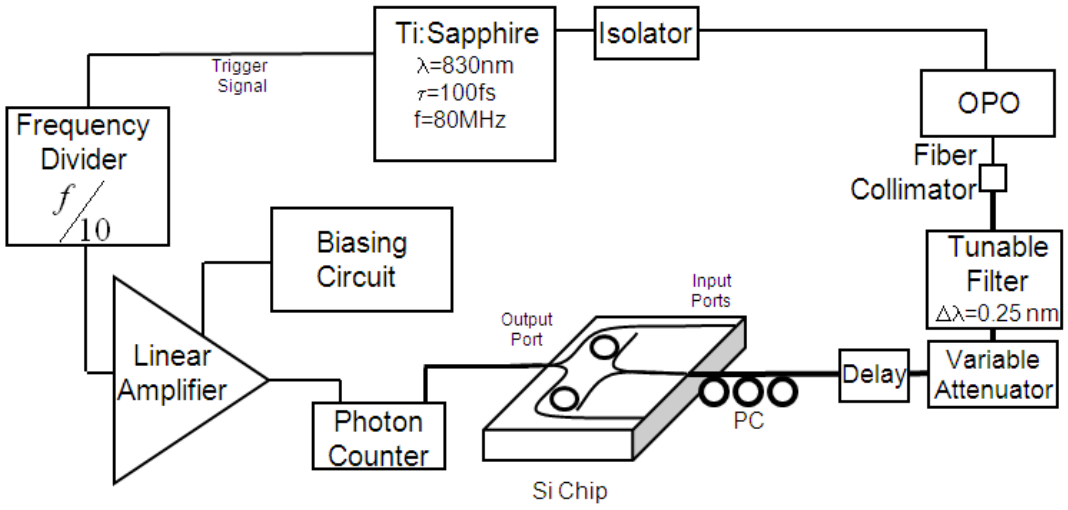

Fig. 2.5 Experimental setup used to measure single photon interference.

We see in Fig.2.6 that when the photons wavelength is around 1527.9nm there is a dramatic change in the transmission. In Fig. 2.6 (first) the transmission of one of the ring resonators (i.e. the left or right branch) exhibits a significant dip due to the coupling of the photon into the ring resonator (and then to the output port). In addition, we can see coupling to the output port and constructive interference in Fig 2.6 (second). We also tested the system with much shorter (larger bandwidth) single photon pulse. In this case the photons duration is too short to exhibit interference with itself in the ring resonator; in essence it behaves as a particle.

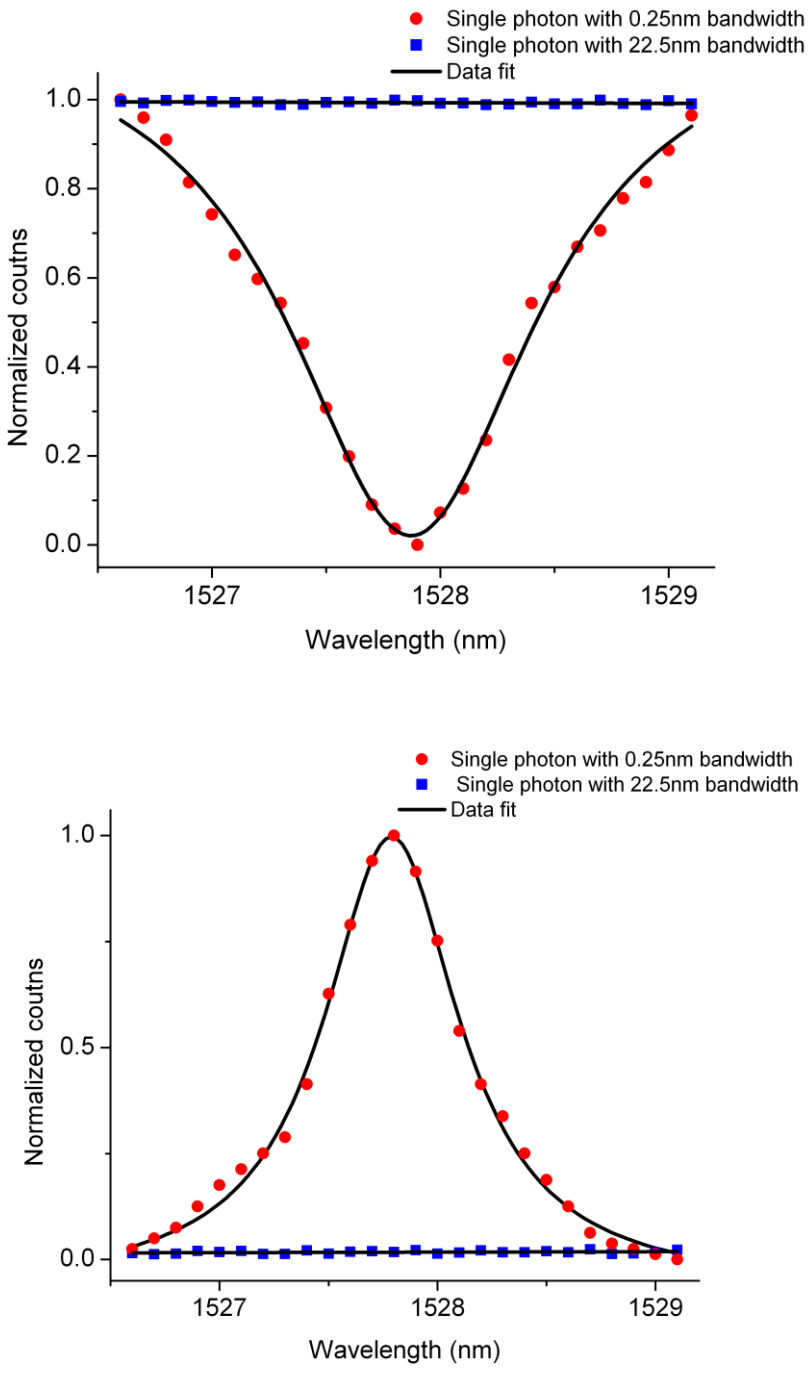

Fig. 2.6 Measured transmission of a long (small bandwidth) photon and a short (large bandwidth) photon through the ring resonator (left) and through the output port of the device (right).

This is seen in Fig 2.6 where the curves for the large bandwidth photon (22.5nm) do not exhibit wavelength dependence and simply transmits unaltered by the ring resonator.

Therefore, as expected, in order for single photons to exhibit interference the bandwidth of the photon and the resonator must be comparable to each other. The ability to filter and rout photons enables robust control of the flow of photons a chip. This will also enable the realization of complex quantum information circuits on chip. As will be discussed in the next chapter, we have demonstrated initial control of the cavities using carrier injection. New exciting phenomena are expected to immerge when launching photons into an active medium.

2.2.3 Dynamic theoretical model

In order to examine the transient dynamic response of the system to an arbitrary single photon input, we solve the equations of motion (Eqn. (2.4 and 2.5)) numerically. To do so we use a finite difference method, it is commonly used to analyze electromagnetic scattering and propagation [62]. We begin by specifying an initial input single-photon state. The time evolution of the state is described by using the knowledge of the amplitude functions at each grid point in space at the previous time step and propagating forward to the next time step using the finite difference approximation shown in Eqns. (2.10 and 2.11).

$$\tilde{\phi}(k,n+1) = \Delta t \cdot \left(\frac{\tilde{\phi}(k,n)}{\Delta t} - i\omega_0 \tilde{\phi}(k,n) - \left(\frac{\tilde{\phi}(k,n) - \tilde{\phi}(k+1,n)}{\Delta x / v_g}\right) - i\delta(N) V \tilde{e}(n)\right) \quad 2.10$$

$$\tilde{e}(n+1) = \Delta t \cdot \left(\frac{\tilde{e}(n)}{\Delta t} - i\omega_c \tilde{e}(n) - iV\tilde{\phi}(N,n) - \frac{\tilde{e}(n)}{\tau_c}\right) \quad 2.11$$

Where N is the spatial grid point representing the cavity/waveguide coupling region; the interaction is clearly a local one.

To demonstrate this process and to elucidate the quantum mechanical features of the

system we consider a single photon state with a Gaussian amplitude (hereafter referred to as the "Gaussian wave packet") incident on the cavity waveguide system. The propagation of the single photon wave packet through the system is typified by the profiles plotted in Fig.2.7.

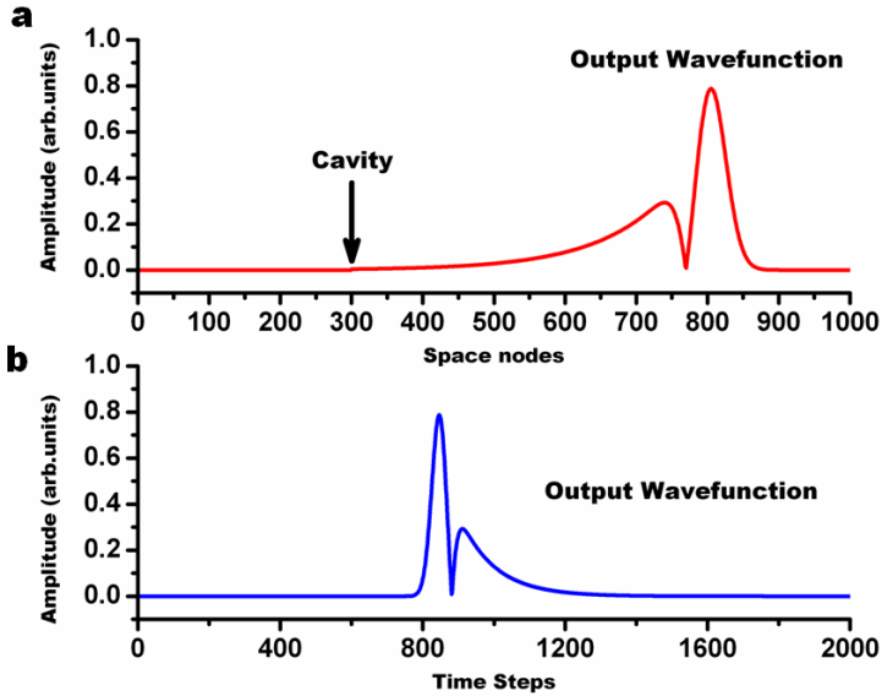

Fig.2.7 Transmission of a Gaussian packet through the cavity waveguide system.

In Figure 2.7a we display the absolute magnitude of the probability amplitude for the wave packet as a function of position along the waveguide for a fixed time. We have chosen that time to be long after the photon could have (i) first interacted with the microcavity resonator at the coupling region and/or (ii) could have completed a round trip in the resonator if it were injected upon interaction at the coupler. Several general features of the solution are apparent. First, there are clearly general positions within the waveguide at this time at which the photon is likely to be detected. Unlike the case involving classical fields, this is a signature of quantum interference between the branch

of the photon state vector representing direct transmission of the photon at the coupler and the branch representing a single round trip in the cavity before transmission. Put another way, if we were to place perfectly efficient single photon detectors at the locations of the two peaks in the figure, then (at most, see below) only one of them would fire in any individual run of the experiment. By operating in the under-coupled regime, we can neglect the contributions of higher order terms arising form more than one round trip through the microcavity prior to transmission through the waveguide. Second, it is the larger peak in Figure 2.7a that corresponds to direct transmission. This peak is centered at $x_d = v_g t$ where t is the time at which the "snapshot" in Figure 2.8a is taken and we are taking t = 0 to be the moment at which the photon is incident upon the coupling region. The round trip peak is smaller, broader and lags the direct peak by a distance of $\Delta x = v_g(2\pi nR/c)$ where R is the radius of the microcavity and n is the effective intra-cavity index of refraction. Third, the round trip peak is attenuated relative to the direct peak; this is a result of (i) our choice of coupling strength (which is unitary and therefore probability conservative) and (ii) cavity losses (which is irreversible and therefore not probability conservative). The unitary source of the difference in peak height is a simple consequence of our choice to operate in the under-coupled regime. The irreversible part is due to cavity losses. This means that in any individual realization of the experiment there is a finite probability for the photon to be "lost" to the environment. Because we are considering only single roundtrip events in our model with relatively weak losses, we expect that the resultant lack of normalization in the output will be small. Because it does not impact the major results presented here, we make no effort to deal with this loss quantitatively here, but it is readily apparent by inspection of Figure 2.7a

that it is a small effect in the regime we are considering. To examine a fourth feature of the solution, consider Figure 2.7b, which shows the time evolution of the modulus of the amplitude function at a fixed position in the waveguide beyond the coupling region. Clearly, the direct peak arrives at an earlier time that the roundtrip peak, as discussed above. One can think of this curve in terms of a photon counting Gedankenexperiment. Suppose we measure the probability of detecting m photons at a time delay Td after the interaction, P(m,Td) for an ensemble of similarly prepared runs of the single photon transport experiment. Figure 2.7b suggests we should see non-zero results only around P(1,Td ≈ x/vg) and $P(1,T_d) \gtrsim x/v_g + 2\pi nR/c$. Again, these results are ultimately traceable to quantum interference between the branches of the single photon state vector. Further, the decay tail of the second peak depends on the cavity decay rate and the coupling factors between the cavity and the waveguide.

We envision that through careful quantitative study of the features described in this section, we can, with the advent of efficient, single photon detectors, develop an experimental protocol for characterizing the optical properties of the photonic structures we are considering here. This is an exciting possibility that we will explore elsewhere.

2.3 Photon-pair generation in silicon wire

2.3.1 Theoretical model

An essential part in these systems is the single photon source. A common off-chip method to generate quantum pairs of photons is Spontaneous Parametric Down Conversion (SPDC) in a nonlinear crystal [63]. In order to make these systems more useful in the future optical communication systems we need to move to on-chip

generation, detection, and processing of qubits. Single photon sources has been demonstrated using quantum-dot photonic wires [64] and $\chi 3$ based nonlinear processes in silicon [43].

A Si wire WG can achieve strong light confinement due to its high refractive-index contrast. The core size of a Si wire WGs for single mode propagation is less than a micrometer. Because of such a small core, the power density of a Si wire is higher by a factor of about 1000 than that of conventional single-mode fiber. Consequently, it is expected that nonlinear optical effects will occur when using a low input power equivalent to that in optical communications. Light propagation with such a high power density can produce a wide variety of nonlinear phenomena, including stimulated Raman scattering (SRS), stimulated Brillouin scattering (SBS), self-phase modulation (SPM), crossphase modulation (XPM), two-photon absorption (TPA), and four-wave mixing (FWM) [65]. In FWM there has been a focus on the traditional regime in which a high-power pump is used to amplify a signal and simultaneously generate an idler beam. Such a process is usually done in the anomalous dispersion regime to compensate the phase shift generated by the pump for phase matching. Given below are the general equations governing a degenerate FWM in silicon-waveguide.

$$2\omega_{pump} = \omega_{signal} + \omega_{idler} \tag{2.12}$$

$$\Delta k = 2\gamma P_{pump} - \Delta k_L \tag{2.13}$$

$$\Delta k_L = 2k_{pump} - k_{signal} - k_{idler} \tag{2.14}$$

Where $\gamma = \frac{\omega n_2}{x A_{eff}}$

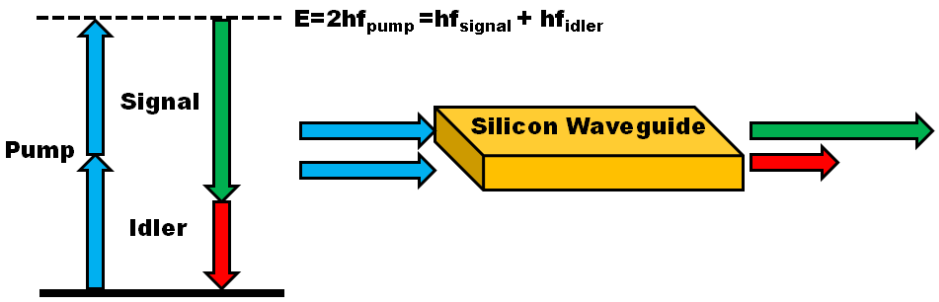

Fig.2.8 FWM process in silicon waveguides.

However, as FWM is a four-photon elastic scattering process, it conserves physical quantities such as energy and momentum among the four interacting photons. As a result, if no signal is initially present so that FWM is initiated from vacuum noise and the pump power is relatively low so that stimulated FWM does not occur, it is possible to create only one pair of signal and idler photons at a time (within the coherence time of the pump) that are correlated quantum mechanically in multiple dimensions. Such correlated photon pairs are useful for applications in quantum information processing [11] [66]. The same process can be accomplished with the aid of optical cavities to increase the creation efficiency at resonance [67] [68]. By improving the quality of the resonator the conversion efficiency increase due to the high field enhancement (FE) factor at resonance [68] $P_{idler} = \eta_{classical} P_{signal}$.

$$\eta_{classical} = \frac{P_{idler}}{P_{signal}} = \left|L \cdot \gamma\right|^2 \cdot (FE)^8 \cdot P^2{}_{pump} \qquad 2.15$$

To describe this process for generating single photon pairs, Consider a one-dimensional, single mode waveguide coupled to cavity via an evanescent coupling, as shown in Fig.2.9. In what follows, we assume that the pump photon state is injected into the waveguide from the left and propagates through the waveguide (cavity) in the positive x (counter-clockwise) direction. Specifically, we assume that the FWM is described by the

nonlinear third order Hamiltonian. Setting $\hbar = 1$, as we will do throughout unless otherwise stated, the effective Hamiltonian for the system we study takes the form [69]

$$\hat{H}_{\text{eff}} = \sum_{\mu} \hat{H}_{\text{channel}} + \sum_{\mu} \hat{H}_{\text{coupler}} + \sum_{\mu} \hat{H}_{\text{ring-linear}} + \hat{H}_{\text{ring nonlinear}} \quad 2.16$$

The sum above is performed for different modes propagating in the waveguide and the channel. Considering all the different interactions and energy transfers in the system we can easily write down expressions for the different Hamolitnians based of the creation and annihilation operators for different modes.

$$\hat{H}_{\text{channel}} = \int dx c_{\mu}^{+}(x) \left(\omega_{\mu} - i v_{g,\mu} \frac{\partial}{\partial x} \right) c_{\mu}(x) \quad 2.17$$

$$\hat{H}_{\text{coupler}} = \int dx \delta(x) \left[V c_{\mu}^{+}(x) \hat{a}_{\mu} + V^{*} \hat{a}_{\mu}^{+} c_{\mu}(x) \right] \quad 2.18$$

$$\hat{H}_{\text{ring linear}} = \omega_{c,\mu} \hat{a}_{\mu}^{+} \hat{a}_{\mu} \quad 2.19$$

$$\hat{H}_{\text{ring nonlinear}} = \sum_{\mu 1, \mu 2, \mu 3, \mu 4} S_{\mu 1, \mu 2, \mu 3, \mu 4} \hat{a}_{\mu 1}^{+} \hat{a}_{\mu 2}^{+} \hat{a}_{\mu 3} \hat{a}_{\mu 4} \quad 2.20$$

where $\left(\hat{c}(x), \hat{c}^{+}(x)\right)$ are the position dependent inverse Fourier representations of the usual Boson ladder operators describing the rightward traveling waveguide mode, and $\left(\hat{a}, \hat{a}^{+}\right)$ are the Boson ladder operators describing the counter-clockwise cavity mode. The canonical commutation relations for the system are $\left[\hat{a}, \hat{a}^{+}\right] = 1$, $\left[\hat{c}(x), \hat{c}^{+}(x')\right] = \delta(x - x')$; $\left[a, \hat{c}^{+}(\hat{x})\right]$ and all other combinations vanish. In using this form of the effective Hamiltonian we are assuming that the waveguide is driven at a frequency within a narrow range far from the cutoff frequency of its dispersion relation, S is the coefficient describing the nonlinear frequency conversion process, and that v_g is the group velocity for the traveling waveguide mode [52]. The evanescent coupling is represented by the

local interaction term having coupling strength $|V|$ where the coupler is situated at x = 0. The different modes represent the four photons interacting during the process (pump-1, pump-2, signal, and an idler).

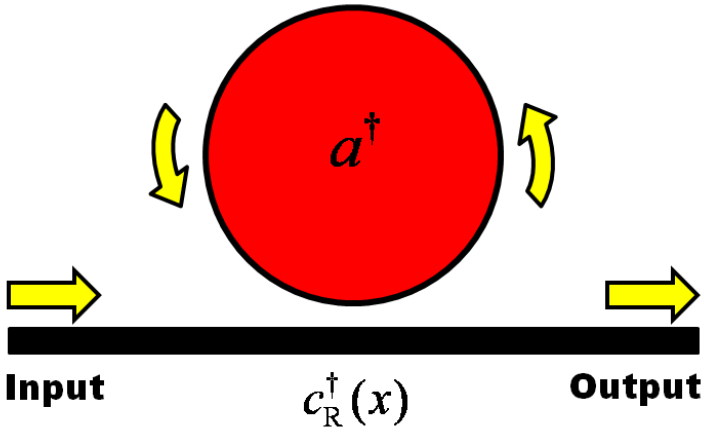

Fig.2.9. Schematic of waveguide-cavity coupled system.

Considering the case where the pump photons have the same energy, we can express its distribution as a coherent state at the coupler where all the interactions happen.

$$\left|\Phi_{In}\right\rangle = O_{in}\left|vac\right\rangle \qquad 2.21$$

The operator O_{in} creates the input state from vacuum. For example the input pump can be considered to have a Gaussian-like distribution $\varphi_P(k) \sim e^{\left(\frac{k-k_p}{2\Delta k}\right)^2}$. Now the generated state is a 2-D distribution depending on the parameters of the generated photons.

$$\left|\Phi_{gen}\right\rangle = O_{gen}\left|vac\right\rangle \qquad 2.22$$

The operator O_{out} takes into count all the energy transfers in the system and generates the output state. The wave vectors can be also related to the distribution of the wave function in k-space [69]. Finally by solving the problem at the coupler through relating the number of photons generated in each mode we find a similar expression for the

photon generation efficiency similar to the classical case $P_{idler} = \eta_{SPFWM} P_{signal}$ and $\eta_{SPFWM} = \eta_{classical}$. The main difference is that the signal power for the conversion is initially provided by vacuum fluctuations instead of a defined input power as the classical case [69].

$$P_{idler} = \eta_{SPFWM} \cdot P_{fluctionatons} = \eta_{SPFWM} \cdot \frac{hf_0 v_g}{(2L)(FE)^2} \qquad 2.23$$

A schematic of the process is shown in Fig.2.10

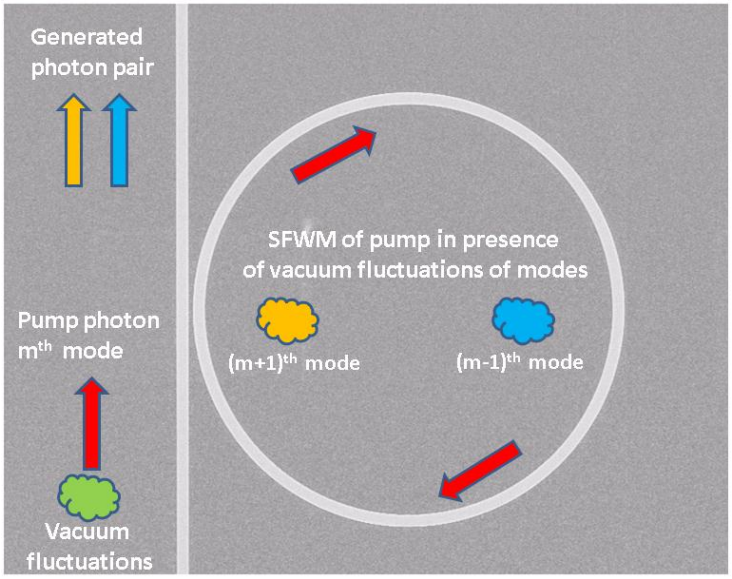

Fig.2.10 Schematic of photon pair generation in SOI ring resonator.

2.3.1 Theoretical model

Following the theoretical we used the setup shown in Fig.2.11 to generate correlated photons in a ring resonator with small free spectral range.

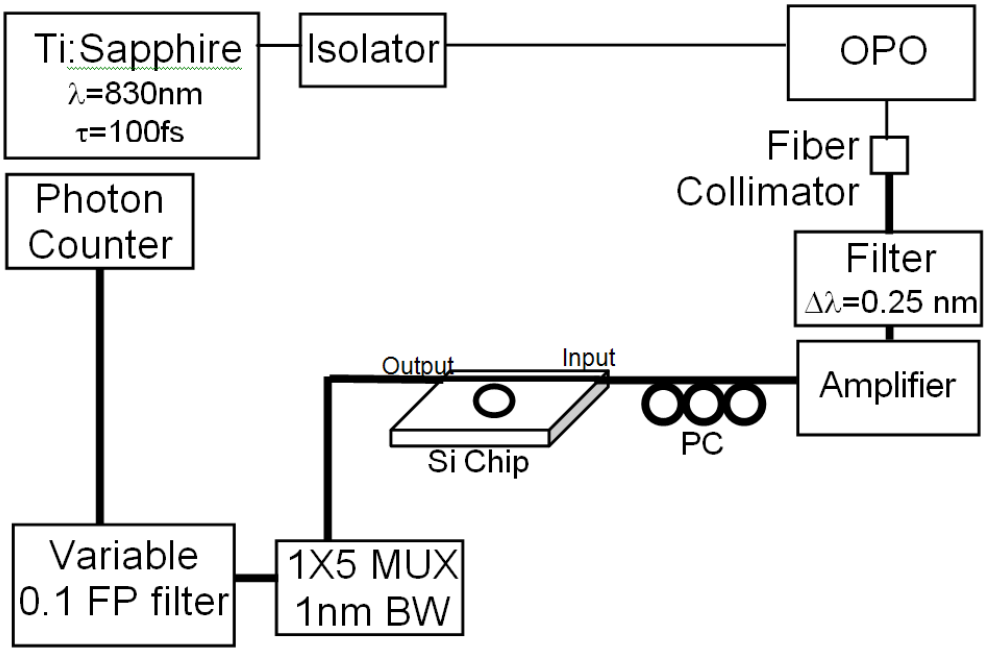

Fig.2.11 Experimental setup for generating correlated photons in silicon chip.

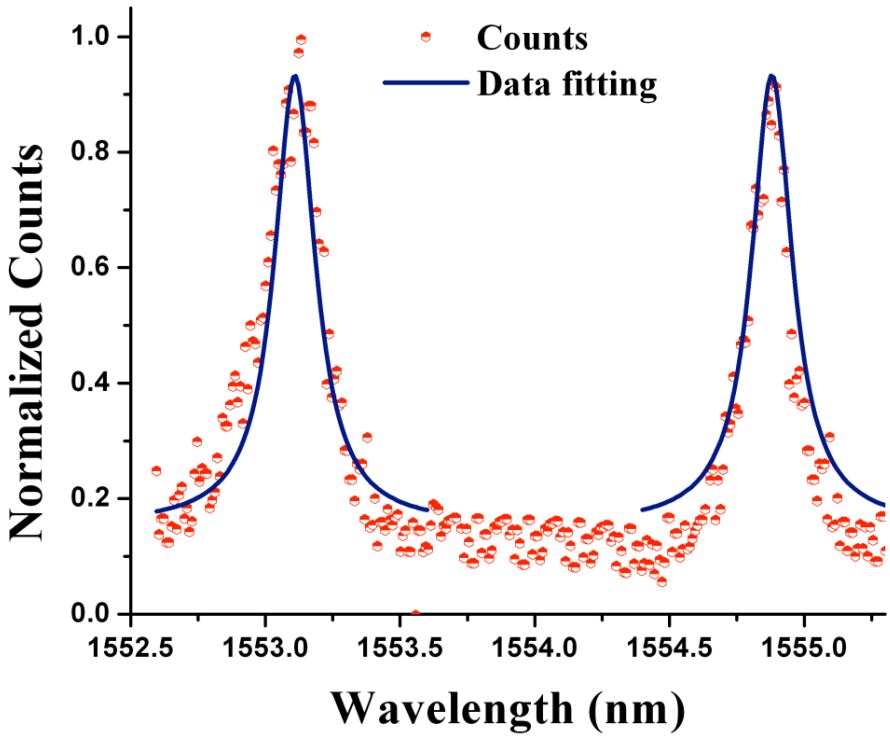

Fig.2.12 Correlated photons generation in silicon micro-ring resonator.

The filtered signal from the OPO is amplified before being coupled to a specific

resonance in the ring. The ring has a FSR of 0.85 nm, which will result in a separation between the idler and signal photons of ~1.6nm. At the output, we initially used 1X5 MUX to eliminate the pump with 70dB extinction ration. Then fine scanning of the wavelength was done using a voltage controlled FP filter with bandwidth of 0.1nm. The results from the single photon counter are shown in Fig.2.12.

There are two main challenges with SPDC sources in general. The first problem is the random nature of the generation of single photon pairs in time. This can solved by using a pulsed pump operation as shown above which will result in a narrower probability distribution of the photon pair generation. This is limited by the duration of the input pump. The second problem is the rate of generating single photon pairs versus higher order conversion specially while operating with high gain. This is closely related to Poisson's statistics of the pump. The probability of multiple pairs scales with the square of the probability of producing a single pair.

$$P_n = \frac{\overline{N^n} e^{-n}}{n!} \qquad 2.24$$

Simply by taking $\overline{N=1}$ we can find a probability of having a single photon per pump to be P1=0.37. For this reason, pulsed SPDC is normally operated at low power, and obeys a trade-off between the count rate and quality of the heralded single photon pairs. This limitation can be overcome by using spatial or temporal multiplexing of several sources [70].

With the single photon source in hand different exciting quantum phenomena can be explored ranging from time bin entanglement [71], polarization entanglement [72], N00N reduced de-Broglie wavelength [73].They essentially depend on creating a number state

that is in general represented by

$$|\Phi\rangle = \sum \alpha_n |n\rangle \qquad 2.25$$

Using simple linear optical elements these states can be manipulated. Taking for example a single photon state input to a MZ interferometer, by efficiently changing the phase of the state and combining the two paths, interference patterns are observed.

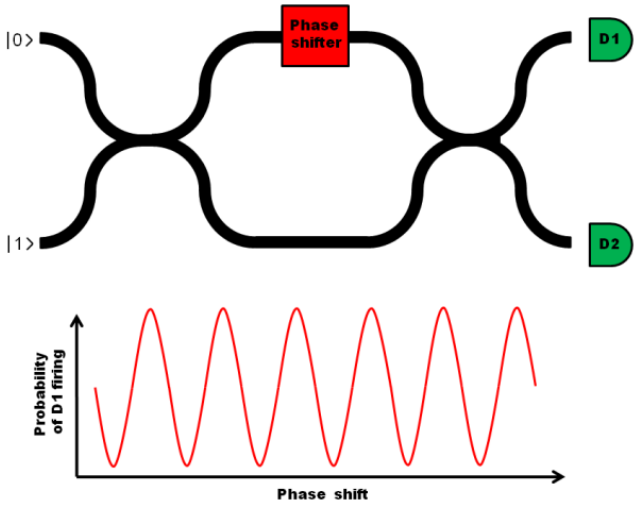

Fig.2.13 Single photon interference in MZI.

The probability of either detector 1 or 2 fires depends sinusoidally on the phase between the two arms

$$P_{01} = \frac{1}{2} \cdot (1 - \cos\theta) = 1 - P_{10} \qquad 2.26$$

Another exciting class of quantum circuits to explore are the photon number dependent switches. Relying on the fact that the effective wavelength of light changes as the number of photons involved in the state is changed. This phenomenon is apparent in N00N states inference patterns which scales in a MZ interferometer configuration with the number of photons [74].

$$Detection \sim \cos(N\phi) \qquad 2.27$$

The general form of this state at the output of a MZ interferometer with a phase shifter is

$$|\Phi\rangle = |0\rangle|N\rangle + |N\rangle|0\rangle \tag{2.28}$$

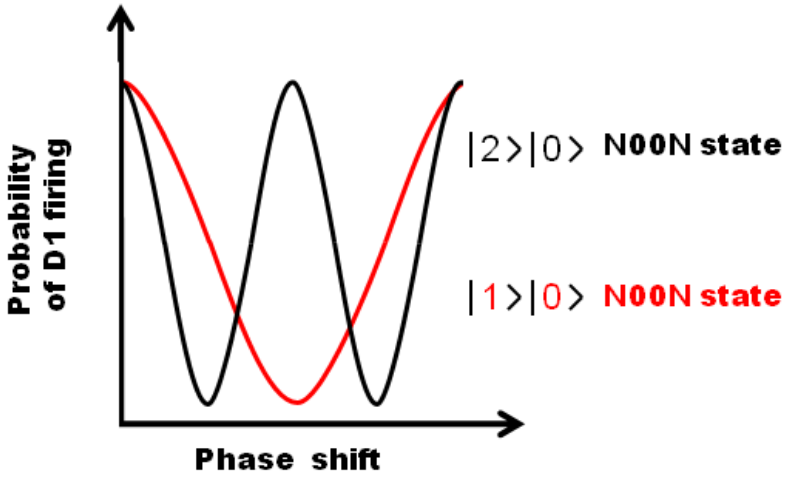

Fig.2.14 Interference pattern dependence on the number of photons.

2.4 Summary

In this chapter we have developed a static and dynamic model describing the interaction between single photon wavepackets and micro-optical cavities. We presented FDTD simulation method of the system that is general and can be used for any arbitrary wavepacket and system condition. In addition, the theoretical results were demonstrated experimentally by showing interference in a system of two micro-ring resonators. We also reviewed the theoretical model for generating photon pairs from vacuum fluctuations in a silicon micro-ring resonator. Following the theoretical model, we have experimentally generated photon pairs in silicon through 4-photon scattering.

In the following chapter, we will focus more on the changes the wavepacket exhibits in the presence of active tuning in the system.

CHAPTER THREE

PHOTON EIGEN ENERGY MANIPULATION

3.1 Introduction

We examine the possibility of dynamically tuning the wavelength of a *single photon* via adiabatic following. The model that we are considering here is similar to the one in Chapter 2 except that we now allow for the dynamic tuning of the resonance frequency of the ring resonator, mathematically by allowing ω_c in the effective Hamiltonian (equation 2.1) to become a parametric function of time, $\omega_c(t)$. The system is shown schematically in Fig.3.1where the change in the color of the cavity from its color at t_0 depicts the change of the cavity resonance frequency. Clearly, the parametric change in the system affects only the harmonic oscillator (free ring resonator) term of the effective Hamiltonian. We expect, then, that for a sufficiently slowly varying function $\omega_c(t)$, the wavelength of the cavity will adiabatically follow the parametric shift in the resonance frequency. This has been demonstrated theoretically and experimentally, by, among others, one of the present authors (SP), in the case of classical electromagnetic waves [32,33,54]. The effect is a clear manifestation of the well-known adiabatic theorem [58], and our mission here is to show, via direct computation, that the phenomenon carries over directly to the fully quantum mechanical case of single-photon transport.

It is interesting to note that for the harmonic oscillator, the fully quantum mechanical import of the adiabatic theorem is fully accessible from semi-classical analysis. Ultimately this is related to the fact that the harmonic oscillator is one of the systems that has perfectly closed orbits in phase space, the trajectory being the energy ellipse, and the

classical adiabatic invariant being the action integral, $\oint pdq = \frac{U}{\omega}$, where U represents the total mechanical energy of an oscillator having natural angular frequency, ω, and the action integral is geometrically equivalent to the area of phase space bounded by the energy ellipse. Semi-classically, the action is related to this adiabatic invariant via the Bohr-Sommerfeld quantization condition from the "old quantum theory," $\oint pdq = N\hbar$. Combining the two expressions for the action integral clearly results in the simple energy quantization condition for the quantized oscillator. It is especially important realize in interpreting our single photon results that, although such simple analysis cannot tell us about the actual quantum *state* of the photon field, in the case of the harmonic oscillator (a realization of which formally represents the single-mode photon field) it does produce exactly the energy *eigenvalues*. It is for this reason that the adiabatic invariant for the fully quantum mechanical Hamiltonian is exactly the same as for the case involving classical fields; this is in fact the underlying reason why the authors of Ref. [30] were able to explain exactly the adiabatic energy shift of a *photon* using only *semi-classical* analysis. Using simple Δ-calculus, it is clear that for any simple harmonic oscillator $0 = \frac{\Delta\left(U/\omega\right)}{U/\omega} = \frac{\Delta U}{U} + \frac{\Delta\omega}{\omega} = \frac{\Delta U}{U} - \frac{\Delta\lambda}{\lambda}$, where the second equality results from our assumption that the oscillator represents a cavity photon, $\omega = \frac{2\pi c}{\lambda}$. Clearly we must have, semi-classically and quantum mechanically, $\frac{\Delta\lambda}{\lambda} = \frac{\Delta U}{U}$. This relationship describes a detailed balance between the energy of the cavity photon and the work done on the system by the external agent that performs the tuning of the cavity resonance; quite aptly, there is a thermodynamically adiabatic transfer of energy from the environment to the cavity.

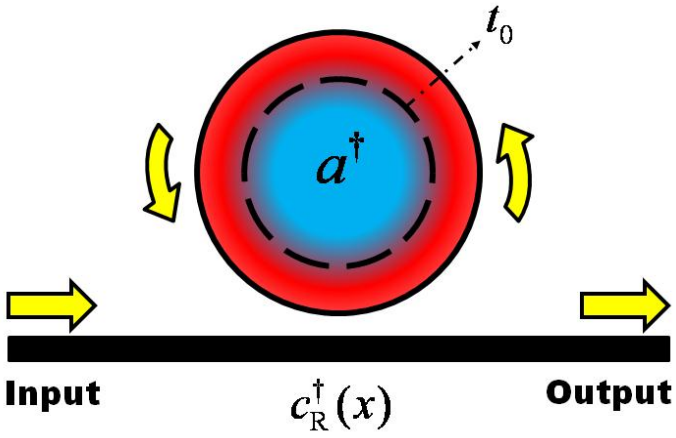

Fig.3.1 Schematic of photon energy lifter. The cavity is adiabatically tuned at time t_0 from one stationary state to another.

3.2 Full Quantum mechanical analysis

We now directly demonstrate the single photon adiabatic wavelength shift and examine its dynamical behavior. To begin, we repeat Eqns. (4) and (5) with the modification to the cavity resonance frequency ω_c,

$$\left(\omega_0 - iv_g\frac{\partial}{\partial x} - i\frac{\partial}{\partial t}\right)\tilde{\phi}(x,t) + \delta(x)V\tilde{e}(t) = 0 \qquad 3.1$$

$$\left(\omega_c(t) - i\frac{1}{\tau_c} - i\frac{\partial}{\partial t}\right)\tilde{e}_{cav}(t) + V^*\tilde{\phi}(0,t) = 0 \qquad 3.2$$

In solving these equations using the numerical algorithm outlined above we will assume a simple linear shift to the resonance frequency, $\omega_c(t) \sim t$. The physical result is insensitive to the exact parameterization, as long as the change is "slow" in comparison with the intrinsic time scale of the system, which in this case set by the inverse of the mode frequency spacing of the ring resonator. Further, it should be experimentally straightforward to dynamically tune a ring resonator resonance at a constant rate over the interesting region of parameter space.

The time evolution equations are solved using the numerical technique described earlier. We first consider wavelength shifts that occur over a time scale smaller than the cavity photon lifetime. In Fig. 3.2 we show our solutions for the cavity photon amplitude function, $\tilde{e}_{cav}(t)$, for several different values of the adiabatic shift starting from negative tuning (left) to positive tuning (right). The evidence of quantum control of the cavity photon wavelength is clear even at the single photon level. We stress that this mechanism for wavelength conversion of a single photon involves only linear optical processes and therefore obviates the need for large nonlinear susceptibilities that is a technological barriers to the development of quantum circuit elements.

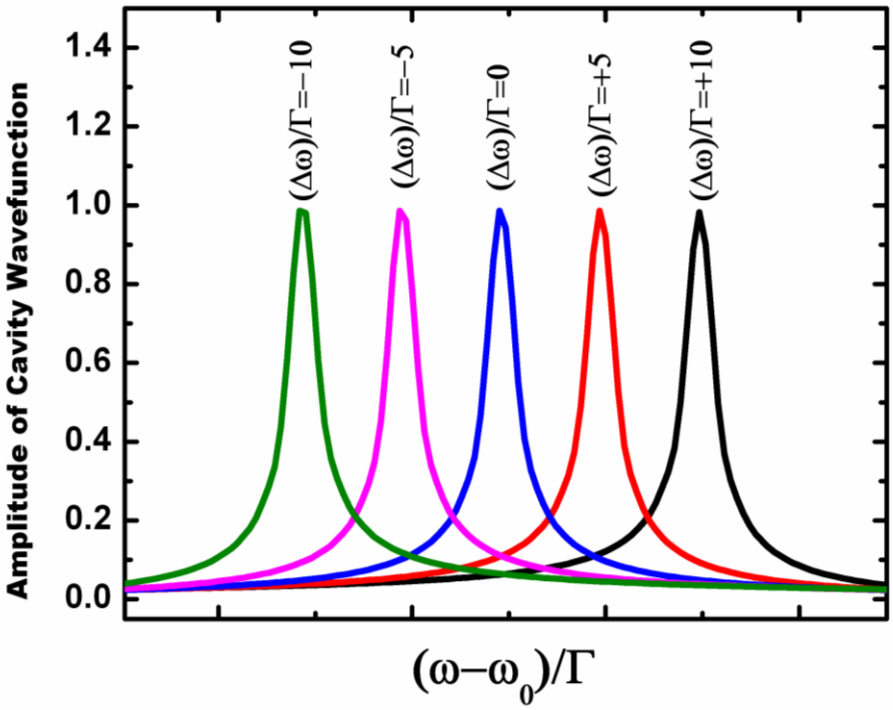

Fig.3.2 Single photon energy state changes adiabatically as a function of the cavity tuning frequency (the tuning changes from negative to positive going from left to right).

Next we study the conversion efficiency as a function of the switching time. The results are shown in Fig.3.3 The switching function is varied linearly with time from the initial state to the final state (the switching time changes from zero to one photon life time going from back to front). We clearly see that as the switching time approaches the time the photon spends inside the cavity there is a lower probability to detect the photon at the new eigenstate. This probability has an upper limit of 1 when the conversion is done in a time $T << \tau_c$. We can understand the degradation in amplitude as the result of a competition between the adiabatic tuning process and the non-adiabatic effect of the finite cavity decay rate we are considering in our model. If the switching time is short, the adiabatic effect dominates (which may seem counterintuitive, but one must recall that adiabatic does not mean "slow" it means without irreversible energy exchange – it just happens that many text book examples of the adiabatic theorem involve slow processes, [75]). On the other hand, if the switching time is comparable to the cavity lifetime, $T \sim \tau_c$, the effects of cavity decay become apparent. Clearly, if $T << \tau_c$, we face the trivial situation of having a very low probability of there being a photon whose wavelength we can hope to shift. We stress here that we are considering micro-cavities with mode frequency spacing that are much larger than the inverse of the relevant time scale for the adiabatic change, $1/T$. We have yet to apply our single photon model to the case in which other modes are accessible and thus excited when $1/T \sim \Delta\omega$. We expect that, as in the semi-classical case, the wavelength conversion will lose fidelity as a result of the distribution of the injected (or extracted) energy over several modes (as experimentally demonstrated [76]) , in turn leading to an increase in the effective entropy of the system (as more microstates, viz. the other modes become available), thus introducing a non-

adiabatic component to the energy transfer. We shall study the details of this more complicated case elsewhere.

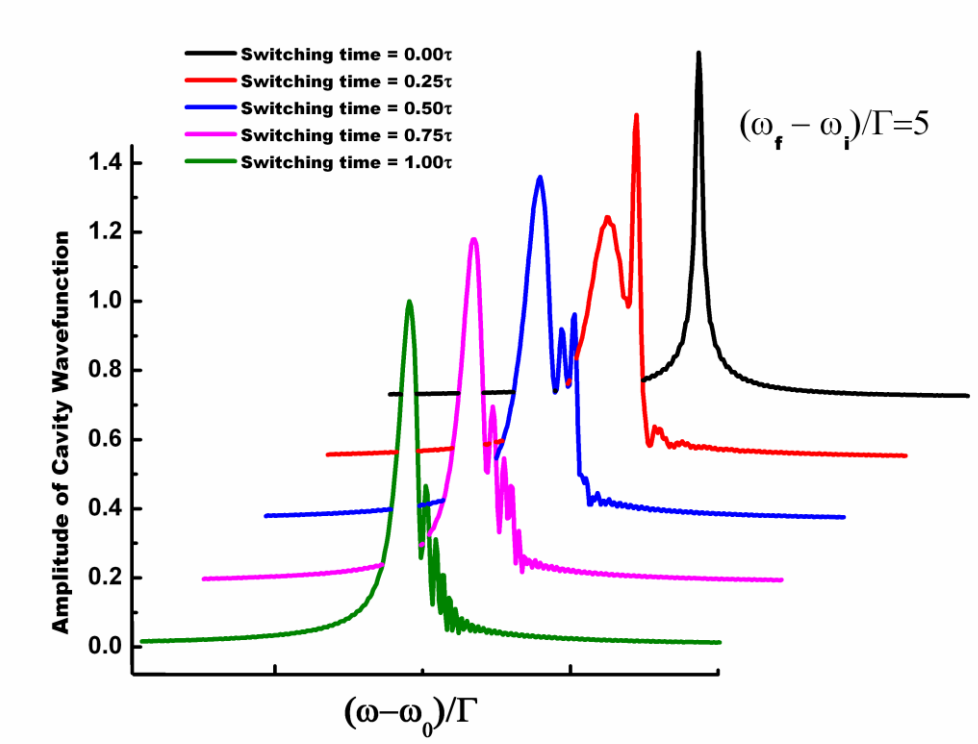

Fig.3.3 Single photon final state as a function of the tuning time. The conversion efficiency degrades with slower tuning (the switching time changes from zero to one photon life time going from back to front).

We now analyze another test to verify that the probability of detecting a photon in the new (old) eigenstate after the conversion is P=1 (P=0). A cavity is placed in series with the dynamic cavity and the experiment is performed twice. Initially, the output cavity is tuned to the original eigenstate and second to the new eigenstate in such a way as to probe the photon energy at the output of the dynamical system. The equations of motion describing the systems can be derived in a way analogous to that discussed in Section II resulting in the system,

$$\left(\omega_0 - iv_g\frac{\partial}{\partial x} - i\frac{\partial}{\partial t}\right)\tilde{\phi}(x,t) + \delta(x_a)V\tilde{e}_a(t) + \delta(x_b)V\tilde{e}_b(t) = 0 \qquad 3.3$$

$$\left(\omega_{c,a}(t) - i\frac{1}{\tau_{c,a}} - i\frac{\partial}{\partial t}\right)\tilde{e}_a(t) + V^*\tilde{\phi}(x_a,t) = 0 \qquad 3.4$$

$$\left(\omega_{c,b} - i\frac{1}{\tau_{c,b}} - i\frac{\partial}{\partial t}\right)\tilde{e}_b(t) + V^*\tilde{\phi}(x_b,t) = 0 \qquad 3.5$$

The numerical results and a schematic of the system considered are shown in Fig.3.4

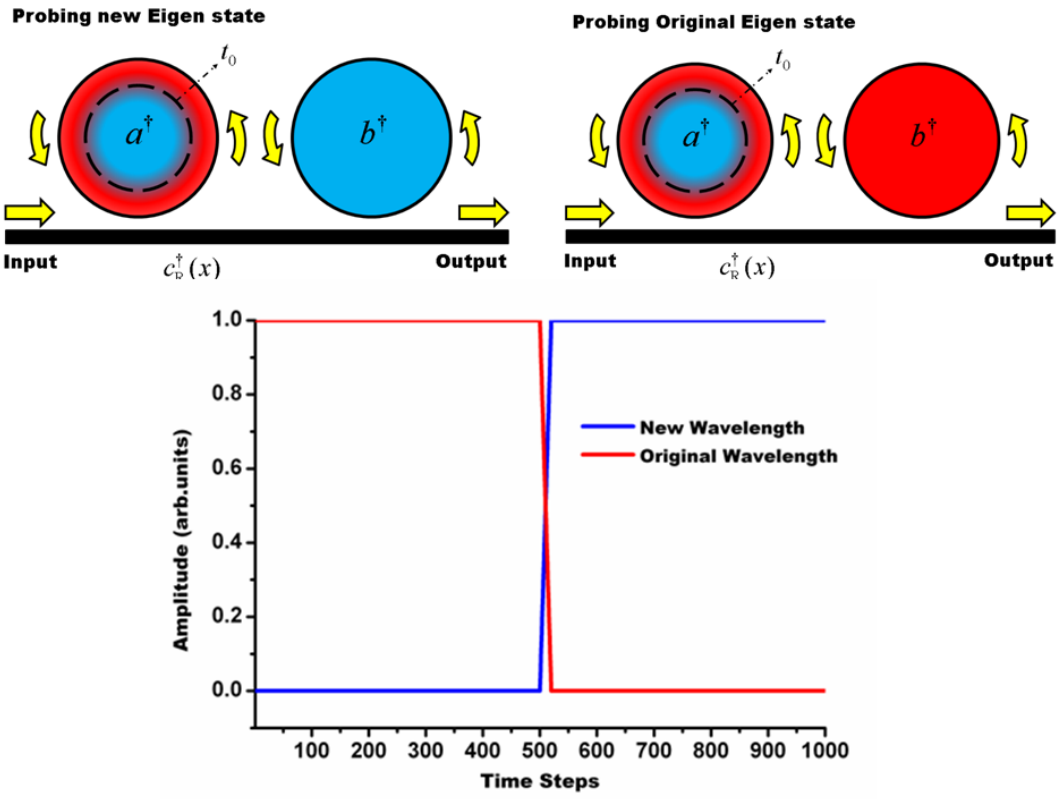

Fig.3.4 The state inside the cavity changes with 100% efficiency. During the transition period the photon follows the state of the cavity (new/old wavelength amplitude changes from 0/1 after the tuning).

We see that the conversion efficiency is 100% with a zero probability of detecting the original photon energy after the conversion process took place. This established that the

wavelength conversion of the single photon is complete and that it leaves the photon wave packet intact.

3.3 Experimental results

The setup of the experiment is shown in Fig.3.5. The systems consist of attenuated optical pulses from an OPO with an average number of photons of 0.1 per pulse. The pulses are coupled to a ring silicon ring resonator through a custom made fiber and a polarization controller. The custom made fiber is used to synchronize the 1550nm pulse with the top pumping at wavelength of 415nm.

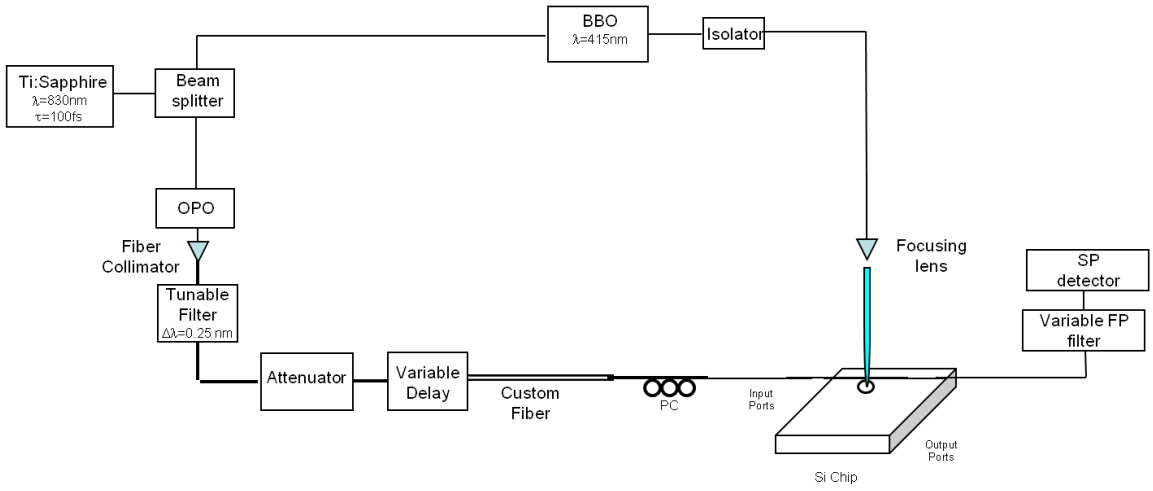

Fig.3.5 Experimental setup for single photon state manipulation through dynamic control of silicon ring resonator.

The experiment goes as follows, when the 1550nm pulses are coupled to a specific mode, the refractive index of the cavity is changed through injection of carriers. The ring used here has a FSR of 0.85nm (diameter of 200 micrometer). This ring size will ensure observing more complex phenomenon which is discrete transitions of photons in the cavity modes.

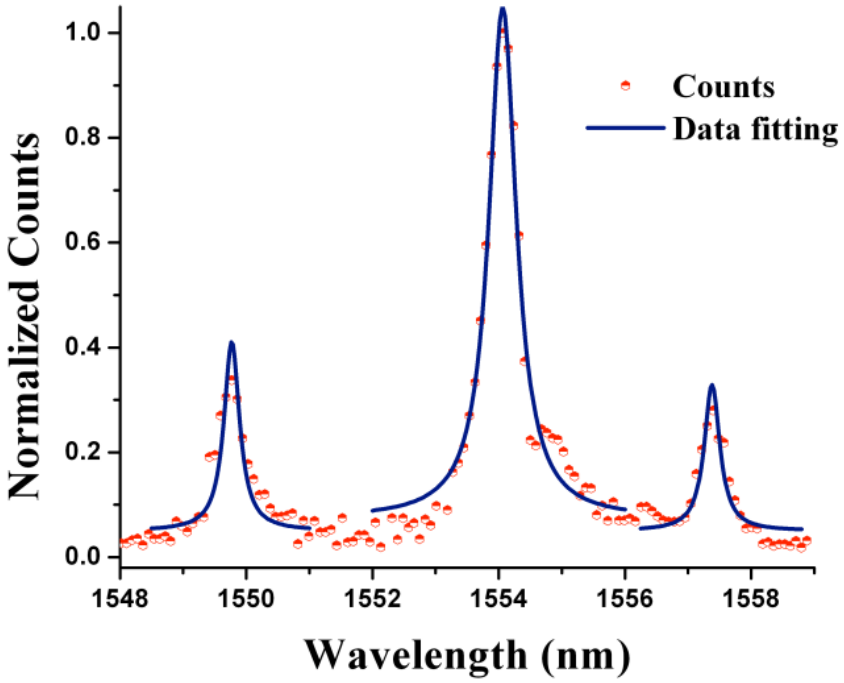

Fig.3.6 Single photon transitions in a ring resonator. The central large peak is the initial wavelength of the photons and is tuned to one resonance. When the resonators is dynamically tuned using the free-carrier plasma dispersion effect the photons make transitions to other resonator states (the two smaller peaks).

The photon-count as a function of wavelength is shown in Fig.3.7. There is a dominant adiabatic shift at 1554nm, in addition to discrete transitions to higher energy (1550nm) and lower energy (1557nm) modes. As will be explained in Chapter 5, certain transitions can be made more probably by carefully designing the photonic states.

3.4 Summary

In this chapter we studied the effect of dynamic tuning of a resonator on a trapped photon wavepacket. The theoretical result follows the adiabatic invariance principle; it manifests itself as changing the eigen energy of the photon. We also studied the effect of the modulation speed on the final state of the photon. Following the theoretical model, we experimentally demonstrated discrete photonic transitions in a cavity with closely spaced modes.

CHAPTER FOUR

PHOTON TRAPPING IN EIT-LIKE SYSTEMS

4.1 Introduction

Delay elements play an important role in quantum computing [77,78] and optical signal processing [79,80] which calls for the need of efficient controlled delay elements with large characteristic storage time. Passive optical delay lines have a fundamental tradeoff between the bandwidth they can accept and the amount of delay they can deliver [81-83] . In order to break this limit dynamic tuning from an initially large bandwidth state (small group index) to a narrow bandwidth state (large group index) is required [28,29,84,85]. Recently such systems were demonstrated on a silicon chip using an all-optical analogue of electromagnetically induced transparency (EIT) [28,86] and a coupled cavity-mirror system [85]. However, the amount of delay demonstrated was significantly limited to much less than one-hundred picoseconds [28,85]. This small amount of delay is due to the absorption of the stored light by the free-carriers that are inherently required to dynamically capture, store and release the pulse of light. Here we propose a novel solution to this problem by separating the primary functionalities (capture, storage and release of the light pulse) of the light storage system into separate cavities. By doing so we can ensure that the light only minimally interacts with free-carriers. As a result we experimentally demonstrate delay that can be continuously varied over ~300ps (with an intrinsic exponential decay time of ~160ps). The delay achieved in our system is four times larger than previously demonstrated active optical delays [28,86]. Our technique is

only limited by the quality of the cavities used and can be easily extended to nanosecond delays with lower-loss cavities which inherently have a longer photon life time [57].

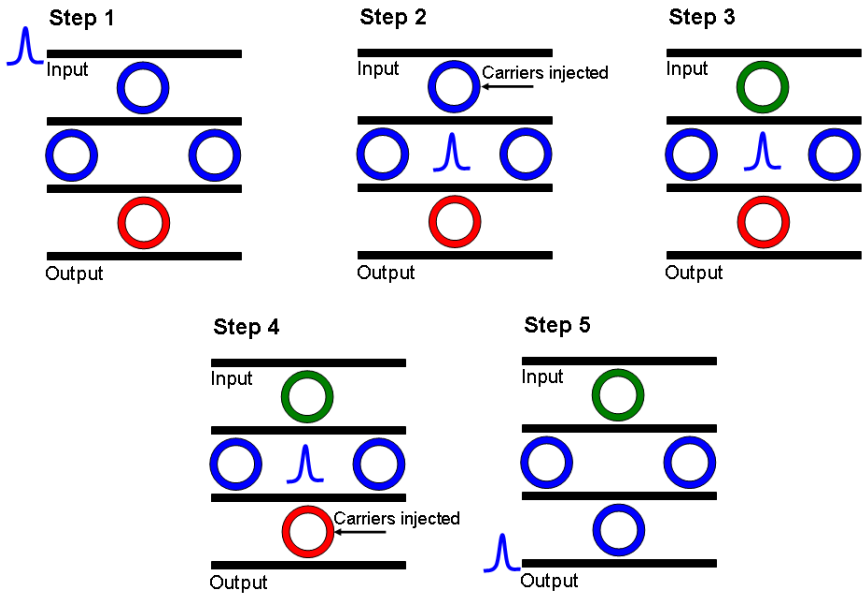

Fig. 4.1 Schematic the system and its operation principle, (Step 1) shows the acceptance state of the system. Bits are stored as shown in (Steps 2 and 3) then released in (Steps 4 and 5).

Our proposed scheme for achieving tunable delay is shown in Fig. 4.1. It consists of three rows of resonators. The first and last rows are used to capture/release a pulse of light into/from the system. The middle row is the low loss storage unit where the light circulates until it is released and is equivalent to the EIT structure in [28]. The system works as follows: 1) Capture stage: Light is input into the large-bandwidth capture switch represented by the top cavity (Fig.4.1-Step 1). The capture cavity initially has the same resonant wavelength as the storage unit so light automatically couples into the storage unit. 2) Storing stage: Once the light is completely in the storage unit the resonant wavelength of the capture switch is detuned by injecting free-carriers (cavity color changes from blue to green as seen in Steps 2 and 3). This effectively decouples the light

from the input/output waveguides, which dramatically increases the group index of the system. In addition, the light is isolated from the free-carrier loss used to tune the system. This is the key for achieving the large and low loss delays demonstrated here. 3) Release: The signal can be released at any time by injecting carriers into the release switch (the ring in the third row). This aligns its resonance (color changes from red to blue in Fig. 4.1 Steps 4 and 5) with the storage unit resonance. The light automatically leaks out into the output cavity and then into the output waveguide.

In order to prove that our device is insensitive to free-carrier loss we used time domain coupled mode theory to compare our design with the previously demonstrated EIT delay element [28]. The following describe the equations used to model the time evolution of a field a inside a resonator that is evanescently coupled to two waveguides with fields $E^{through}$ and E^{drop}, respectively [87].

$$\frac{da}{dt} = (j\omega_o - \frac{1}{\tau_{int}} - \frac{1}{\tau_{through}} - \frac{1}{\tau_{drop}})a + j\kappa_1 E_{In}^{\ through} + j\kappa_2 E_{In}^{\ drop} \quad 4.1$$

$$E_{Out}^{\ through} = E_{In}^{\ through} - j\kappa_1^{*} a \quad 4.2$$

$$E_{Out}^{\ drop} = E_{In}^{\ drop} - j\kappa_2^{*} a \quad 4.3$$

where ω_o and $\kappa_{1,2}$ are the resonance frequency of the cavity and the coupling coefficient from through/drop waveguides to the resonator, respectively. The times τ_{int}, $\tau_{through}$, and τ_{drop} represent the field decay constants through internal cavity loss, coupling to the through port, and coupling to the drop port, respectively. Eq. (4.1), (4.2) and (4.3) were applied to each of the cavities in Fig. 4.1 and they were coupled to each other by appropriate waveguide amplitudes (Et^{hrough} and E^{drop}). In addition, we assumed that there was no internal cavity loss in order to highlight the effect of free-carriers and also let

$\kappa_1=\kappa_2$ for simplicity. □□□To model the effects of the free-carriers during the capture/release steps we applied Eq. (4.4), (4.5) and (4.6) to the evolution of the field a in the resonator over one round trip:

$$a(l) = a_o e^{-j\Delta\beta l + 0.5\Delta\alpha l} \quad 4.4$$

$$\Delta\beta = \frac{2\pi}{\lambda}\Delta n_{neff} = \frac{-2\pi}{\lambda}(8.8\times10^{-22}\Delta N + 8.5\times10^{-18}\Delta P^{0.8}) \quad 4.5$$

$$\Delta\alpha = 8.5\times10^{-18}\Delta N + 6.0\times10^{-18}\Delta P \quad 4.6$$

where ΔN cm-3 (electrons) and ΔP cm-3 (holes) are the injected carrier densities, and Δβ and Δα represent the changes in the propagation and attenuation constants in a waveguide with effective index neff and length l (which is the circumference of the resonator) [28,88]. The results of the coupled mode simulations are seen in Fig. 4.2. Light is captured in the storage unit at t~100ps and released at t=700ps. By comparing Fig. 4.2A (our design) and Fig. 4.2B (EIT) it is clear that our system stores the light signal in the system for a considerably longer time (potentially as long as 4.5ns in this example which is solely limited by the very small coupling to the capture switch in Step 3) than the comparable EIT system. This is even with the order of magnitude larger carrier density (5E18 cm-3) used in this example (and consequently order of magnitude larger absorption coefficient). And this free-carrier loss insensitivity applies for a very large range of carrier concentrations as plotted in Fig. 4.3 where the stored power is negligibly affected by the increase in the injected carrier density in our proposed scheme as compared to the fast decay with increasing the injected carrier density in the EIT structure [28]. Therefore, it is clear that by separating the capture/storage/release processes our system can be made insensitive to free-carrier loss.

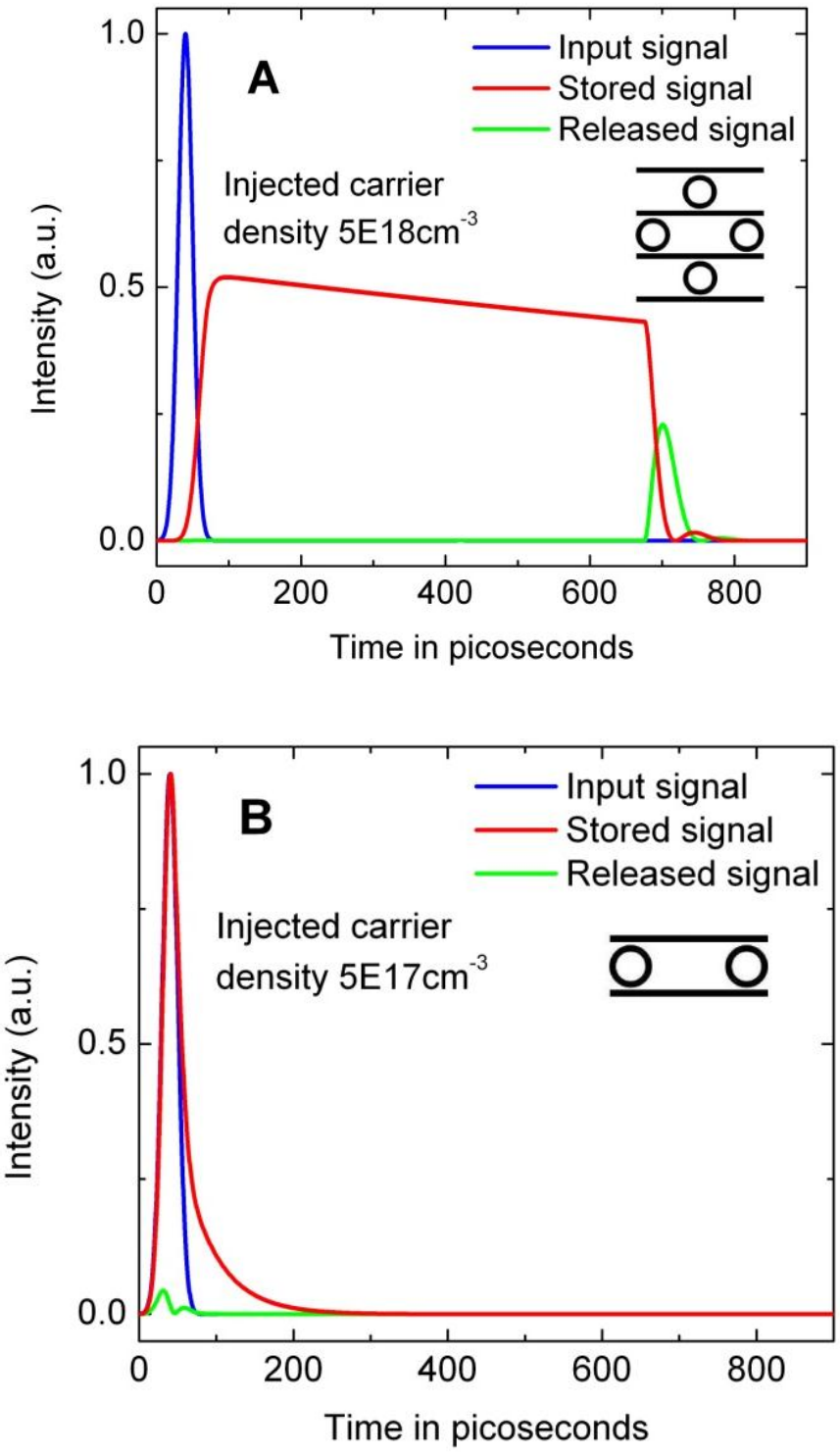

Fig. 4.2 (a) Numerical simulations of storing a 20ps pulse in the proposed system with an injected carrier density of 5E18cm-3. (b) Same data is stored in the EIT device proposed in [28] with an injected carrier density of 5E17cm-3.

While the EIT structure could avoid the free-carrier loss by operating in the high free-carrier loss state initially and then switching to a low loss state for storage (by pulling carriers from the system) the carriers would need to removed from the system in a time less than one photon life time of the rings (with the high loss), which is not realizable with current electro-optic modulators [88].

One tradeoff of our approach is that the resonances need to be shifted farther than in the EIT structure. This will require more carriers and consequently more power. In addition, the injected carriers will broaden the capture switches resonance slightly however this effect is minimal (in this simulation the resonance is broadened to $\Delta\lambda$=0.8nm from $\Delta\lambda$=0.3nm with a 6.7nm shift in resonance). However, the higher carrier concentration is an acceptable tradeoff in order to obtain order of magnitude higher storage times.

We see in Fig. 4.2A that approximately one-third of the input signal is released from the system. The first loss occurs in the initial storage of the pulse where we see ~53% of the input power is stored in the system. Approximately one-third of the initial pulse is lost in the input ring during the storage process (Steps 2 and 3) where it is changed to another wavelength via adiabatic wavelength conversion and also absorbed by free-carriers [32]. The remaining loss occurs because when the input ring and EIT mode are initially aligned in Step 1 the presence of the input ring actually disrupts the overall phase of the EIT mode, essentially opening it slightly, which allows some of the light to escape out of the other ports of the storage unit [28,56]. This disruption of the phase of the EIT mode also occurs during the release process when the resonance of the release ring is aligned with the storage unit resonance, which causes the final drop of power seen at t=700ps in Fig. 4.2A. However, we believe the overall efficiency observed in these

simulations is not a fundamental limit of our scheme and can be considerably improved by carefully selecting coupling coefficients and utilizing more cavities in the storage unit [89,90].

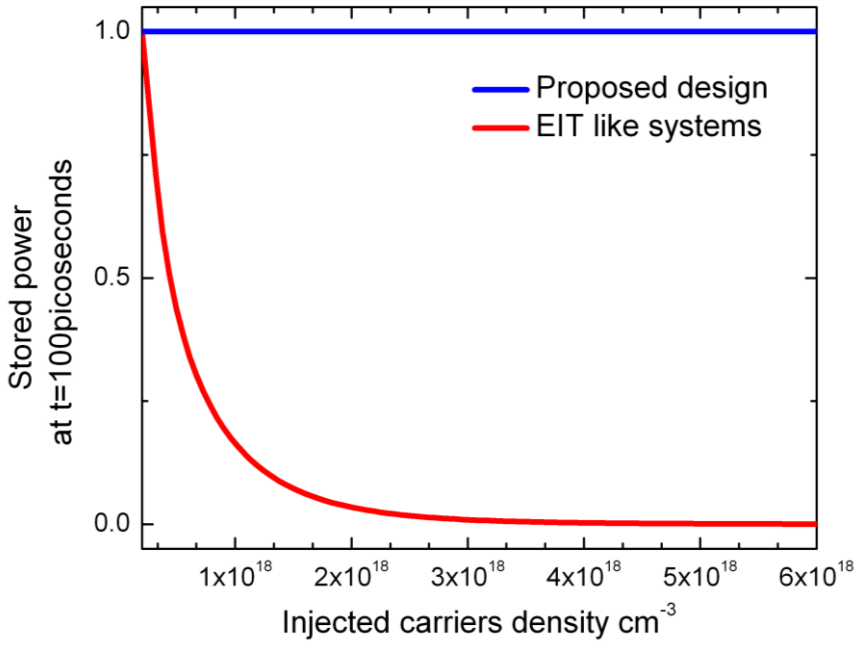

Fig. 4.3 Numerical simulations of the stored power after 100picoseconds in the storage unit with different carrier densities. Our proposed scheme is in blue while a comparable EIT system in red.

4.2 Passive device analysis

We fabricated our proposed delay element on an SOI platform as shown in Fig.4.4 using E-beam lithography (JEOL 9300) with negative resist XR-1541 6%. However, instead of using a separate release cavity we removed it in order to simplify our experimental setup. This is because we found that the cavities have slight variations in the resonance positions from their predicted values due to fabrication imperfections, which can be corrected with thermal tuning. In order to reduce the number of cavities that need to be heated we only use three cavities in the fabricated structure, as opposed to four, which

significantly simplifies our experimental setup. The top cavity still works as a capture switch, and the remaining two make up the storage unit. We can use one of the cavities in the storage unit as a release switch. While carriers need to be generated in this switch our simulations show that the light interacts with these carriers for only a short single photon lifetime of the cavity, which only induces a small power loss [32,91].

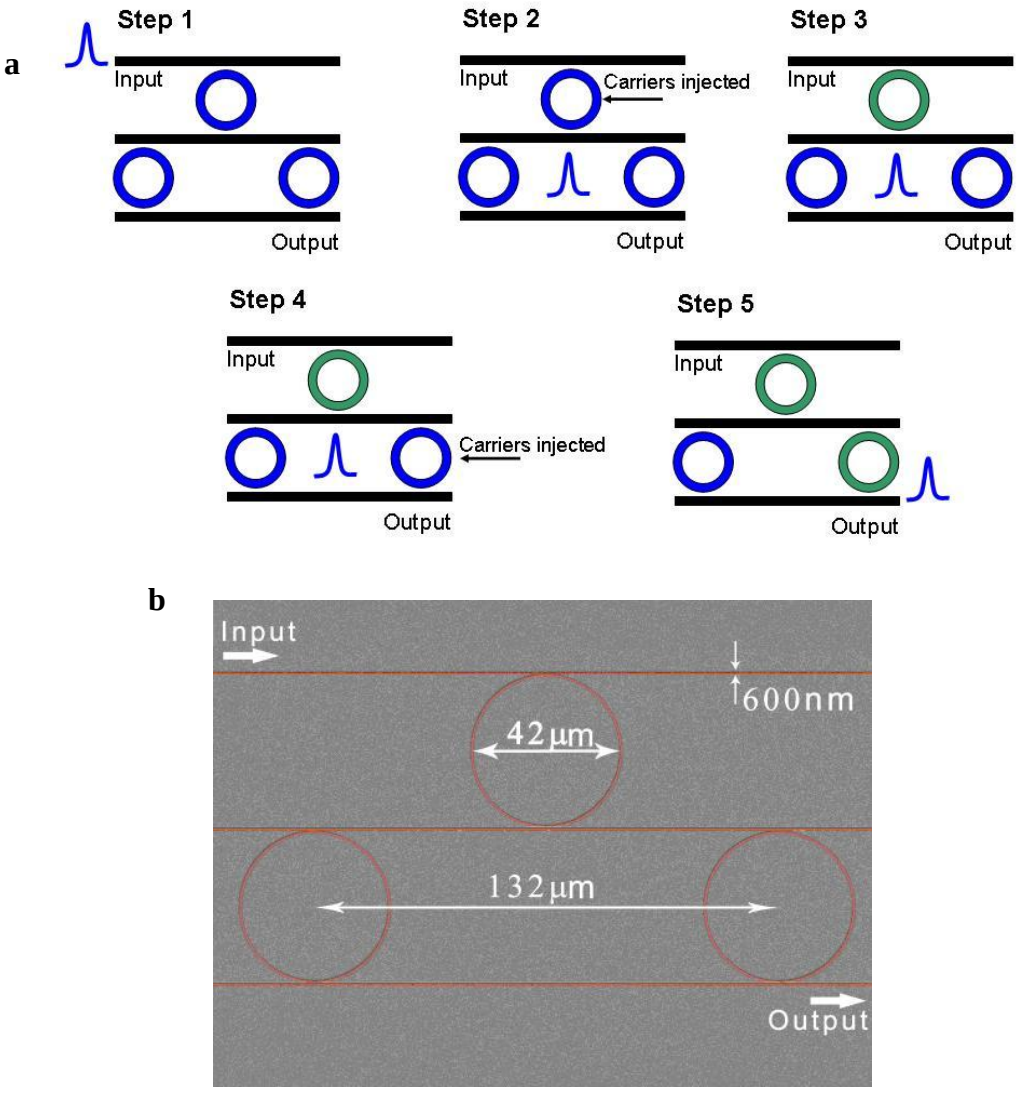

Fig. 4.4. (a) Schematic of the capture and release process of the three ring system similar to Fig.4.1. (b) Scanning electron microscope image of the fabricated device with three ring resonators.

The fabricated rings have a diameter of 42μm with a separation between the two storage rings of 132μm. The rings diameter and their separation were chosen to ensure constructive interference of the storage units supermode [28]. The waveguide dimensions are 250nm in height and 600nm in width in order to increase confinement of the mode and consequently minimize the loss from scattering along the rough etched sidewalls of the waveguides. In addition, the input ring and one of the storage unit rings (used as an output switch) were designed to have a slightly smaller diameter (ΔR=-3nm). This will deliberately locate the resonances at shorter wavelength to allow for subsequent red-tuning. In the switching process the applied heat from carrier recombination shifts the resonances to the correct position (all three rings in resonance).

In order to couple data from the input port into the storage unit all the cavities in the system should have the same resonance. The loaded Q of the rings were measured to be 5000 with an intrinsic Q of 200,000 ($1/Q = 1/Q_{\mathrm{int}rinsic} + 1/Q_{coupling} \approx 1/5000$). To align them we applied heat [8] . (supplied by the external laser used to switch the cavities as explained in following sections) to the top input ring and one of the storage unit rings, both of which are designed to be initially blue-shifted. Fig.4.5 shows the transmission through the middle port of the device with different heating. The initial resonances with no heating are shown in Fig.4.5.A. It consists of an "open" EIT mode of the storage unit superimposed on the input ring transmission dip to the left the EIT peak. In order to move to a closed EIT state for storing data, heating is applied to the blue shifted storage ring (ring with slightly smaller radius initially) as shown in Fig.4.5.B. Consequently, the EIT peak will vanish creating a large photon life time state of 165ps for data storage [28]. There is still some leakage to the capture ring, however it is very minimal provided this

ring resonance is shifted enough in the capture step. The final step is to align the input ring to the storage unit in order to couple light into the storage unit. The transmission after red shifting the input resonance is shown in Fig.4.5.C.

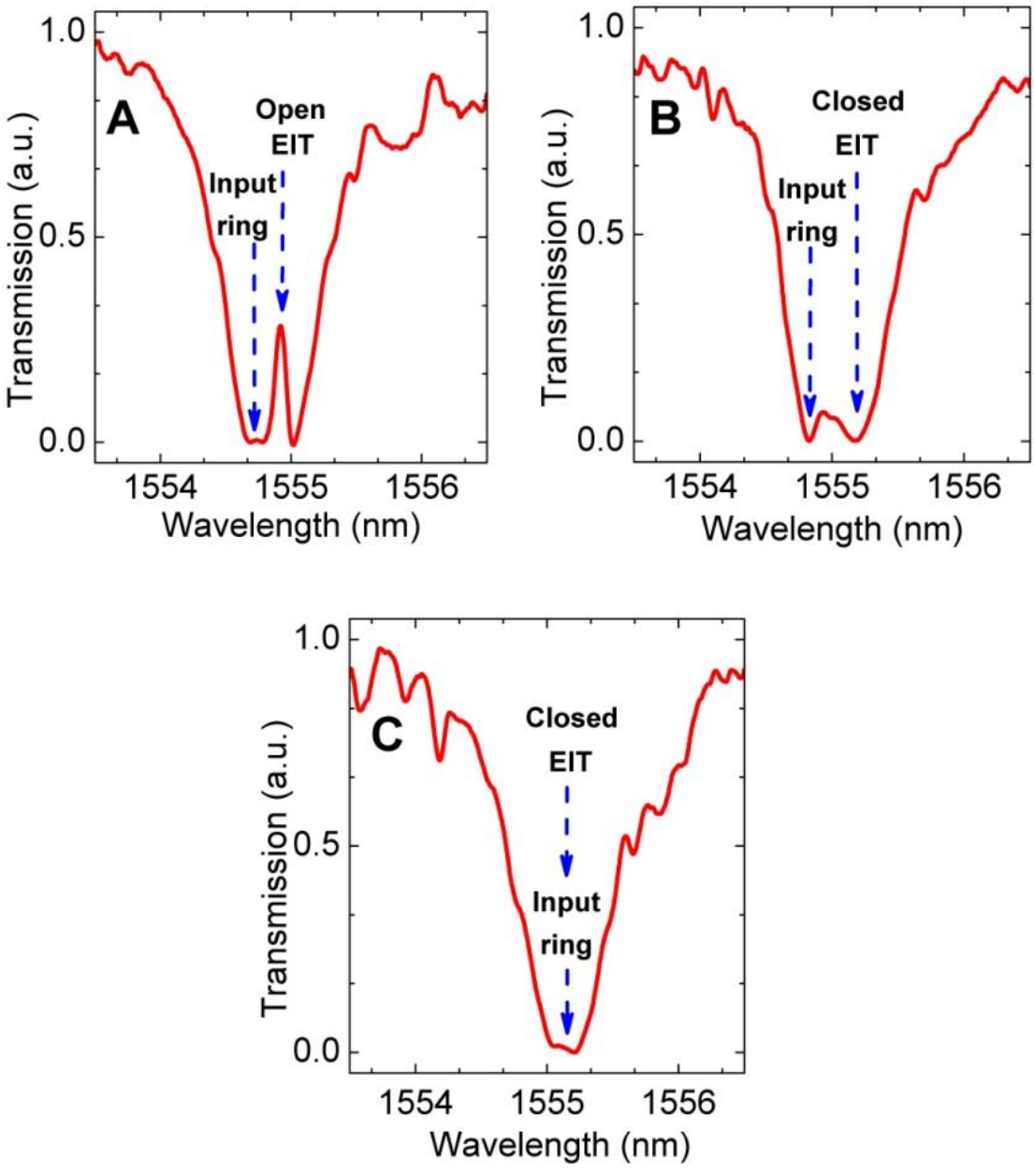

Fig. 4.5 (A) Shows the transmission through the middle waveguide without heating (Open EIT), while (B) shows the transmission with heating of the blue storage ring (Closed EIT), finally (C) depicts the case when all the rings are approximately in resonance through heating of the input ring and the blue storage ring.

The small peak in the transmission spectrum in Fig.4.5.C at ~1555.2nm results from imperfect alignment of resonances. Unfortunately, the heat from the external laser was not enough to force all the resonance to align perfectly. The misalignment could be avoided in future designs by ensuring that the resonances are better-aligned initially.

4.3 Dynamic photon trapping

We can now store and release pulses of light now that the resonances are aligned by heat. The complete experimental setup is shown in Fig.4.6. It consists of a Ti:Sapphire laser generating 100fs pulses at a repetition rate of 80MHz. The pulses are centered at a wavelength of 830nm. The pulses are split using a 50/50 splitter. One half will be used to generate the bit to be stored at 1550nm telecom wavelength. The second half will generate the storage and release pulses at a wavelength of 415nm, which is efficiently absorbed by silicon micro-cavities The first half of the 830nm pulse is converted to 1550nm using an OPO (optical parametric oscillator). The resulting signal is very broadband (~22.5nm due to the short ~200fs pulses) so the bandwidth of the pulse is reduced to match that of the rings in the system using a 0.25nm Tunable Grating Filter (JDS Uniphase TB3). To compensate for the 20dB reduction in the power after the filter an EDFA (Erbium doped fiber amplifier) is used. To eliminate the spontaneous emission noise from the EDFA we use another filtering stage with a bandwidth of 0.5nm. A variable delay line is then used to synchronize the data with the storage and release pulses. Next the pulses polarization is rotated to the TM state (E-field perpendicular to the chip) using a polarization controller and launched into the chip where it couples into the storage unit through the input ring. When the pulse is released it is detected with a fast photodetector (impulse response of ~33ps) and then recorded on an oscilloscope.

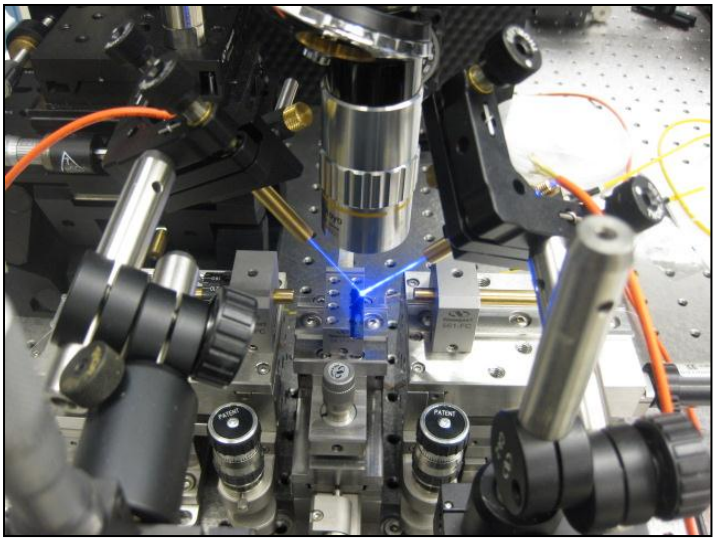

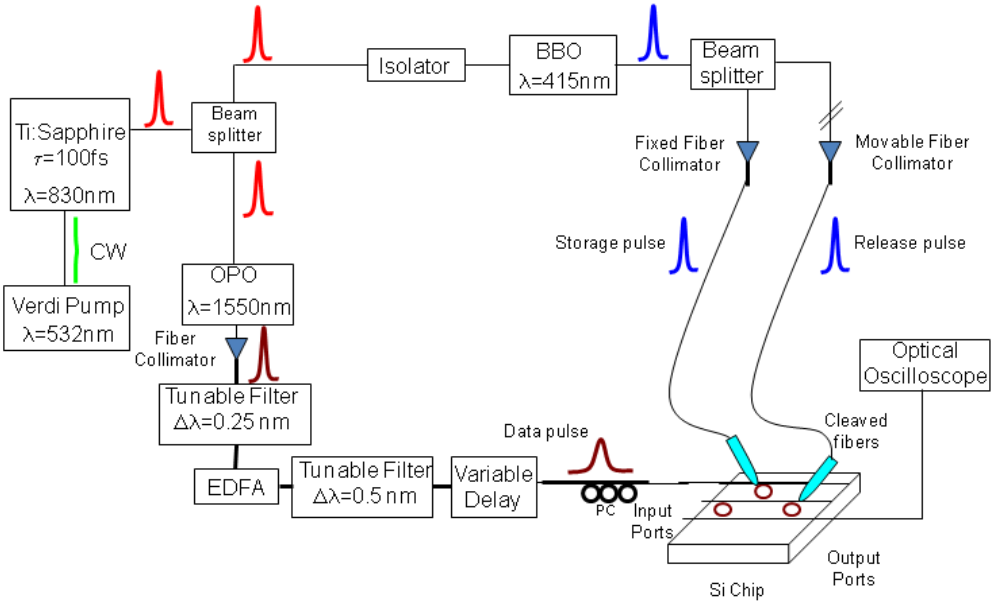

Fig. 4.6 Experimental setup.The stored pulses are generated in an OPO crystal from 830nm Ti-Sapphire laser, while SHG is used to generate 415nm storage and release signals.

The second part of the 830nm pulses is converted to high energy blue light in order to switch the silicon cavities through linear absorption (which generates free-carriers). First the 830nm pulses pass through an Isolator to prevent any back reflection to the laser. Then 415nm blue light pulses are generated through SHG (second harmonic generation)

in a BBO (beta barium borate) crystal. The resulting 415nm pulses are split using a 50/50 beam splitter where one half (store pulse) is used to store the light in the system and the second half (release pulse) is used to release the 1550nm light from the system at any arbitrary time (the time is adjusted with a translation stage). Both 415nm pulses are coupled to equal length fibers with cleaved ends which are placed in close proximity to their respective input/storage ring. While the pulses are short (~100fs) they induce a steady-state amount of heat via phonons produced by carrier recombination which is also used to tune the resonance positions as discussed in the previous section.

4.4 Experimental Results

As discussed earlier the data is stored and released in the following manner: First the 1550nm pulse is coupled through the input ring to the storage unit in the closed EIT state. While the data is inside the storage unit the 415nm storage pulse switches the input ring decoupling it from the storage unit. The stored data is released from the system at any time by opening the EIT mode using a release pulse which switches one of the storage rings slightly off-resonance. The spot size of the switching pulses is 50μm in diameter with an overlap of 4% with each ring. Carriers of concentration 4E17cm-3 are generated in the waveguide through absorbing a pulse of energy of 0.73pJ from the 20pJ incident pulse (assuming 4% mode overlap with the ring). This causes a resonance shift of 0.8nm in the rings which is more than adequate to ensure that there is no coupling to the capture/storage rings in the experiment with a broadening in resonance from 0.3nm to 0.37nm (reduction in Q from 5000 to 4000). The total storage time is controlled by varying the delay between the store and release pulses. As seen in Fig. 4.7 we are able to achieve different storage times which can be continuously varied from zero up to ~300

picoseconds as seen in the specific examples in plots Fig. 4.7A-D (the smaller oscillations in the data come from the impulse response of the detector as independently verified by analyzing pulses of different powers outside the chip).

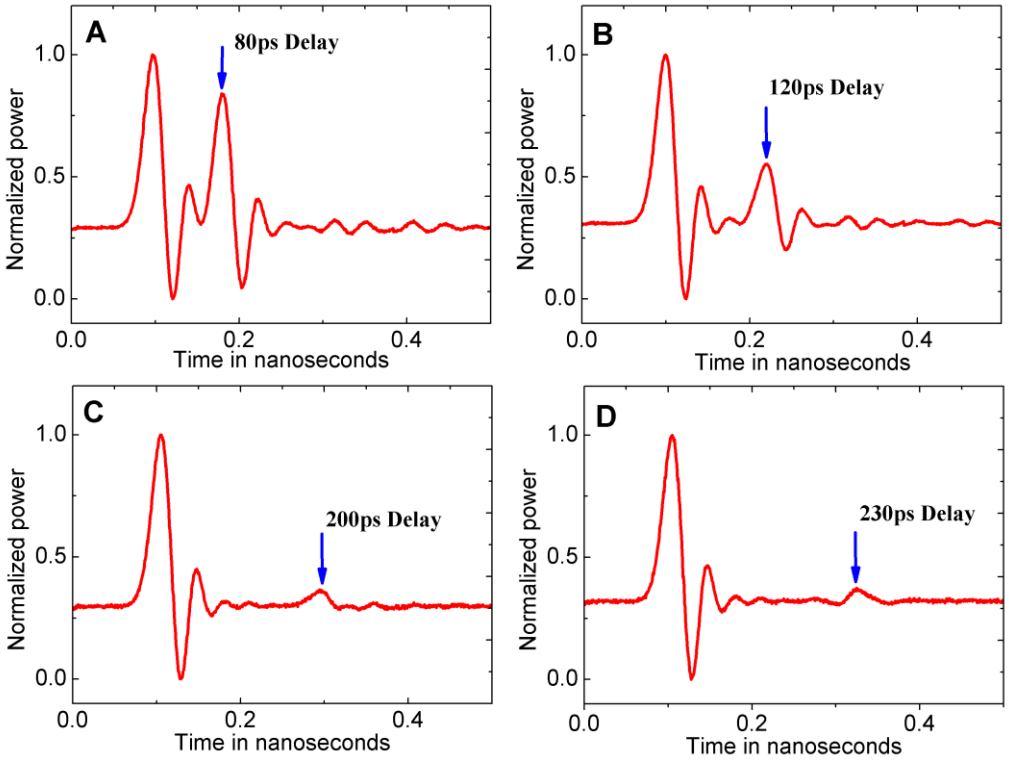

Fig. 4.7 Different delays are measured through changing the time between the store and the release top pumping pulses.

This large delay, as compared to previous dynamically tuned structures [28,85], is inherently due to the absence of free-carriers in the storage unit of our system. We expect that using an identical system a delay of several nanoseconds is possible provided the inherent waveguide/cavity loss is low enough. Here our waveguide loss was measured to be an exceedingly high 8dB/cm due to fabrication issues which introduced considerable sidewall roughness. This loss could be reduced to less than 3dB/cm with

similar waveguide dimensions and could be further reduced by using etchless waveguides (loss of <0.5 dB/cm) [92].

The initial larger peak seen at t~100ps is due to power that leaks out from the system before the storage process takes place. As discussed earlier the initial alignment of the input ring with the EIT mode slightly disrupts the overall phase of the EIT mode, allowing some light to escape the storage unit [28] This peak was not visible in Fig. 4.2A because the output ring (which is absent in the experiment) does not transmit this initial peak. In the experiment there is also an additional power leakage from the imperfect closing of the EIT resonance using heat as seen and discussed in Fig. 4.5C along with the low extinction ratios of the resonators. This initial peak can be minimized by utilizing a storage unit with multiple cavities and by tuning the coupling coefficients [89,90] .

In order to compare the quality of the storing process against previously demonstrated systems the output power at different delays was measured as shown in Fig.4.8. The system shows the expected exponential relation between output power and storage time. The characteristic decay time of the system is measured to be 160ps which is four times larger than previous systems [10, 11]. In addition, data is stored for more than 32-times the pulse duration as opposed to a fraction of the input pulse duration as demonstrated in a passive delay element [93]. This delay is achieved with a maximum efficiency of 24% (relative to the input pulse), which significantly breaks the time-bandwidth limit of a single cavity. We would expect that a ~5picosecond pulse that is coupled to a cavity with a photon lifetime of ~160 picoseconds would have an efficiency of at a maximum of 3%. However, here we show more than 9% of the initial pulse is stored after 160 picoseconds in the unit which is significantly larger than the time-bandwidth limit of a passive single

cavity. And without the leakage of the light to the other ports of the storage unit during the storage/release process we would expect the efficiency could be further increased. We should note that in order to achieve 100% efficiency multiple cavities would need to be used in order to completely store the input pulse as proposed elsewhere [89,90,94].

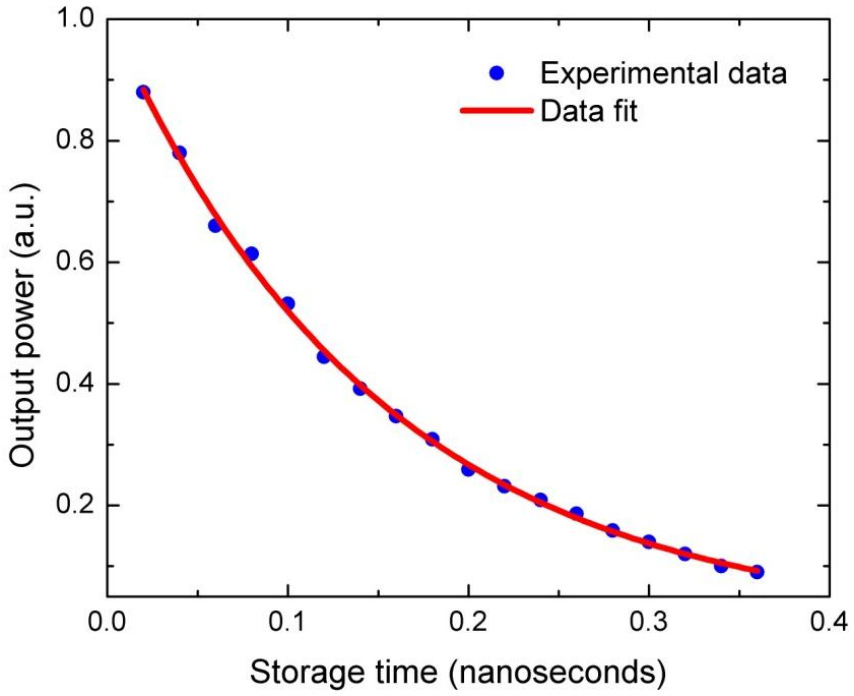

Fig.4.8 Different delay measurements and data fit, the system has an intrinsic decay time of ~160ps.

4.5 Quantum mechanical Analysis

4.5.1 Theoretical Model

After experimentally showing that the process is successful using high intensity light, we apply our dynamical analysis developed in Chapter to study the coherent trapping of a single photon wave packet in a multi-waveguide multi-ring system. Similar classical light experiments have been performed which rely on a photonic EIT analogue [28,55,56,85,95]. Due to the importance of the quality of the storage unit we consider the

structure in [55] where the interaction between the photon and the dynamic parts of the system is minimal. This opens the door for efficient single photon processing unit based on silicon electronic devices, enabling the integration of hybrid structures capable of a wider range of functions. A schematic of the device is shown in Fig.4.9.

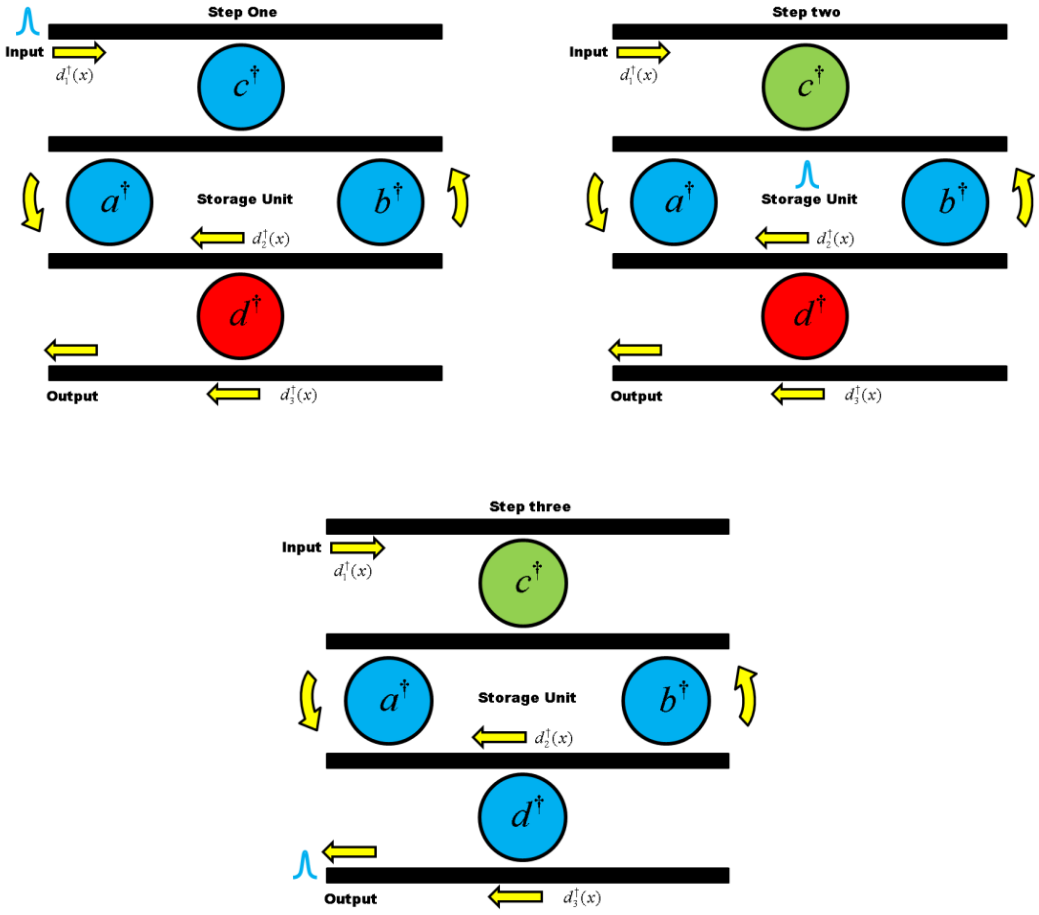

Fig.4.9 Schematic the single photon storage unit, (Step 1) shows the acceptance state of the system. Bits are stored as shown in (Steps 2) then released in (Steps 3).

Equations (4.7)-(4.14) below are the time evolution equations for the system. Note that that we are considering microcavities with no internal coupling between clockwise and counter-clockwise modes so that there will be a uni-directional excitation of waveguide

modes. This implies in Fig. 4.9 that modes d_1,d_2, d_3 ,and , d_4 propagate in the left, right, left, and right directions, respectively. Furthermore, the initial state of the system (input state position and direction) determine the permitted coupling conditions.

$$\left(\omega_0 - iv_g \frac{\partial}{\partial x_1} - i\frac{\partial}{\partial t}\right)\tilde{\phi}_{d1}(x,t) + \delta(x_c)V\tilde{e}_c(t) = 0 \tag{4.7}$$

$$\left(\omega_0 - iv_g \frac{\partial}{\partial x_2} - i\frac{\partial}{\partial t}\right)\tilde{\phi}_{d2}(x,t) + \delta(x_a)V\tilde{e}_a(t) + \delta(x_b)V\tilde{e}_b(t) + \delta(x_c)V\tilde{e}_c(t) = 0 \tag{4.8}$$

$$\left(\omega_0 - iv_g \frac{\partial}{\partial x_3} - i\frac{\partial}{\partial t}\right)\tilde{\phi}_{d3}(x,t) + \delta(x_a)V\tilde{e}_a(t) + \delta(x_b)V\tilde{e}_b(t) = 0 \tag{4.9}$$

$$\left(\omega_0 - iv_g \frac{\partial}{\partial x_4} - i\frac{\partial}{\partial t}\right)\tilde{\phi}_{d4}(x,t) + \delta(x_d)V\tilde{e}_d(t) = 0 \tag{4.10}$$

$$\left(\omega_{\mathrm{c,a}} - i\frac{1}{\tau_{\mathrm{c,a}}} - i\frac{\partial}{\partial t}\right)\tilde{e}_{\mathrm{a}}(t) + V^*\tilde{\phi}_{d2}(x_a,t) + V^*\tilde{\phi}_{d3}(x_a,t) = 0 \tag{4.11}$$

$$\left(\omega_{\mathrm{c,b}} - i\frac{1}{\tau_{\mathrm{c,b}}} - i\frac{\partial}{\partial t}\right)\tilde{e}_{\mathrm{b}}(t) + V^*\tilde{\phi}_{d2}(x_b,t) + V^*\tilde{\phi}_{d3}(x_b,t) = 0 \tag{4.12}$$

$$\left(\omega_{\mathrm{c,c}}(t) - i\frac{1}{\tau_{\mathrm{c,c}}} - i\frac{\partial}{\partial t}\right)\tilde{e}_{\mathrm{c}}(t) + V^*\tilde{\phi}_{d2}(x_c,t) + V^*\tilde{\phi}_{d3}(x_c,t) = 0 \tag{4.13}$$

$$\left(\omega_{\mathrm{c,d}} - i\frac{1}{\tau_{\mathrm{c,d}}} - i\frac{\partial}{\partial t}\right)\tilde{e}_{\mathrm{d}}(t) + V^*\tilde{\phi}_{d4}(x_d,t) + V^*\tilde{\phi}_{d3}(x_d,t) = 0 \tag{4.14}$$

The system operates as follows; initially the input cavity is tuned to the storage unit cavities to direct the single photon wave packet into the system. Next the eigenstate of the input cavity is changed to trap the photon in the storage unit. In order to release the photon from the system we tune the eigenstate of the output cavity to the storage unit.

4.5.2 Simulation Results

The system of equations were solved numerically with a single photon Gaussian packet as our input state propagating from left to right in waveguide mode d_1. First the packet is coupled to the storage unit then the storage unit is closed by detuning the input cavity and we see that we can hold the wave packet. At later times the input cavity is tuned back to the storage unit and the packet leaks back to the output port as shown in Fig. 4.10. In this way we have demonstrated the coherent storage and release of a single photon via linear optical interactions in a network microcavity system.

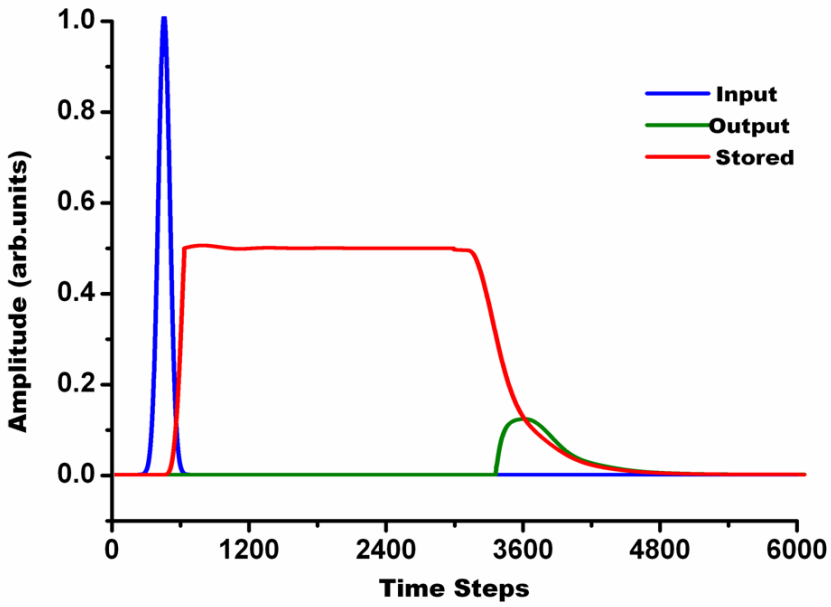

Fig.4.10 Storage and release process of single photon wave packet. The input Gaussian pulse is shown at time step=600. The stored packet amplitude extends from time steps=600-3600. The released wave packet decays from the storage unit at time step=3600

4.6 Summary

We proposed, analyzed, and experimentally tested a novel design for an active delay element which has numerous applications ranging from optical signal processing to quantum computing. The dynamic nature of the system breaks the time bandwidth limitations imposed by static cavities, resulting in a storage time of approximately 300ps.The storage time is only limited by the quality of the cavities used and could be significantly increased to several nanoseconds by using low loss cavities and by optimizing the fabrication process [57,84-86,93]. One tradeoff of our approach is it does require more power to realize the system (in order to ensure complete isolation of the capture switch from the storage unit). However, this is an acceptable tradeoff in order to achieve the large delays shown here. Finally we have presented a full quantum mechanical model and showed single photon trapping in a system of cavities.

CHAPTER FIVE

ENNINEERED TRANSITIONS IN PHOTONIC MOLECULES

5.1 Introduction

The engineering and active control of resonant photonic structures has enabled unique optical functionalities. In one recent work researchers showed that the direction of propagation and mode profile can be linked through photonic transitions – enabling a non-magnetic optical isolator [34] , others broke the time-bandwidth limit in optical cavities by dynamically tuning the bandwidth of coupled cavities [28,55], and others have realized 100% efficient linear wavelength conversion by trapping light while adiabatically tuning the eigenstate of a resonator – commonly known as adiabatic wavelength conversion [30-32,76,94,96,97]. However, these functionalities have been limited by the mechanism used to realize the refractive index change. For example, the Silicon photonics platform is limited to the free-carrier plasma dispersion effect (PDE), which is used to reduce refractive index through carrier injection [18,22,35]. However, carrier injection always results in a resonant wavelength shift towards the blue – limiting adiabatic wavelength conversion to blue wavelength changes [98]. In contrast, here we show that it is possible to efficiently change the wavelength of light, to the red or to the blue, regardless of the refractive index sign by engineering the states of a system of resonators.

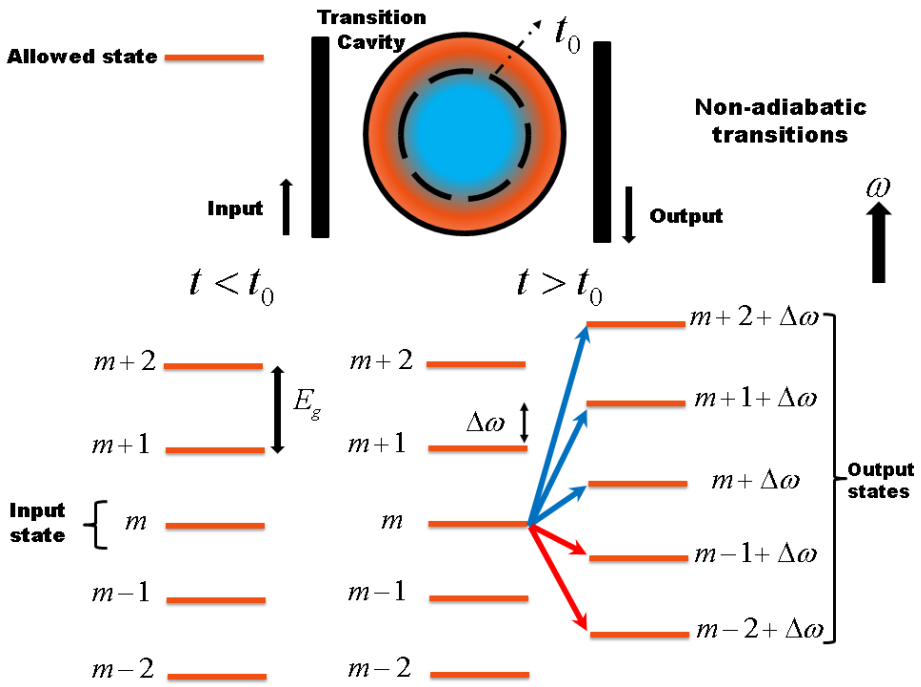

Fig.5.1 Photonic transitions in atom-like photonic structure. Light initially excites one state of the resonator (t<t0). When the resonator is switched at a fast rate, multiple output states are excited (t>t0). Δω is the relative shift of all of the states due to the refractive index change.

It was shown in [76] that when a resonator is *non-adiabatically* perturbed it is possible to transition photons to other resonant modes – even towards the red, albeit with an extremely low efficiency. The reason for this low efficiency is that the final state of the system couples to a continuum of output modes - with a dominant excitation of the adiabatic shift as seen in Fig.5.1. [32]. Here we show that by carefully designing the states of a *system* of cavities, which we call a photonic-molecule, nearly all of the light can be non-adiabatically transitioned to just one state – even towards the red. This opens the possibility of using the PDE for both blue and red shifts of light.

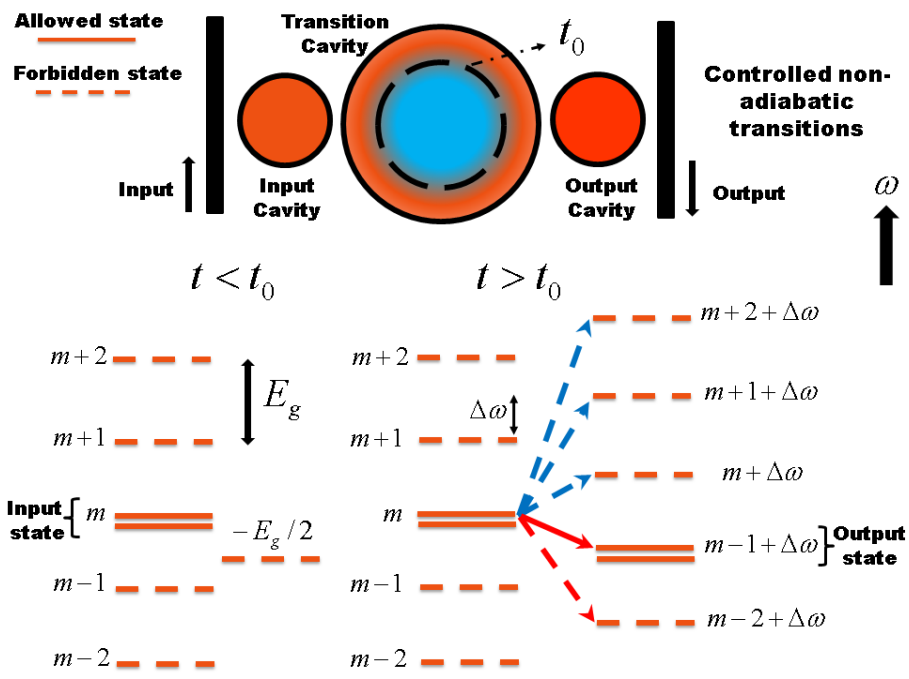

Fig.5.2 Photonic transitions in molecule-like photonic structure. Photonic transitions are engineered using the resonance of the input and output cavities. Only one state is allowed after switching the transition cavity. The remaining transitions lie inside forbidden states in the energy diagram.

5.2 Designing system states

The proposed photonic molecule is shown in Fig.5.2. It consists of an input and output cavity each with large Free Spectral Range (FSR) and a transition cavity having closely spaced states. By initially aligning one resonance of the input cavity and one resonance of the transition cavity it is ensured that the system only has one allowed state, as shown as a double solid line in the figure (the double lines indicate that there is mode splitting at this allowed state) [99]. We note that although there are many internal degrees of freedom for the transition cavity, they are not allowed due to the phase matching condition enforced by the input cavity. On the other hand, the output cavity has a red

shifted resonance from the input state (lower energy in Fig.5.2 [-Eg/2]). Consequently, light cannot escape from the input state into the output cavity due to the misalignment of the states.

In order to transition the light efficiently to the red-shifted output cavity we induce a non-adiabatic perturbation of the transition cavity through a refractive index reduction. This will blue-shift all of the states of the transition cavity, including the initially excited input state. However, now the input cavity will be in a forbidden state and the output cavity will be on-resonance with the (m-1) mode of the transition cavity – forming a newly allowed state. It is important to note that this is the only allowed output state of the system due to phase matching between the cavities. Consequently, the light is red-shifted.

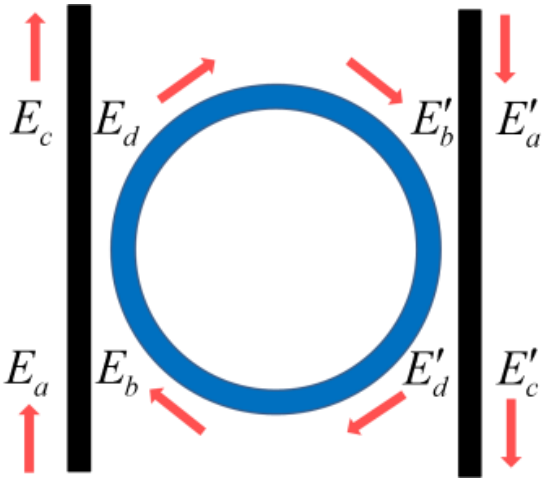

Fig.5.3 The building block of the photonic molecule consists of a single cavity. The fields are related through coupling coefficients and time evoltuion operators equations 1-3. Radiation and scattering losses are lumped in the field absorption cofficient γ.

In order to demonstrate this we describe our model which uses temporal matrix analysis [99] including all the evolution operators and coupling coefficients. The following equations govern the different relations between fields inside an individual resonator, as shown in Fig.5.3.

$$\begin{bmatrix} E_C(t_m) \\ E_D(t_m) \end{bmatrix} = \begin{bmatrix} t & i\kappa \\ i\kappa & t \end{bmatrix} \begin{bmatrix} E_A(t_m) \\ E_B(t_m) \end{bmatrix} \quad 5.1$$

$$E_B(t_m) = E'_D(t_m - 1)Ue^{(-i\omega t_m)} \quad 5.2$$

$$E'_B(t_m) = E_D(t_m - 1)Ue^{(-i\omega t_m)} \quad 5.3$$

Here γ and $\Phi(t,\lambda)$ are the loss coefficient and phase accumulated after one round trip around the ring. The time evolution operator U links the field after half round trip propagation inside the resonator $U = \exp(-\gamma/2 - i\phi(t,\lambda)/2)$. E_x represents the different fields in the system. The coupling and transmission coefficients satisfy the power preserving relation $|t|^2 + |\kappa|^2 = 1$.

The initial steady state response of each ring isolated from the rest of the system is shown in Fig.5.4. In the model we consider realistic parameters – a typical value of waveguide loss of 3dB/cm is assumed, the input and output ring resonators have a radius of approximately $R_{input/output}$=10μm and the transition resonator has a radius of $R_{transition}$=100μm (FSRs of 8.8nm and 0.437nm, respectively). Note that, for clarity the individual ring resonances were calculated separately to visualize the position of different resonances with respect to each other, while in the actual system they will be coupled. We see in Fig. 4 that initially the input cavity and the transition cavity have the same resonance. The output cavity is placed at the midpoint of the gap between the (m) and

(m-1) mode of the transition cavity. This will ensure that when the transition cavity is blue-shifted using the PDE that it will be in-resonance with the output cavity. This will effectively create a phase-matched state with lower energy.

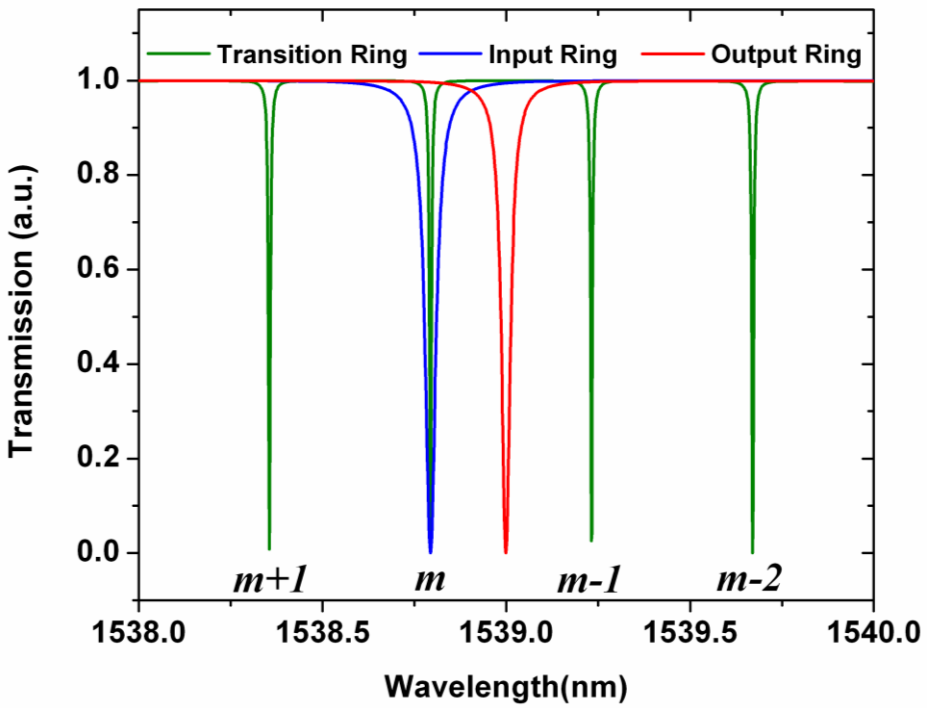

Fig.5.4. Transmission of different rings in the intial state of the system. The input cavity and the transition cavity have the same resosnance condition, while the output cavity is purposly shifted toward red wavelengths half FSR away.

5.3 Red transitions with blue index change

The controlled transition towards lower energies (red) is demonstrated in Fig. 5 by injecting a carrier density of 4E16/cm^3 (Δn=-1.9E-4) in the transition resonator while a pulse of light is trapped inside. The switching is performed over 100fs, a time much smaller than the photon life time in order to ensure non-adiabatic transitions in the transition ring [76]. In Fig.5.5 we see that most of the light is red shifted by $\Delta\lambda$=+0.16nm

and there is minimal excitation of the other states. Consequently, by engineering the states of the system it is possible to induce any state transition. We note that the new state is positioned slightly away from the center of the bandgap of the transition ring due to mode splitting. However, by changing the coupling between the resonators and positions of the resonances, different states can be created. An important point to be emphasized here is the fact that this is a true mode coupling in the transition ring, not a filtering effect - the spectrum shown in Fig.5.5 is measured inside of the transition ring not at the output port. Furthermore, this shows that only one red shifted mode is created in the transition ring due to the nature of the system.

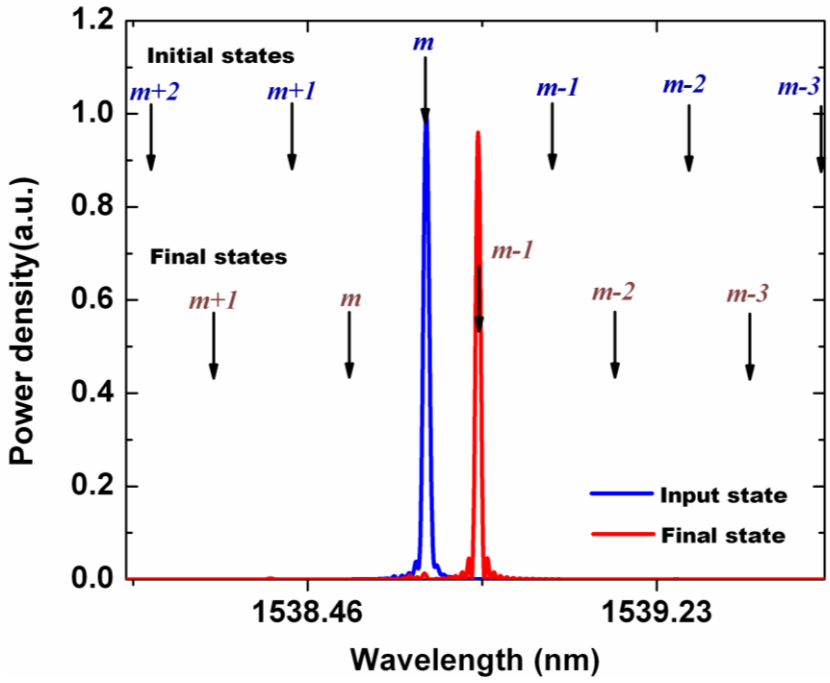

Fig.5.5 States before the switching (blue) and after switching (red) inside the transition ring. The conversion efficiency is 96%.

To verify the above theory, we numerically simulated the dynamic process by solving Maxwell's equations using the finite difference time-domain (FDTD) method [100]. The system has the same configuration as the one described earlier but with scaling differences in order to speed up

the computation process (Radii of Rtransition=24μm and Rinput/output=4μm. These correspond to FSRs of ~4nm and ~26nm, respectively).

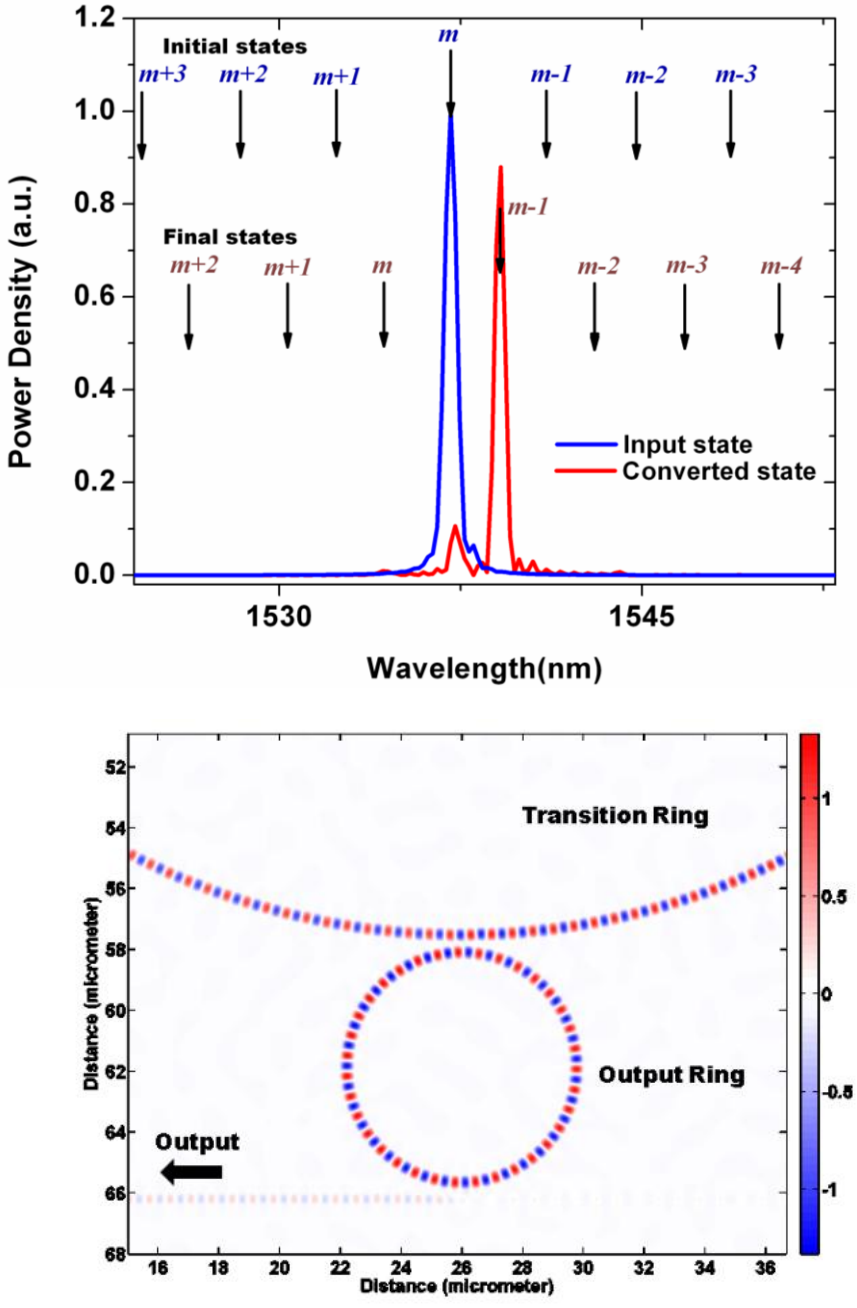

Fig.6. (a) FDTD result of red wavelengths created in the transition ring. (b) Field distribution in the system after the conversion. The converted light is now coupled to the output port through the output ring, which is initially red shifted.

We see in Fig. 5.6(a) that with an index shift of Δn= -2E-03 the light is red-shifted by 2nm. The behavior is qualitatively the same as the results obtained with temporal matrix analysis. However, the conversion efficiency is slightly lower (88%) since the non-adiabatic transition is not as efficient with the large FSR used in the FDTD simulation. This is not a fundamental limitation provided the FSR of the transition ring is small enough. In Fig.5.6b we can see that light is coupled into the output port which was initially detuned from it.

In order to maximize the conversion towards the red it is important to place the output rings state at a half an FSR away from the input state (m). Moving this resonance closer to the input state results in unintended adiabatic coupling to original (m) state. In addition, it would require a larger index change to achieve red-shifting since the initial (m-1) mode would be even farther away from the output state. On the other hand, placing the output ring state closer to the initial (m-1) state will also reduce the efficiency because the input and output state are initially further apart, but the refractive index change would be smaller – resulting in a weaker non-adiabatic transition. This could be overcome, however, by using resonant transitions where the resonator is switched at a rate corresponding to the difference the state [96] spacing. In addition, without resonant transitions it is important to switch the transition resonator as quickly as possible in order to maximize the non-adiabatic transition process, as seen in Fig. 5.7

5.4 Summary

In conclusion, we demonstrated that by engineering the states of a photonic molecule, and using non-adiabatic transitions, it is possible to obtain wavelength changes that are independent of the refractive index change mechanism. This new phenomena can lead to more flexibility in designing integrated optical systems.

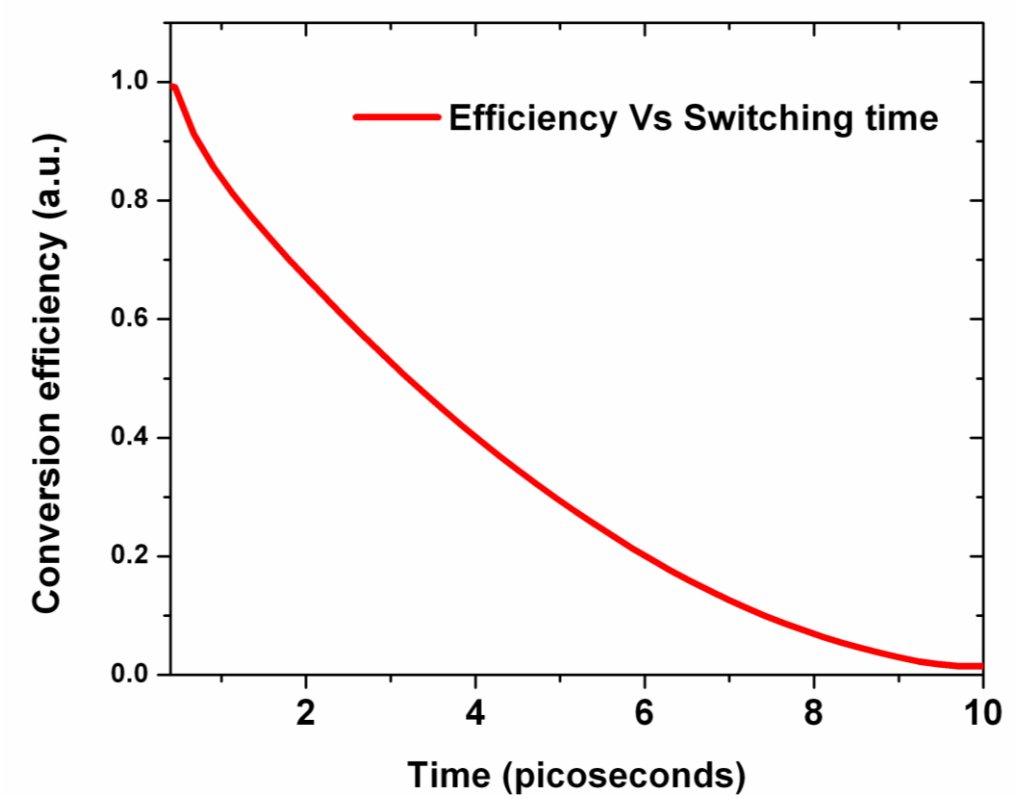

Fig.5.7 Red wavelength conversion efficiency vs. switching time. The efficiency decreases as switching speed is slowed due to the enhancement of the adiabatic shift in the resonator.

CHAPTER SIX

NON-MAGNETIC CMOS COMPATIBLE PHOTON ISOLATOR

6.1 Introduction

Optical Isolators play a vital role in optical integrated circuits by only allowing transmission of data in one direction. In optical fiber and bulk optical systems isolators are realized using a system of polarizers and Faraday Rotators. However, Faraday Rotation inherently requires a DC magnetic field and a gyrotopic material, such as, Bismuth Iron Garnet (BIG) or Yttrium Iron Garnet (YIG). These materials are simply incompatible with low-cost CMOS fabrication processes and have been difficult to miniaturize and integrate on a silicon nanophotonic chip, which is now the leading platform for next generation photonic circuits and interconnects [101].

Fundamentally optical isolation is made possible by realizing a non-reciprocal system. Making a system that behaves depending on the direction of propagation of the light through it. A very novel method was presented that realizes such a system by inducing interband transitions between the fundamental and higher-order modes of a multimode optical waveguide [34]. The transition only occurs when the light is phase matched which is realized by modulating small parts of the waveguide through a temporal and spatial periodic refractive index modulation at 10's of GHz speeds. However, there will be considerable challenges in realizing this in practice. In addition, due to the limited refractive index change that is possible in silicon the required length of the device is on the order of millimeters. While it is possible to reduce the size of the device using a ring

resonator it will be difficult to avoid unintentional excitation of the higher-order modes of a multimode ring resonator similar to what occurs in disk resonators [31].

In contrast here we present a simple isolator that is based on an adiabatic wavelength conversion effect that was recently demonstrated in silicon microcavities [30-33,102] . Isolation is achieved by dynamically tuning the refractive index of a resonant cavity. There are no requirements on what resonant mode is used, how quickly it is tuned, or how the modes are spaced. In addition, the entire resonator can be tuned to achieve isolation as opposed to precisely engineered portions thus greatly reducing the device design constraints. One tradeoff with our approach is it inherently only works with pulses but since high-bit-rate data signals are essentially pulsed this is not a significant limitation.

A schematic of the proposed isolator is shown in Fig.6.1. The device works by inputting a “red” wavelength signal travelling from left-to-right into a wavelength converter. This converts the input signal to a “blue” wavelength and then lets it travel to the rest of the photonic circuit. If any of the “blue” light is reflected, it will travel past the wavelength conversion unit and will be caught by a “blue” filter. This will effectively keep it from travelling back to the input of the photonic circuit, in turn, realizing complete optical isolation. Wavelength conversion is achieved by using a micro-resonator that traps light for a brief time in a “red” resonant mode. While the light is trapped the refractive index of the entire resonator is adiabatically tuned. This shifts the lights wavelength to a new “blue” wavelength via the adiabatic wavelength conversion process explained in the following section and elsewhere [30,32]. The adiabatic process theoretically has 100% conversion efficiency [30] provided that the light is completely trapped in the resonator.

However, due to the dynamic nature of the pulse-resonator interaction it is difficult to realize 100% conversion with a single resonator. Therefore, here we propose a novel scheme using several resonators to achieve complete conversion.

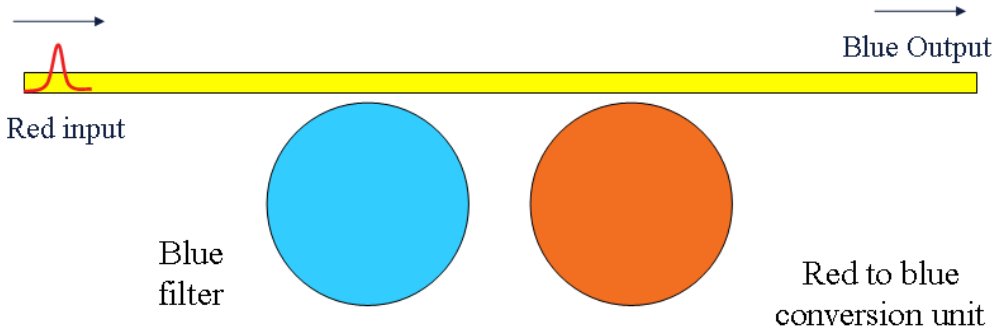

Fig.6. Schematic of the isolator. A red input signal is converted to a blue output signal by a adiabatic wavelength conversion unit (Red to Blue). If any of the blue signal is reflected it is filtered out so that it cannot propagate back to the input of the circuit.

6.2 Adiabatic wavelength conversion (AWC)

We initially study the adiabatic wavelength conversion process before going into details of the isolator operation. We first consider the behavior of electromagnetic waves in a dynamic media [103]. The input signal can be expressed as an infinite sum of uniform plane waves each having a unique direction, a unique frequency of oscillation, and a time varying envelope.

$$E(t,z) = \sum_{k} f_k(t).e^{i(\omega t - k_k z)} \qquad 6.1$$

Each term of the sum satisfies Maxwell's equations at this particular frequency and wave vector. To see the effect of a dynamically tuned system we consider a time-varying permittivity in the wave equation:

$$\nabla^2 E - \varepsilon(t)\mu_0 \frac{\partial^2 E}{\partial t^2} = 0 \qquad 6.2$$

We substitute the expression of the field in (6.2) at specific *k* vector value then apply the slow varying envelop approximation. We can easily get a general differential equation describing the propagating wave in the system at any instant of time.

$$i\frac{\partial f(t)}{\partial t} = \frac{\varepsilon(t)\omega_0}{2(\varepsilon(t)+\varepsilon)} f(t) \approx \frac{\varepsilon(t)\omega_0}{2\varepsilon} f(t) \qquad 6.3$$

ε and ω_0 are the static dielectric constant of the medium and the center frequency of the signal propagating through the systems. The dynamic tuning in the dielectric constant is generally less than one percent of the static value which can be neglected in the sum as shown above.

The last step in obtaining an expression of the wave going through the system is to solve (6.3). This is done by integrating it with respect to time using an initial value of the signal $f(t_0)$ at time t_0 when the dynamic tuning starts.

$$f(t) = f(t_0)\exp\left(-i\omega_0 \int_{t_0}^{t} \frac{\varepsilon(\tau)\omega_0}{2\varepsilon} d\tau\right) \qquad 6.4$$

By examining the expression above we can clearly see that the frequency of the signal is a function of the dynamic tuning of the system. The frequency is found by taking the derivative of the signal's phase with time.

$$\omega(t) = \omega_0\left(1 - \frac{\varepsilon(t)}{2\varepsilon_0}\right) \qquad 6.5$$

This simple analytical approach shows that the frequency of light is changed by simply modulating the materials permittivity with time. Inherently this assumes that the entire signal senses the permittivity change. While this could be done in a waveguide in

practice the light needs to be trapped/confined in a particular area to achieve a spatially-independent process [30,32]. It is also seen from (6.5) that the conversion efficiency of the process is 100%, meaning that all the photons that experienced the index change in the system get converted to the new wavelength. However, it is actually impossible to have all of the photons in a pulse experience the dynamic tuning which limits the conversion efficiency to about 35% when cavities are used for trapping light [32].

In order to explain the low conversion efficiency of single resonator we initially consider a simple system [32] shown in Fig. 6.2. It simply consists of two waveguides and an optical cavity. When the input signal matches the resonance of the cavity (both red) it gets coupled to the cavity for one photon life time. If the cavity is dynamically tuned the trapped wave will change its wavelength following the resonance shift of the cavity (both cavity and signal shift to blue). However, this simplistic picture does not take into count the time-bandwidth product of both the input pulse and the cavity. To understand how this is important to the total conversion efficiency consider a time-bandwidth limited optical signal *x(t)*, with a Fourier transform *X(w)*. This signal has constant time-bandwidth product that comes directly from the definition of the transform of the signal (i.e. $\Delta t.\Delta\omega = C$). Similarly the cavity has a time-bandwidth limited response which is also important to consider.

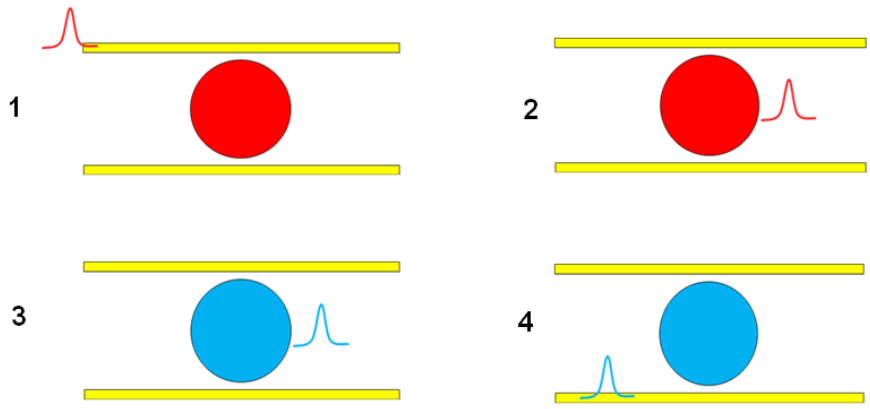

Fig. 6.2 Ideal wavelength conversion system.

We assume for the moment that the bandwidth of the cavity is larger than the bandwidth of the input signal (i.e. very long input pulse). In terms of bandwidth argument the pulse will fit perfectly inside the cavity allowing for efficient trapping and high conversion efficiency. But due to the time-bandwidth limit only a small fraction of the pulse in time gets trapped inside the cavity at a particular instant. This is due to the small photon lifetime of time of the cavity (large bandwidth). At this instant if the cavity is tuned only the portion of the signal that is inside gets converted. The rest of the signal in the input waveguide senses a different cavity resonance which stops it from coupling. This is shown in Fig 6.3a. On the other hand if the pulse is short then most of the signal bandwidth is not supported by the narrow bandwidth of the cavity. This results again in a low efficiency, because only the frequencies that couple to the cavity get converted. This is shown in Fig 6.3b.

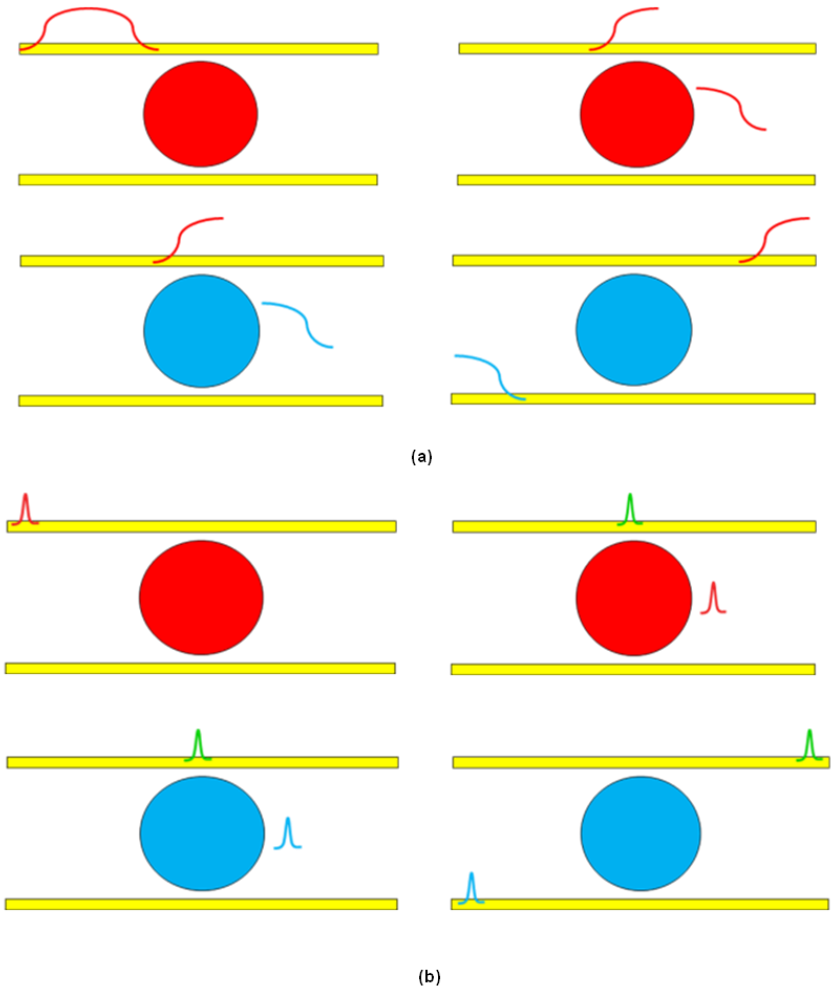

Fig. 6.3 Long pulse (a), and a short pulse (b) coupled to a cavity while dynamically tuning the resonance of the cavity.

In dealing with high data rate signals even if the cavity and signal parameters are closely matched some of the pulse escapes before the cavity is dynamically tuned. While some cannot couple to the cavity after it has been tuned due to the change in resonance. Consequently, the net conversion efficiency is on the order of 30-40% when the pulse and cavity are closely matched [32].

In conclusion a system of a single resonator cannot achieve 100% conversion efficiency. In the following sections we will present two novel techniques in time and frequency

domains for 100% conversion efficiency. These represent the heart of the isolator proposed in the following sections.

6.2.1 Frequency domain sampling (FDS) technique

One way of breaking the 35% efficiency barrier is using frequency domain sampling technique by dividing the input bandwidth into smaller segments as shown in Fig.6.4 and delaying each part of the bandwidth with a constant delay. Then reconstructing the signal again after the conversion takes place. Consider an input signal $x(t)$ with a Fourier transform (FT) $X(\omega)$. This FT can be expressed as a sum of weighted segments of width $\Delta\omega$ which is identical to the original transform in the limit when the number of segments goes to infinity.

$$X(\omega) = \sum_m A_m \delta(\omega - \omega_m) \qquad 6.6$$

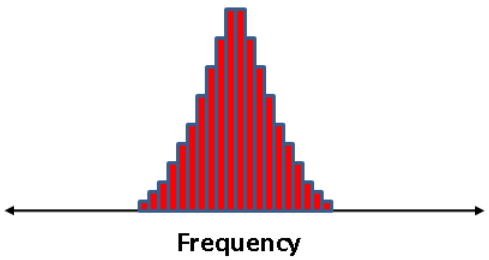

Fig. 6.4 frequency sampling of the input spectrum.

The procedure described above can be realized using cascaded high Q optical cavities to sample the frequency response of the signal as shown in Fig.6.5. Each cavity can be approximated by a delay element at the resonance frequency when the Q is high. The frequency domain representation of a cavity in high Q condition is approximated in (6.7),

which is centered the resonance frequency of the nth cavity mode ω_n. The difference between the resonances of consecutive cavities must be larger than twice the bandwidth of the cavity so that the modes of different cavities will not overlap.

$$R(\omega_n) = e^{-i\omega_n t_0} \tag{6.7}$$

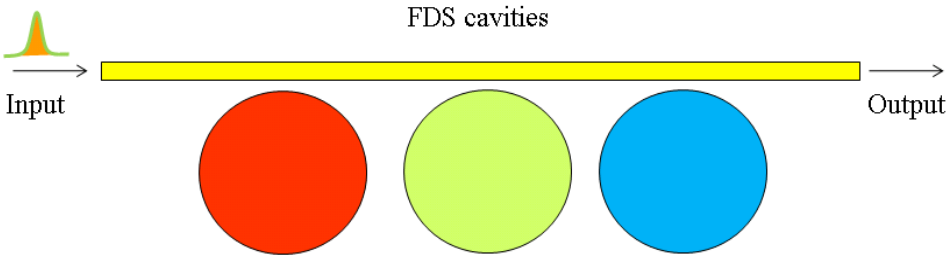

Fig. 6.5 Schematic of FDS system.

Due to the fact that the modes do not couple, each segment in the input spectrum will couple only to one cavity. As a result all frequencies will have the same delay given that the cavities are identical (produce the same delay). The output is given by the following sum which vanishes except for $m = n = k$

$$Y(\omega) = \sum_k A_k e^{-i\omega_k t_0} \delta(\omega - \omega_k) \tag{6.8}$$

Taking the IFT of the previous equations yields the expected result for the output which is simply a delayed version of the input.

$$y(t) = x(t - t_0) \tag{6.9}$$

Each resonator satisfies the time-bandwidth limit but the presented system allows us to increase the photon life time by using high Q cavities while still accept large frequency

content. The minimum number of the cavities needed equals the ratio between the bandwidth of the signal and the bandwidth of a single cavity.

6.2.2 Time domain sampling (TDS) technique

The addressed problem can be solved in a different fashion using time domain approach. This is done using multiple identical optical cavities with a bandwidth larger than the input bandwidth to ensure that all frequencies are coupled to individual cavities. Although the delay of an individual cavity is small because of their small photon life time but using an array of them any delay value can be obtained without any limit on the bandwidth. Again each cavity satisfies the time-bandwidth limitations but the whole system breaks it. Fig.6.6 shows a schematic of the system.

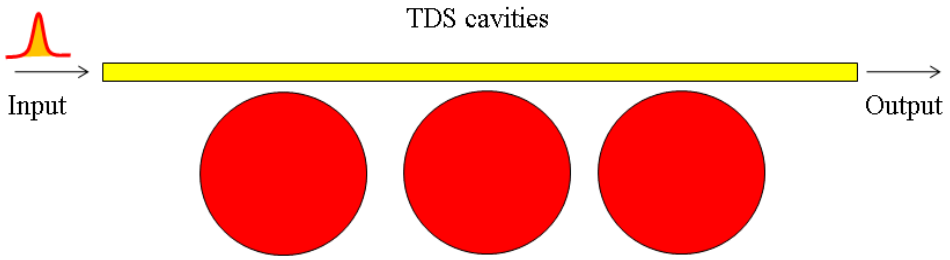

Fig. 6.6 Schematic of TDS system.

To prove this analytically we first consider the same band limited input signal $x(t)$ with a FT $X(\omega)$. Because the bandwidth of the pulse lies completely within the allowed frequency range of each cavity (very small Q), the output of a single cavity is represented in frequency domain as a simple delay given by (6.10).

$$Y(\omega) = X(\omega)e^{-i\omega t_k} \qquad 6.10$$

Where t_k is the time delay produced by k_{th} cavity. In the case of large number of cavities (n) the output is delayed by nt_k.

$$Y(\omega) = X(\omega)e^{-i\omega\sum_k t_k} = X(\omega)e^{-i\omega t_0} \quad 6.11$$

Finally taking the IFT we find that the output of the system is a delayed version of the input with a delay equal to the number of cavities multiplied by the photon life time of a single cavity.

$$y(t) = x(t - t_0) \quad 6.12$$

The process explained above allows us to trap a pulse of light completely inside a system of microcavities for 100% adiabatic wavelength conversion efficiency. The minimum number of cavities needed equals the ratio between the duration of the signal to the photon life time of a single cavity.

6.3 Uni-directional active isolator

In this section we will present a novel design for unidirectional isolator using TDS technique. The isolator is shown in Fig.6.7. It contains an input ring (blue) with a resonance wavelength $\lambda 2$. The middle part represents the TDS wavelength conversion unit. It consists of seven rings side coupled to a waveguide. The large number of rings is a consequence of the small photon life time (high radiation loss due to the small radius). All the rings have radius of 2μm. The dimensions of the silicon waveguides used are 460nmX250nm surrounded by silicon oxide.

The isolator works as follows: when an input signal centered at $\lambda 1$ ($\lambda 1 > \lambda 2$) is launched through the input port it passes by the input ring then enters the system of the cascaded rings. We will see that the pulse is distributed in time between the rings which allows for 100% conversion when index change is applied. The index change is chosen so that the converted signal is now centered at the resonance wavelength of the input ring $\lambda 2$.

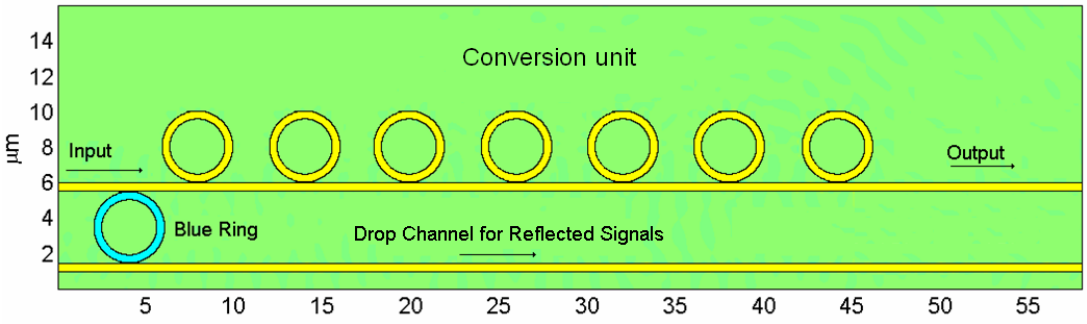

Fig. 6.7 Schematic of the isolator.

FDTD simulations were done to prove the analytical model and monitor light propagation through the systems in varies conditions. To examine the forward propagation characteristic of the system excitation is added. The input signal used is a TM polarized 3 picoseconds wide Gaussian pulse centered at wavelength 1554.9nm which matches the resonance wavelength of the rings used in the conversion unit. The simulated structure and pulse propagation are shown in Fig.6.8. As the pulse propagates through the system it passes by the input ring without any coupling to it (no light is coupled to the drop port of that ring in the bottom waveguide). Next the pulse is distributed in time between the conversion unit rings allowing for wavelength conversion. The conversion is done by changing the index of the rings. For practical cases the index is changed for a time less

than the photon life time of the cavities. With this novel TDS design large photon life times can be achieved by cascading cavities as explained. This opens the door for a mechanical index change of the system [54], using extremely force sensitive effective index structures [104]. After the conversion takes place the pulse is directed to the output port. This completes the forward propagation of the pulse through the system.

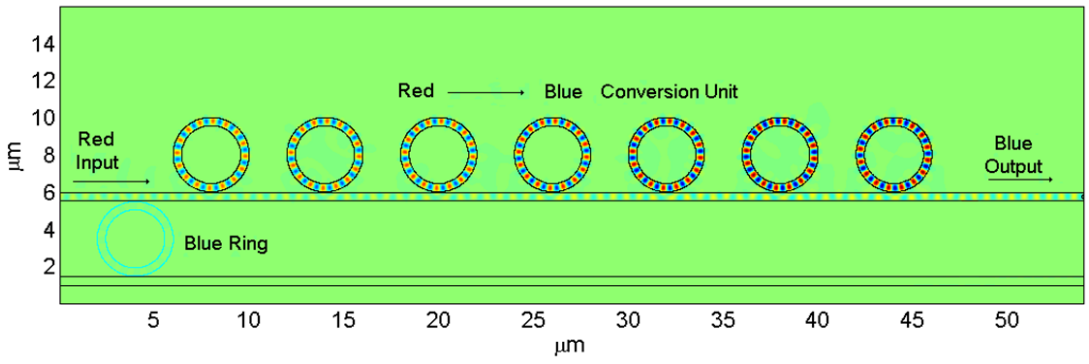

Fig. 6.8 Forward propagation simulation, where no power is coupled to the input ring.

The modulation strength $\delta n/n$ of the index change used is 1.4E-03 which is relatively large because of the low Q of the rings. After performing the time domain analysis the spectrum of the input signal and output signal is calculated using FT. The results are shown in Fig.6.9. The input signal is shown in red centered at a wavelength of 1554.9nm while the output signal after the conversion is shown in blue centered at wavelength 1552.7nm. The relative change in the index is proportional to the relative change in the index $\delta n/n = -\Delta\lambda/\lambda$.

The system shows 100% conversion efficiency indicating that all photons inside the cavities got converted to the new wavelength with no red signal in the output co-propagating with the converted blue. This also can be demonstrated using high Q cavities each centered at a different wavelength to span the input spectrum in FDS technique.

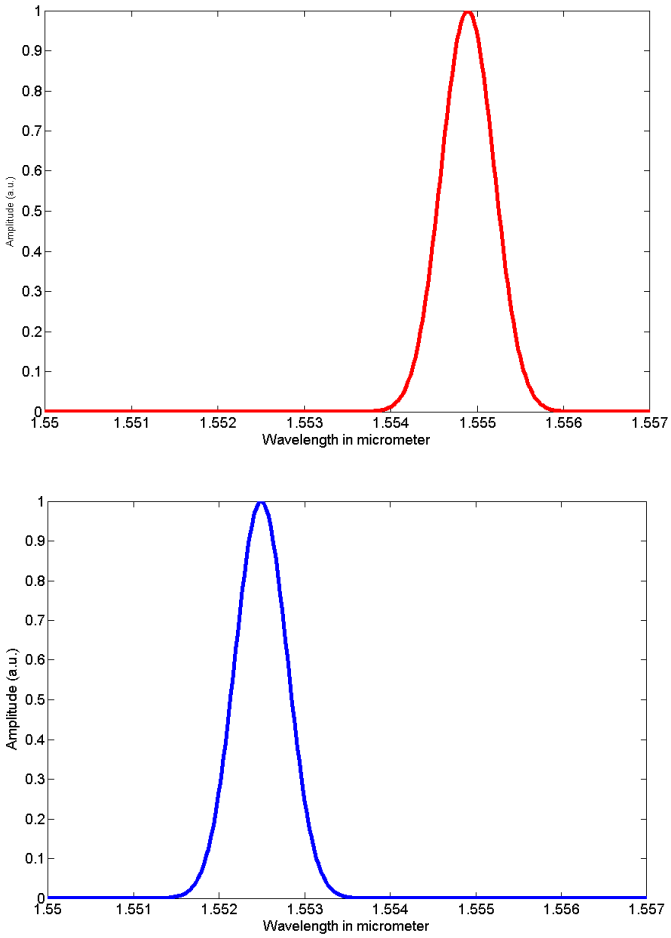

Fig. 6.9 Input signal (first), and the output signal (second).

After examining the forward characteristic of the isolator, we now move to the isolation characteristic in the case of waves propagating the opposite direction. The isolation is tested through using a high reflectivity broadband mirror placed at the output to redirect the converted waves back to the input port. Another test is performed using the same mirror when the conversion unit is not used while monitoring the coupling through the input port from the backward waves.

A schematic of the broadband mirror is shown in Fig.6.10. The mirror is simply a Bragg reflector that consists of eight low index holes in the center of the waveguide each hole

has a radius of 100nm [105]. The separation between the centers of two adjacent holes is 420nm. To find the reflectivity of the mirror with wavelength an ultra short 10fs pulse is launched then the FT is calculated to get the power reflection coefficient.

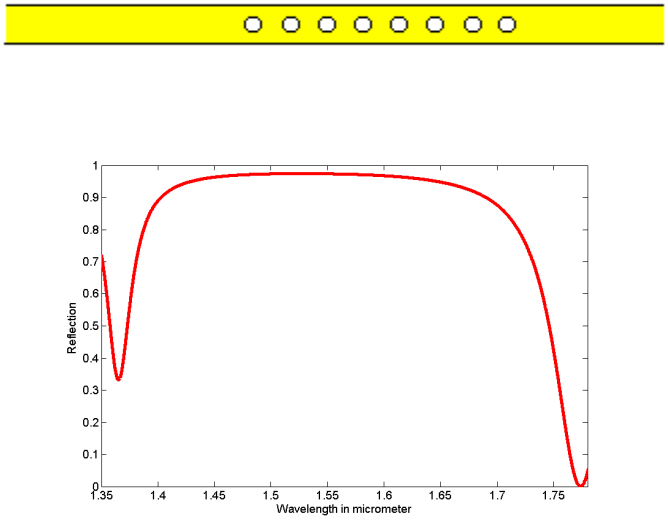

Fig. 6.10 Mirror reflectivity with wavelength.

From Fig.6.10 we can see that the mirror has high reflectivity in the operating wavelength from 1400nm to 1700nm. The next step is including the mirror in the system after the conversion unit to back reflect all the light to the input.

A pulse with the same parameters in the forward characteristics was launched through the system. The converted signal now gets reflected by the mirror placed in the end of the structure. When the signal reaches the blue input ring it gets coupled to it because the pulse now is centered at the resonance wavelength of that ring (1552.7nm) due to the conversion process that took place. This ring works as band stop filter for all the reflected waves after the conversion. It redirects light away from the input waveguide to the drop

port in the bottom waveguide. Looking at Fig.6.11 we can see that all the reflected waves after the conversion are completely isolated from the input.

With this approach 24dB isolation is achieved using non-magnetic materials in a compact and implementable fashion. Because of the flexible design of the system, the isolation ratio can be further increased by increasing the number of blue rings in the systems. The isolator relies on adiabatic wavelength conversion in single mode waveguides, which is desirable in integrated optical systems. It requires no complicated modulation techniques to modulate portions of rings or waveguides as in [34]. In addition, all the rings support the same spatial mode.

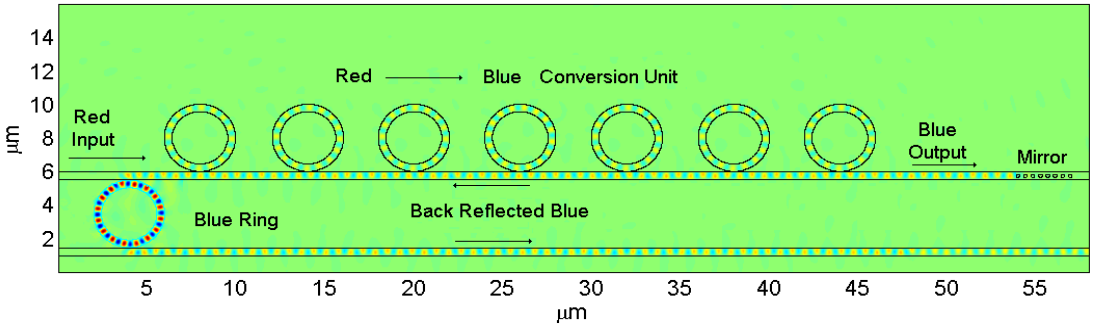

Fig. 6.11 Backward propagation.

For practical circuits all the rings can be efficiently tuned, using already implemented tuning systems [8]. The isolator works for a pulsed signal which is the desired operation in high data rate optical systems. The conversion unit timing can be synchronized using already implemented active optical delay elements [28,55,56,85,91]. Fig.6.12 shows the spectrum of the forward and backward propagating waves in the input ports with isolation of 24dB.

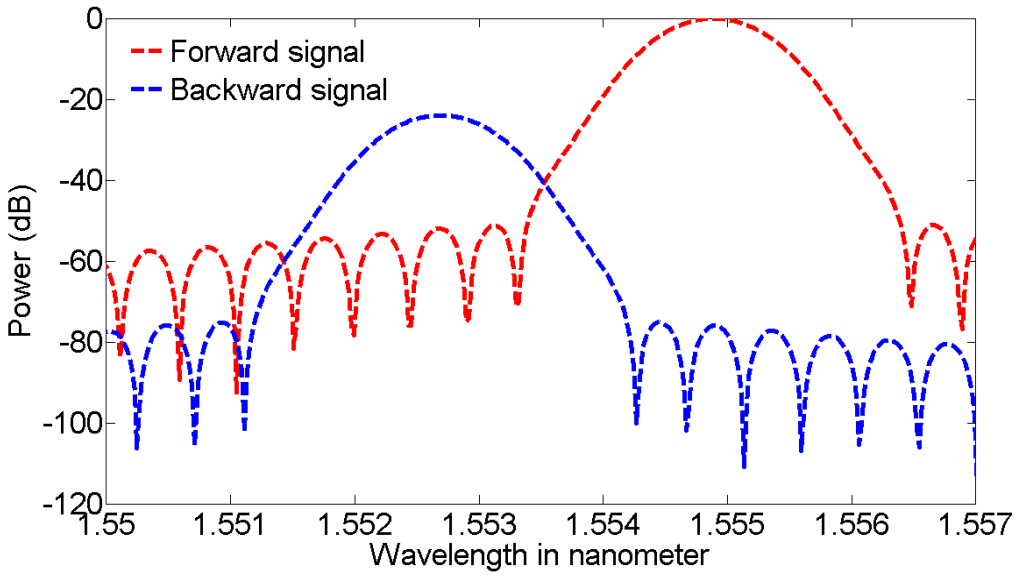

Fig. 6.12 Spectrum of forward and backward signals.

All the red input gets back reflected to the input port when the conversion unit is OFF as seen in Fig.6.13.

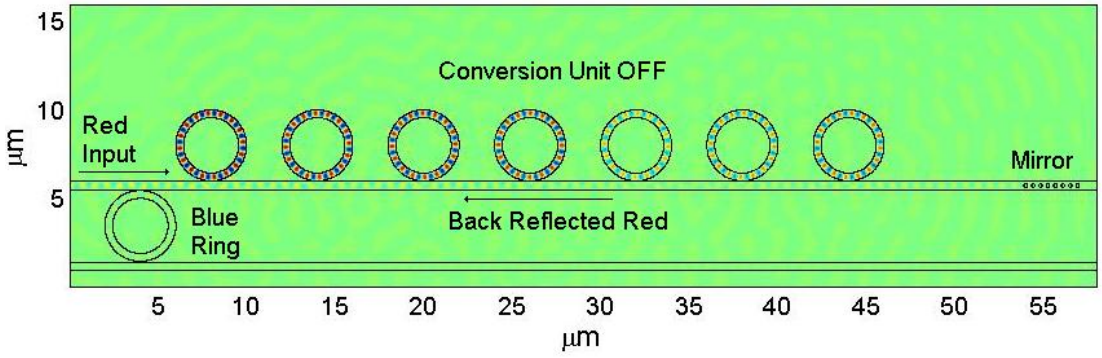

Fig. 6.13 Back reflected waves couple to the input when the conversion is not used.

6.4 Bi-directional Isolation

The increasing need for complex optical system with small foot print and less processing steps requires flexible multifunctional optical systems. Here we present a bidirectional optical isolation system which enables us to integrate two complete circuitries on both sides and get independent isolation for each direction. Although the system is reciprocal and can work equally as an isolator in both directions, it still exhibits non-reciprocal properties to isolate due to active tuning. An example of such system is shown in Fig.6.14.

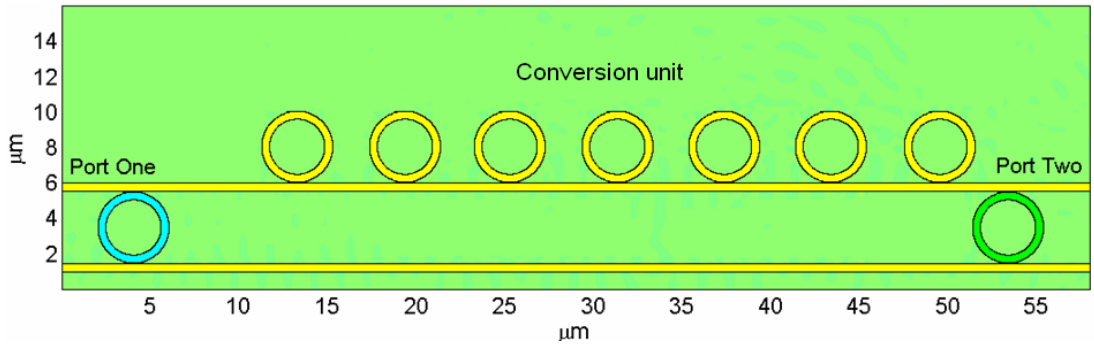

Fig. 6.14 Schematic of bidirectional isolation system.

It consists of two input rings as shown with wavelength conversion unit in the center. Relying on the fact that the WC processes produces a blue shift and the large bandwidth of the cavities in TDS systems, we can engineer the resonances of these rings with respect to the TDS unit. Let port one ring have a resonance wavelength $\lambda 3$ (blue Fig.6.15) while port two input ring $\lambda 2$ (green Fig.6.15). The position of these resonances on the spectrum of the converter is shown in Fig.6.15. Port one operates at the green part of the spectrum while port two at the red part of the spectrum.

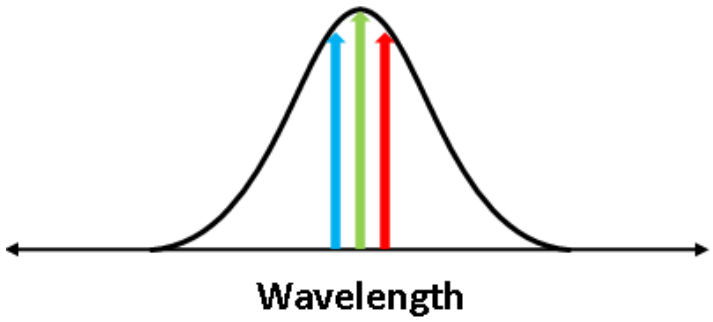

Fig. 6.15 The spectrum of the wavelength conversion unit with the different resonances $\lambda 1$, $\lambda 2$ and $\lambda 3$ (blue green and red).

Left to right operation

It works as follows; first when port one is used the operating wavelength is green. Light passes through the input ring (blue) because of the mismatch in the resonance condition. Then, it couples to the wavelength conversion unit which supports the signals at the green wavelength as shown in Fig.6.15. After the conversion takes place the new wavelength of the signal is blue which enables it to pass through the output ring without any coupling. Any reflected signals as in the unidirectional isolator will be isolated from the input through the drop port by the blue ring.

Right to left operation

If port two is used as an input port. The pulse is centered at red wavelength. The place of this wavelength in the conversion spectrum is shown in Fig.6.15. Light passes through the input ring (green) because of the mismatch in the resonance condition, then couples to the wavelength conversion unit. This will change the wavelength to green according to Fig.13. This allows it to pass by the blue because of the mismatch in the resonance conditions and couple to the output port. All back reflections are filtered from using the green filter in a similar fashion to the uni-direction isolator.

6.4 Summary

We present a novel design for an active integrated optical isolator for high bit rate transmission of data employing adiabatic wavelength conversion to realize a non-reciprocal system that consists mainly CMOS compatible components. The isolator uses novel sampling methods (time domain sampling or frequency domain sampling) to ensure complete isolation of optical pulses. The presented device achieves isolation of up to 24 dB. In addition, we have presented a bi-directional isolation device which can play a crucial role in high bit rate wavelength division multiplexed system (WDM). The system delivers bidirectional isolation of separate wavelength channels to help integrate more complex photonic system on a single chip

CHAPTER SEVEN

BROADBAND ULTRA-FAST PHOTON SWITCH

7.1 Introduction

Nanophotonic circuits have great promise for overcoming the limitations of electronic interconnects, especially in applications that require high bandwidths, low powers and low noise. Crystalline silicon is now the preferred platform for building these nanophotonic devices because of its low intrinsic loss at telecommunication wavelengths, the compatibility with CMOS processes, and high index contrast.

One of the most important components of a nanophotonic communication system is a fast electro-optic modulator, which takes in a DC optical input signal and switches it on/off using a high data-rate electronic signal. Modulation is achieved by inducing a change in the phase or the intensity of the light, using a refractive index change or an absorption change, respectively. In silicon the free-carrier plasma dispersion (FCPD) effect can achieve both [23,26,27,106]. However, in all recently demonstrated electro-optic devices the FCPD has been relatively small, requiring either very large photonic devices or devices that leverage resonant effects to increase the sensitivity to small refractive index changes. However, using resonant effects come with a tradeoff – the bandwidth of the device dramatically decreases. This is especially true for modulators based on micro-resonators, such as rings or discs [23,26,27,107]. The bandwidth of these resonators is so small that they are extremely sensitive to temperate variations, and very small fabrication imperfections. To overcome this limitation, high powered and complicated compensation techniques are required to precisely set and maintain the resonant wavelengths of all of

the devices on the chip [108]. Alternatively, Mach-Zehnder interferometer modulators have been demonstrated which significantly increase the optical bandwidth [22,35]. Although the system described in [45] achieves modulation speeds up to 30Gb/s, it is relatively large (~3mm long) due to the small overlap of the light with the carrier modulation. While sub-micron waveguides can reduce the overall size of the modulator [46], the overall photonic structure has a more complex structure than the one proposed here. In addition, both modulators in [22,35] suffer from significant free-carrier absorption due to the overlap of the optical mode with doped regions and/or injected carrier densities. In contrast, here we utilize the inherent free-carrier absorption present in FCPD modulators to realize a broadband, high speed, compact, electro-optic modulator.

Here we propose a very simple modulator that solves the problems encountered with the previous structures. This modulator is fundamentally different from all the other recently demonstrated modulators in that it relies on the absorption change in silicon instead of the refractive index change. Therefore, it does not require a resonance or interference effect, it just requires a simple short waveguide. Since light is just absorbed, the device inherently operates over the entire bandwidth of the waveguide where the mode has sufficient confinement (more than 100nm bandwidth centered at wavelength of 1.55μm). As a result of this the device has minimal sensitivity to process variations which allows the integration of multiple matched devices on the same chip without the use of any complicated structures for wavelength insensitivity [109]. The modulator is realized by integrating Schottky diodes into the waveguide to control the free-carrier density. Schottky diodes have a significant advantage over traditional PN/PIN diodes because

they are majority-carrier devices that operate with very low turn on voltages, and are very fast [23]. The proposed design has a very high overlap between the optical mode and the large modulated carrier density, which results in a large change in the optical absorption over a short length. This is in stark contrast to previously demonstrated electro-absorption modulators based on free-carriers in Silicon that were inherently slow and large in size due to their reliance on PN/PIN diodes [25,110]. In addition, while Germanium-on-Silicon modulators based on the Stark effect are showing initial promise they inherently require a significantly more complicated integration and fabrication scheme than the device proposed here [111]. In the following sections the design of our simple modulator is presented with models to monitor the behavior of the device and the transient response for fast switching operation.

7.2 Modulator design

The modulator structure is simply a 100μm long silicon-on-insulator single mode waveguide. The waveguide dimensions are 250nm in height, including a thin 50nm rib, and 450nm in width, as seen in Fig.7.1. The middle region of the waveguide is lightly doped to $10^{16}cm^{-3}$ with P type dopant (Boron). This concentration as will be seen in our simulations results in a low OFF state loss, and a wide depletion region due to the internal voltage difference between the Schottky contact and the doped silicon. The ribs on the sides of the waveguide are heavily P doped to $10^{19}cm^{-3}$. When the device is turned ON holes from these ribs are injected into the middle region where the optical mode resides. The device has three terminals, two ohmic Aluminum contacts connected to the heavily doped ribs 700nm away from the waveguide in order to minimize the loss, and a single 50-nm wide Aluminum Schottky contact (Gate) connected to the top of the

waveguide. The contact resistance in the modeling is assumed to be 2KΩ which matches previous analytical models [24] and experimental results [27]. While the positioning of the gate on top of the waveguide and the P+ doped regions do induce some insertion loss, the total insertion loss of the device is only 2.98dB. While a larger metal region will be needed to make electrical contact to this gate, a modest via of size 200X200nm placed anywhere along the top of the waveguide would introduce an additional attenuation of only 3%. The electrical arrangement of our modulator has a significant advantage over commonly used PN/PIN based approaches such as [22,27] in that the carriers are forced to flow directly through the center of the waveguide where the optical mode resides, ensuring optimal light and free-carrier concentration overlap.

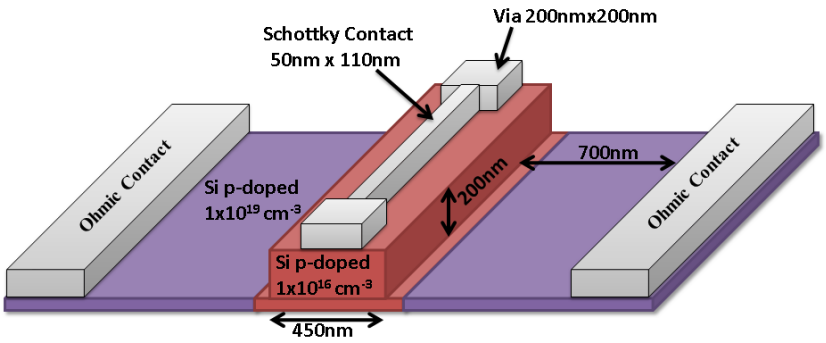

Fig. 7.1 Cross-section of the Schottky diode waveguide modulator. The device consists of a lightly doped center region where the light is confined. A 50nm wide Schottky contact is attached to the top. A 50nm highly doped rib is at the bottom of the waveguide where ohmic contacts (700nm away from the center region) are attached. The waveguide is embedded in silicon dioxide. The device length is 100 μm (not to scale).

7.3 Electrical and optical modeling

The device is simulated using a two-dimensional simulation package ATLAS from SILVACO [112]. This program simulates internal physics and device characteristics of

semiconductor devices by solving Poisson's equation and the charge continuity equations for electrons and holes numerically. The software allows a complete statistical approach (Fermi–Dirac statistics) when heavily doped regions are considered [21]. The suitability of this device modeling package to analyze electro-optic modulators in SOI waveguides has been demonstrated by several other authors [19-21,24]. Several physical models were used to accurately predict the behavior of the device such as field and concentration dependant mobility, Shockley-Read-Hall (SRH) recombination model, Auger recombination model and band narrowing for the regions with high carrier concentration. A surface recombination model is also used to account for the semiconductor/insulator interface recombination. The carrier interface recombination velocity and the surface recombination velocity are taken as 8000 cm/s each [55], while the electrons and hole lifetimes in bulk silicon are taken as 3μs and 10μs respectively [55]. The highly doped are assumed to have an abrupt junction [53] for simplicity. This has a negligible effect on the carrier transport phenomena of the devices compared to realistic Gaussian profiles with 35nm normal deviation [54]. The design of these devices allows for the junctions to have a fast lateral decay rate when they are realized using low KeV ion implantation. The top Schottky contact is made from Aluminum which has a work function of 4.1eV [23]. The ohmic contacts are also made from Aluminum and connected to the heavily doped P regions. The behavior of the aluminum contact (i.e. whether it is ohmic or Schottky) simply depends on the doping level/work function of the silicon it is attached to. In practice a short low-temperature anneal (400-500C) may be required to form a good quality Schottky contact.

A finite difference mode solver was used to calculate the complex effective index of the waveguide in order to characterize the wave propagation and loss. Taking into account all of the doped regions, carrier concentrations [18] and metal contacts (analyzed with Drude model) the complex effective index of the mode obtained from the optical simulation is used to calculate the transmittance of an optical signal through the modulator using the following equations:

$$T = e^{(-\alpha \cdot L)} \tag{7.1}$$

$$\alpha = \frac{n_g}{\mathrm{Re}(n_{eff})}(4\pi/\lambda) \cdot \mathrm{Im}(n_{eff}) \tag{7.2}$$

where α denotes the power absorption coefficient, L is the length of the device, n_g is the group index of the waveguide, Re(neff) is the real part of the complex effective index, λ is the wavelength of operation and $\mathrm{Im}(n_{eff})$ is the imaginary part of the effective index. The first term of equation 4.39 essentially accounts for the slowed propagation of the light due to the reduced group velocity of the mode in the waveguide. This term is important in nanosized waveguides because the group index is significantly larger than the effective index of the mode [113]. The group index is calculated using the mode solver and the well known equation:

$$n_g = n_{eff} - \lambda \frac{dn_{eff}}{d\lambda} \tag{7.3}$$

7.4 Performance Analysis

Fig 7.2 shows the calculated hole carrier distribution profile when the device is OFF. Taking this off-state carrier concentration into account and all other sources of optical losses, such as the metal contacts, a characterization of the optical mode was made to measure the effective index and intrinsic loss of the device.

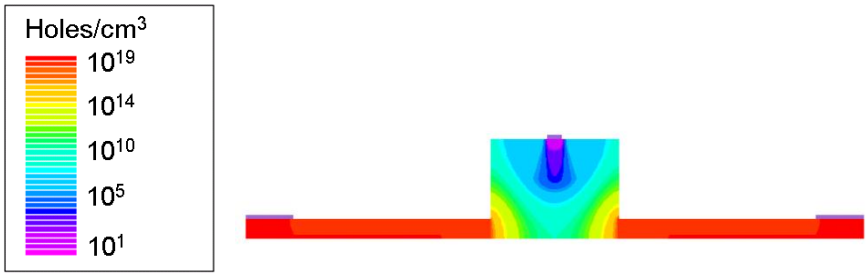

Fig 7.2. The hole carrier concentration density profile in the devices off-state. It is seen that there is a very low carrier concentration in the center waveguide region where the light resides.

Fig 7.3 shows the calculated mode profile for the magnetic and electric fields of the TE mode. It is seen that most of the light resides in the central region with a very low carrier concentration, and consequently low initial loss.

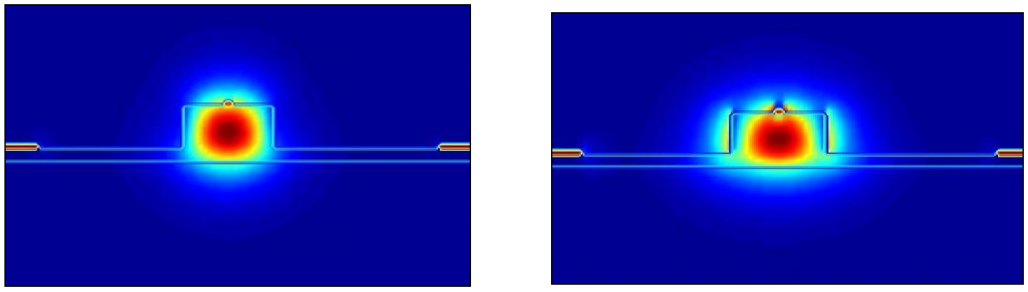

(A) **(B)**

Fig.7.3. The (A) vertical magnetic field intensity and (B) horizontal electric field for the TE mode of the waveguide.

The dependence of the real and imaginary part of the effective index on wavelength is shown in Fig 7.4 taking into count the material dispersion of silicon, oxide, and aluminum [114]. . At the operating wavelength of 1550nm the real part of the effective index is found to be 2.5817, and the imaginary part is 5.17E-04. The absorption coefficient is related to the imaginary part of the refractive index by equation (7.1), which then can be used to calculate the transmission of the device using equation (7.2). From this we find that the device has an insertion loss of only 2.98dB for a device length of

100μm (n_g=3.996) even though there is metal directly on top of the waveguide. In addition, the insertion loss only varies by .78 dB over a 100nm bandwidth as plotted on the right y-axis of Fig 7.4b, which demonstrates the very broadband nature of the device.

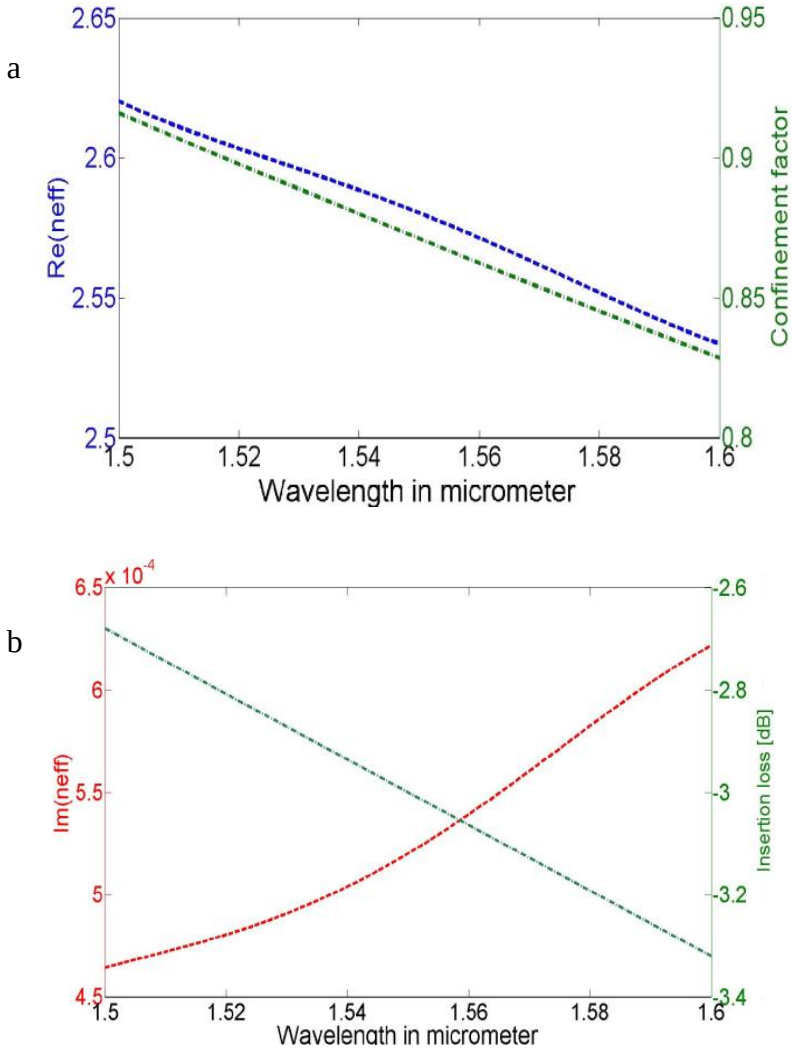

Fig.7.4 (A) Real part of the effective index (blue) and the amount of power confined in the central silicon region where the carrier concentration is modulated (green). (B) Imaginary part of the effective index (red) and the total insertion loss of a 100μm long device (green).

Unfortunately losses are much higher for the other polarization state but with the recent demonstration of polarization rotators on a chip, it is possible to have an entire chip operating at a single polarization [115].

As mentioned earlier modulation in the optical signal is achieved through a change in absorption by injecting/extracting a high carrier density into the optical mode. The carrier concentration is modulated by applying a forward or reverse bias to the gate while connecting the other two ohmic terminals to ground. Here we use a maximum reverse bias voltage of +1.25V, and a minimum forward voltage of -1.25V. Reverse bias (forward bias) occurs with a positive (negative) voltage because the device is P doped We can see the low hole concentration in the waveguide region under reverse bias in Fig 7.5(a), and the very high hole concentration in the forward biasing operation in Fig 7.5(b). It is seen that there is a very large change in carrier concentration (10^{19}) exactly where the optical mode resides. Such a large carrier concentration change results in a very large change of the absorption coefficient of the device, which is directly leveraged to modulate light in the waveguide.

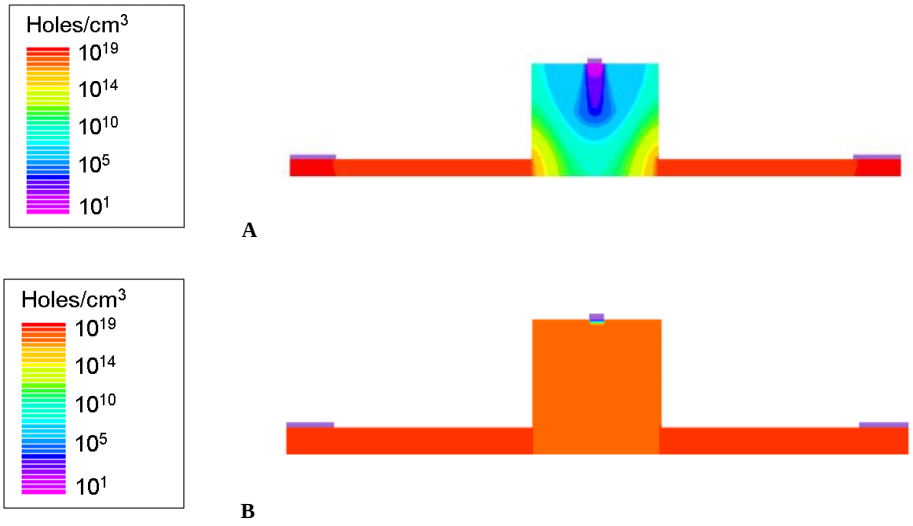

Fig.7.5. The log of the hole density profile with a (A) 1.25V reverse bias and (B) a 1.25V forward bias. The change in the absorption coefficient is calculated using the change in the electron and hole concentration with the following equation.

$$\Delta\alpha_{fc} = [8.5\times10^{-18}\times\Delta N + 6\times10^{-18}\times\Delta P] \quad 7.4$$

where $\Delta\alpha_{fc}$ is the change in the free-carrier absorption coefficient per unit length (cm^{-1}), and ΔN and ΔP are the change in the electron and holes density per cm^3, respectively. The carrier distribution in Fig 7.5.a represents the reverse biased condition (OFF state) where the operating voltage is below the threshold of the device and there is low carrier concentration where the optical mode resides. Although the carrier density changes with space ($10^9 cm^{-3}$ to $10^{14} cm^{-3}$ over the whole waveguide) it has a negligible effect on the free carriers loss at this state according to equation (7.4) $\Delta\alpha_{fc} \sim 0$. Once a current is established in the device (forward biased junction, voltages >0.5V) the carrier concentration is extremely uniform ($10^{15} cm^{-3}$) over the entire active region of the mode due to the small waveguide dimensions and the vertical design of the contacts as seen in Fig. 7.5b. Therefore, as a simplification it can be assumed that the carrier concentration is a constant over this entire region in the forward bias operation and the approximate change in the modes absorption coefficient is given by [113] :

$$\Delta\alpha = \frac{n_g}{n_b}\gamma_{fc}\Delta\alpha_{fc} \quad 7.5$$

where $\Delta\alpha$ is the change in modes absorption coefficient, n_g is the group index, n_b is the bulk index of silicon (3.46□□ and γ_{fc} is the free-carrier spatial confinement factor of the mode which accounts for the amount of light that interacts with the modulated free-carrier concentration (i.e. in the center) and is give by equation (7.6) [113]. Due to the strong overlap of the light with the free-carriers we find that this confinement factor is 87%.

$$\gamma_{fc} = \frac{\iint_{center} \varepsilon |E|^2 dxdy}{\iint_{\infty} \varepsilon |E|^2 dxdy} \qquad 7.6$$

Since ng/nb=1.15, we find that $\Delta\alpha=1.003\Delta\alpha_{fc}$, which allows us to simplify that the change in the absorption of the mode is approximately just given by equation (7.4). From this we can directly calculate the change in transmission from the modulated carrier-concentration using equation (7.1). Lastly, the right y-axis of Fig 4.32a shows the change in the confinement factor given by equation (7.6) as a function of wavelength. We see that it varies by only 9% and the approximation we make here is approximately valid over more than 100nm bandwidth.

Fig 7.6 shows the negative of the input signal applied to the gate (the signal is flipped to conform with normal convention that positive voltages correspond to a forward-biases) in order to demonstrate the high speed of the proposed modulator. It is seen that the forward bias voltage is pre-emphasized with a -4V short voltage pulse and then reduced to -1.25V. This pre-emphasis technique has been commonly used in the forward biasing of previously demonstrated ring resonator and Mach Zehnder PIN modulators [24,35]. Pre-emphasis effectively increases the power of the high frequency components of the input signal which consequently increases the speed that the effective carrier concentration is injected.

Fig 7.8 shows the optical response of the 100micrometer long waveguide device to the voltage signal applied in Fig 7.7 (calculated using Equation 7.1and 7.4).

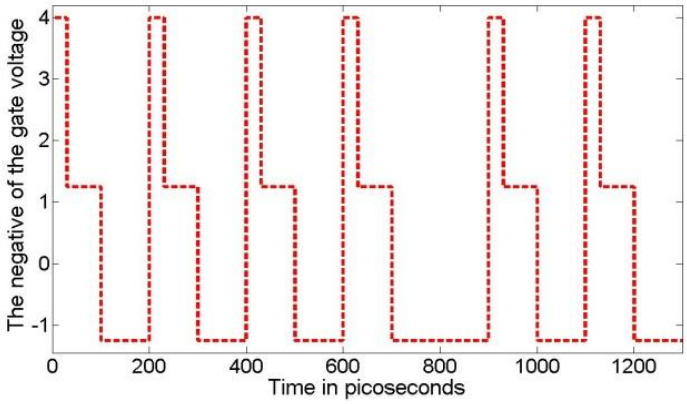

Fig. 7.6 10 Gbit/s gate voltage applied to the Schottky modulator device.

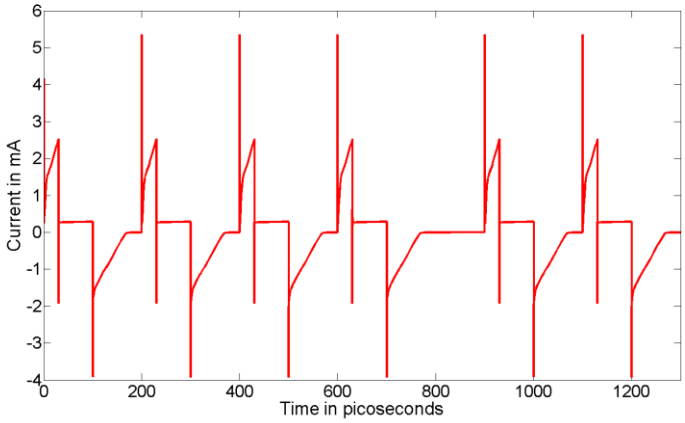

Fig. 7.7 Gate current in the Schottky modulator device.

It is seen that the modulation depth of the device is more than 65% (~4.6 dB). A larger modulation depth can be achieved with a tradeoff in insertion loss as explained below.

Fig 7.9 gives a closer look at the response of the carriers over one period of the voltage input signal. The device reaches steady state OFF transmission (High carrier concentration) in only 30ps from the ON state (Low carrier concentration), and only takes 60ps to go from OFF to back ON. The high speed of the device and large majority carrier concentration change (1E19) are directly enabled by the use of a Schottky junction which work by thermionic emission of majority carriers over the barrier created by the unequal work functions between a metal-semiconductor interface.

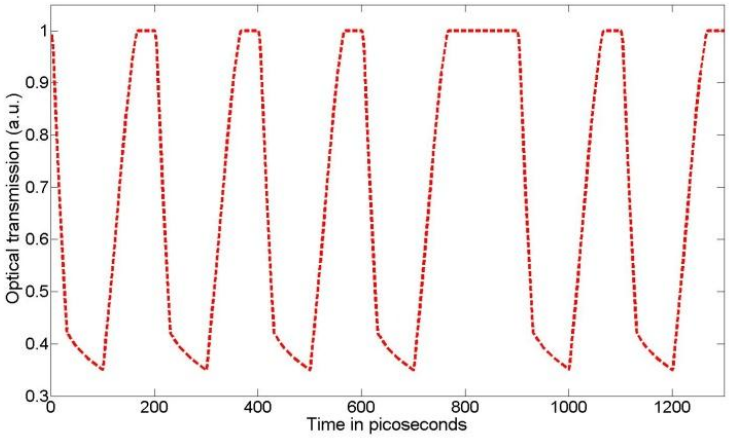

Fig. 7.8 Optical response of the Schottky modulator to the gate signal applied in Fig. 7.7. It is seen that a modulation depth of > 4.6 dB is achieved at a bit-rate of 10 Gbit/s.

This is in stark contrast to the operation of PN/PIN devices, which are limited by relatively small and slow minority carrier concentration processes, which inherently require ultrasensitive and complex interference based optical devices in order to achieve significant modulation [22,27,35,106]. The fast transition times of the Schottky device enable operation at speeds of 10 Gbit/s and our modeling indicates that even faster switching is possible with a tradeoff of higher insertion loss.

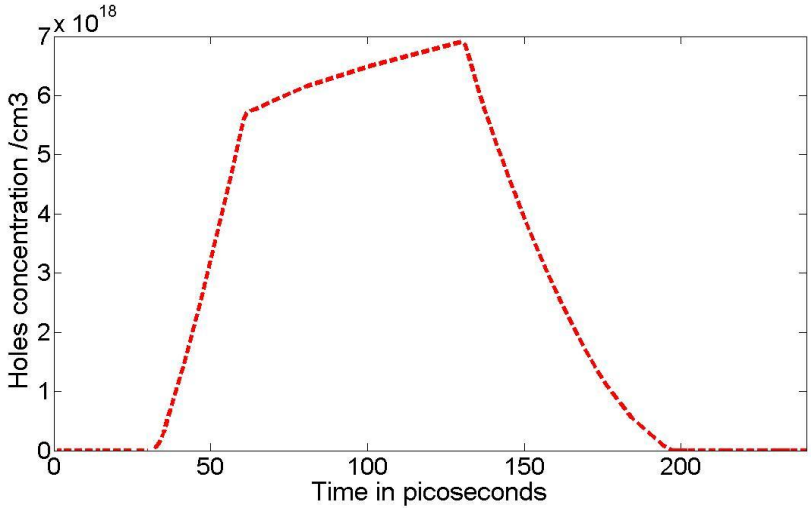

Fig.7.9 Hole concentration over one period of an applied gate signal. It is seen that the rise time of the concentration is only 30 picoseconds and the fall time is 60 ps.

It is important to note that our device does not have any RC constant limitations due to the low capacitance of Schottky diodes in comparison with PIN diodes. The depletion capacitance of the entire device was calculated to be 50fF compared to larger values in PIN structures of 200fF [46]. In order to accurately characterize the RC time constant of the system, the resistivity of the top aluminum contact (thickness of 110nm) was determined based on theoretical models and experimental measurements in [116]. Usually metal contacts such as copper with a line width approaching the electron mean free path (EMFP) (39 nm at room temperature) experience a strong increase in resistivity that is attributed to surface and grain boundary scattering. This phenomenon can be studied in different metals using Fuchs–Sondheimers (FS) surface scattering and Mayadas–Shatzkes (MS) grain boundary scattering models. However, this increase in the resistance is less pronounced in aluminum contacts with the same size due to the small EMFP of 15nm [22]. The sizes of the contacts used (gate 50nmX110nm) in the design are much larger than the EMFP size limit, which makes the resistivity approach the bulk values of 2.66 μohm.cm for aluminum. Based on the resistivity value we can easily calculate the input resistance to be 245Ω (equation 4.44) looking from the gate to the drain and the source. Although the current in the modulator flows vertically from the gate to the source and drain there is some current conduction along the length of the device through the gate contacts due to the finite conductivity of aluminum when voltages are connected to the vias (gate region shown in Fig 7.1) while the drain and source are grounded. This creates an equipotential point in the center of the gate. Lastly, the input resistance can be further reduced using multiple vias with a tradeoff of more insertion loss.

$$R = \rho \frac{L}{A} \tag{7.7}$$

Where ρ is the resistivity, L is the contact length (50μm) and A is the contact area (110nmx50nm). The time constant of the device can be calculated as follows

$$\tau = \mathrm{RC} = 50^{-15} \times 245 = 12.75 \text{ picoseconds} \tag{7.8}$$

Finally the cut-off frequency of the device is calculated from the RC time constant

$$\mathrm{F} = \frac{1}{2\pi \mathrm{RC}} = \frac{1}{2\pi \times 12.75\mathrm{ps}} = 12.5 \text{ GHz} \tag{7.9}$$

The cut-off frequency is higher than the operation speed of the device of 10GHz. This shows that the device has no RC speed limitations.

As explained earlier there is an inherit tradeoff between modulation depth and insertion loss in the proposed device. As the device is made longer the off-state insertion loss from the metal gate and highly doped regions increases as seen in Fig 7.10. However, the modulation depth is increased due to the additional free-carrier absorption from the majority carriers. These trade-offs can be varied slightly by modifying the device geometry (wider gate contact, with a tradeoff in additional loss), but this also results in a change in the operating speed and maximum carrier concentration of the device. One additional source of loss in the system which has a negligible effect on the performance is scattering loss. It mainly consists of an inherent waveguide scattering loss and mode mismatch loss through coupling light to the modulator. The first type comes from the rough side-walls of the waveguide due to the etching process. A typical value for the attenuation is 3dB/cm [117] which comes to an insertion loss of ~0.03dB for the total length of the modulator (100μm). The second type of scattering loss comes from the

small mode mismatch at the input/output ports of the modulator with the silicon waveguide. This is due to the presence of contact vias and aluminum gate on the top of the waveguide. We performed mode mismatch calculations and estimated the insertion loss from this effect to be ~0.2dB. In summary the total insertion loss of the device including all the scattering loss mechanisms metal loss, carrier losses, scattering loss, and mode mismatch loss is approximately 3.25dB,

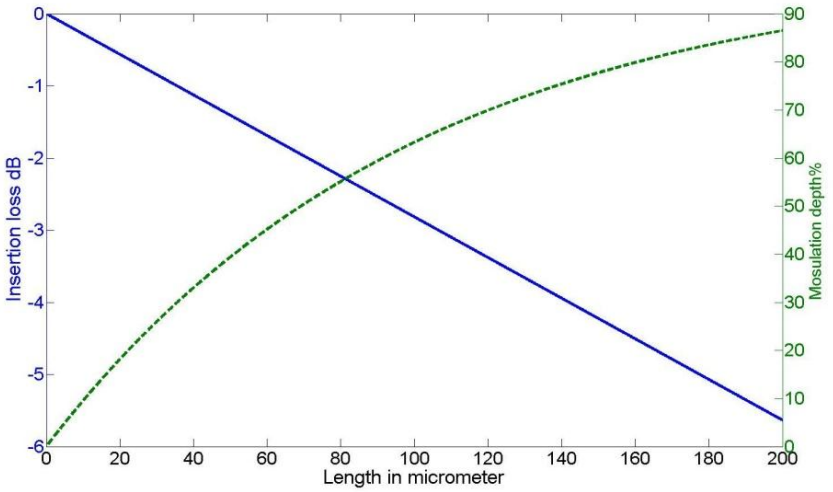

Fig. 7.10 Insertion loss and modulation depth of the device as a function of device length.

Lastly, although the device draws more current than PIN devices (consequently more power), its high switching speed and ultra-high continuous bandwidth (more than 100nm) makes it a vital component in broadband optical communication systems. Hundreds of channels from different systems can be processed in the same device because of the absence of any wavelength dependence. While large ring resonators (radius>100 μm) have been demonstrated to switch many ITU channels simultaneously, they would require a similar switching power as used here due to their inherently large circumference of ~1 mm [118]. However, they would still require the use of complicated temperature

compensation schemes. Another advantage is the robustness of the design to fabrication imperfections; because the device simply consists of a straight waveguide it can be built in any length without having precise dimensions and even looped as spirals to reduce the overall footprint on chip. In terms of modulation there are no complexities of matching resonances or using feedback techniques for stable operation through fixing the operating point as required in resonant or interference structures.

7.5 Summary

Here we've proposed a design for a simple broadband silicon electro-optic modulator based on free-carrier absorption in a silicon-on-insulator waveguide. The device is capable of at least 10 Gbit/s operation and with further tuning of the device geometry, such as waveguide dimensions and the Schottky gate width, the device can be tuned for higher speed operation or lower loss. The modulator design maximizes the overlap between the optical mode and injected carriers which resulted in the compact size of the. The broadband nature of the systems enables it to modulate hundreds of wavelength multiplexed channels without the use of any complex tuning or compensation techniques.

CHAPTER EIGHT

CONCLUSION AND FUTURE DIRECTION

8.1 Conclusion

In this work we have theoretically investigated and experimentally demonstrated novel photonic devices that manipulate photons on silicon chip. The research mainly focused on the interaction between photon number states and traveling wave photonic cavities. The active nature of the cavities along with non-classical behavior of photon number states result in exciting new phenomena. The energy eigenstates of photons can be manipulated. In addition, time-bin entangled states can be created in a compact cavity which opens the door for new quantum encryption schemes. Also, we showed that photons can be stored efficiently in multi-cavity systems. This will aid the development of on-chip optical signal processing where delay elements are essential. Moreover, we demonstrated that by designing a system of cavities a photonic transition can be controlled. The results play an important role in WDM systems where blue- and red-wavelength shifts are needed when carriers are injected. Finally, incorporating active control on the cavities can dramatically change the transmission characteristics of the system to isolate certain paths. The following section summarizes the major contributions of the work.

8.2 Major Contributions

The following are major novel contributions presented in the work:

1- Derived a dynamic model for single-photon cavity interaction.

2- Developed a novel FDTD algorithm that predicts the scattering behavior of single-photon wavepackets with cavities in space-time domain.

3- Proved that photons change their eigenenergy state in active optical cavities with 100% efficiency.

4- Experimentally demonstrated adiabatic wavelength conversion and discrete transitions of single photons in active cavities.

5- Experimentally generated photon pairs in an atom-like photonic structure through 4-photon scattering.

6- Designed and experimentally demonstrated an on-chip photon memory with a record storage time of 300 picoseconds.

7- Proposed and numerically investigated a photonic molecule structure that controls photonic transitions regardless of the index change sign.

8- Analyzed a novel CMOS compatible isolator that breaks the time reversibility using only active optical cavies.

9- Designed and numerically tested a new broadband photon switch with a bandwidth of more than 100nm operating at 10Gb/s.

8.3 List of My Publications

Most of the original contributions have been published in journals or presented at conferences. Following is the list of publications and patents I achieved in this research with number of citations as of October 2011.

Journal Publications

2011

- **Ali W. Elshaari**, and Stefan F. Preble "*Engineered Transitions in photonic molecules* " Optics Express (submitted).

2010

- Edwin E. Hach III, **Ali W. Elshaari**, and Stefan F. Preble "*Fully quantum mechanical dynamic analysis of single-photon transport in a single-mode waveguide coupled to a traveling-wave resonator* "Physical Review A, **82**, 063839, Dec-2010. (Cited 1 time)
- **Ali W. Elshaari** and Stefan F. Preble "*10Gb/s Broadband Silicon Electro-Optic Absorption Modulator* " Optics Communication, **283**, 2829-2834, Jul-2010. (Cited 1 time)
- Abdelsalam A. Aboketaf, **Ali W. Elshaari**, and Stefan F. Preble "*Optical Time Division Multiplexer on Silicon Chip*" Optics Express, **18**, 13529-13535, Jun-2010. (Cited 1 time)
- Karthik Narayanan, **Ali W. Elshaari**, and Stefan F. Preble "*Broadband All-Optical Modulation in Hydrogenated-Amorphous-Silicon Waveguides*" Optics Express, **18**, 9809-9814, May-2010. (Cited 8 times)
- **Ali W. Elshaari**, Abdelsalam. A. Aboketaf, and Stefan F. Preble "*Controlled Storage of Light in Silicon Cavities* " Optics Express, **18**, 3014-3022, Feb-2010. (Cited 3 times)

Conference Publications

2010

- Abdelsalam A. Aboketaf, **Ali W. Elshaari**, and Stefan F. Preble "*Optical Time Division Multiplexer on Silicon Chip*", Frontiers in Optics (FIO), Oct-2010 .
- **Ali W. Elshaari**, Abdelsalam. A. Aboketaf, and Stefan F. Preble "*Toward Optical Memory on Silicon Chip* " Lester Eastman (LE), Aug-2010.
- Abdelsalam A. Aboketaf, **Ali W. Elshaari**, and Stefan F. Preble "*Optical Time Division Multiplexer on Silicon Chip*", Lester Eastman (LE), Aug-2010.
- Liang Cao, **Ali W. Elshaari**, Abdelsalam. A. Aboketaf, and Stefan F. Preble "*Adiabatic Couplers in SOI Waveguides*" Conference on Lasers and Electro-Optics (CLEO), May-2010.

2009

- **Ali W. Elshaari** and Stefan F. Preble "*Nanosecond Tunable Optical Delay Using Silicon Cavities*" Frontiers in Optics (FIO), Oct-2009. (Cited 1 time)
- **Ali W. Elshaari** and Stefan F. Preble "*Active Optical Isolator Using Adiabatic Wavelength Conversion in Microcavities*" Frontiers in Optics (FIO), Oct-2009. (Cited 2 times)

2008

- **Ali W. Elshaari**, Stefan F. Preble, and M. Ali G, Abushagur "*Broadband Silicon Electro-optic Absorption Modulator*" Frontiers in Optics (FIO), Oct-2008.
- **Ali W. Elshaari**, Stefan F. Preble, C. Cress, R. Raffaelle, and M. Ali G. Abushagur "*Towards a Low-Q Erbium Doped Silicon Laser*" Frontiers in Optics (FIO), Oct-2008.

8.4 Future Direction

The field of quantum photonic circuits is fast growing field with many research possibilities. After improving each building block in the network, the natural step is to start integrating on the system level. This can be done by combining multiple elements together to form small networks. Then we can study the effects of integration and the linearity of the overall system. In addition, unique states interaction with optical cavities needs to be investigated such as high order N00N states and squeezed states which are very important in quantum communication. Moreover, for all of these systems to be useful, the fabrication process needs to improve dramatically to reduce the waveguide loss, which is a big challenge with the current circuits resulting in low signal to noise counts. Also, more research is required to integrate single photon super conducting detectors on chip to reduce the size of the system and efficiently process the results. This will require an extensive study of the compatibility of these materials with silicon platform. In addition, a detailed study of the behavior of silicon waveguides, cavities, and carrier dynamics at cryogenic temperatures must be performed.

Finally, these systems are although difficult to implement at the moment, but when developed they will revolutionize the way we think about computers in addition to the ultra-fast and secure communication we can achieve.

APPENDICES

Appendix I

Resonator with carrier injection (Classical CMT model Matlab)

```
% *******   defining constants and field matrices *******
Ea1(1:time_steps)=0; Eb1(1:80000)=0; Ec1(1:time_steps)=0;
Ed1(1:time_steps)=0;
Ea2(1:time_steps)=0; Eb2(1:80000)=0; Ec2(1:time_steps)=0;
Ed2(1:time_steps)=0;
E_through(1:time_steps)=0; E_drop(1:time_steps)=0;
index(1:time_steps)=0;neff(1:time_steps)=0;phase(1:time_steps)=0;
gamma(1:time_steps)=0;field_absorption_per_meter(1:time_steps)=0;
Q(1:time_steps)=0;carriers(1:time_steps)=0; index(1:time_steps)=0;


%%
q=1.6e-19;
c=299792458;
Resistance=200;                          % silicon/metal contact
resistance
vth=0.7;                                  % Threshold voltage for PIN
tauc=(1/2.3)*1e-9;                        % Carrier life time
capacitance=1e-15;
volume=2*pi*R*1e2*.45e-4*.25e-4;          % Ring volume in cm3
%dt=ng*pi*1e-6/c;


t_through=sqrt(1-k_through.^2);
t_drop=sqrt(1-k_drop.^2);
```

```
        if k_drop>0
            % loss from drop ring
            gamma0=0.6908*100*2*pi*R*0.5;
        else
            % loss from throgh port for critical coupling
            gamma0=sqrt(1-k_through.^2);
            gamma0=-log(gamma0);
        end


% *******   Main time evolution loop *******
for tt=20:time_steps
        if voltage(tt)>0
                Q(tt)=Q(tt-1)+dt*((1/Resistance)*(voltage(tt-1)-vth)-
Q(tt-1)/tauc);
        else
              if Q(tt)>0
                Q(tt)=Q(tt-1)+dt*((1/Resistance)*(voltage(tt-1)-vth)-
Q(tt-1)/tauc);
              else
             %   Q_M1P1(tt)=Q_M1P1(tt-
1)+dt*((1/Resistance)*(voltage_M1P1(tt-1)-Q_M1P1(tt-1)/capacitance)-
Q_M1P1(tt-1)/tauc);
                Q(tt)=0;
              end
        end
      carriers(tt)=Q(tt)/(q*volume);
      index(tt)=(8.8e-22*carriers(tt)+8.5e-18*carriers(tt)^.8);
```

```
      neff(tt)=n_eff-real(index(tt));
      phase(tt)=neff(tt)*(2*pi/res_wavelength)*2*pi*R;
      field_absorption_per_meter(tt)=.5*14.5e-18*carriers(tt)*100;
      gamma(tt)=gamma0+field_absorption_per_meter(tt).*2.*pi.*R;

% *******   saving time domain matrices *******
    Ea1(tt)=E_input(tt);
    Eb1(tt)=Ed2(tt-R/1e-6)*exp(-gamma(tt)/2+1i*phase(tt)/2);
    Ec1(tt)=t_through*Ea1(tt)+1i*k_through*Eb1(tt);
    Ed1(tt)=1i*k_through*Ea1(tt)+t_through*Eb1(tt);
    Ea2(tt)=0;
    Eb2(tt)=Ed1(tt-R/1e-6)*exp(-gamma(tt)/2+1i*phase(tt)/2);
    Ec2(tt)=t_drop*Ea2(tt)+1i*k_drop*Eb2(tt);
    Ed2(tt)=1i*k_drop*Ea2(tt)+t_drop*Eb2(tt);
    E_through(tt)=Ec1(tt);
    E_drop(tt)=Ec2(tt);
    indx(tt)=index(tt);
end
    E_through(1,time_steps+1)=0;
    E_drop(1,time_steps+1)=0;

    carriers(1,time_steps+1)=0;
    indx(1,time_steps+1)=0;
end
```

Appendix II

Single Photon-Cavity Dynamics (Quantum FDTD model Fortran)

MATLAB SECTION

```
%% ***** CALL FORTRAN ROUTINE ******
clear all
close all
clc
!g95 photon1.f95
!a
%% ***** TIME DOMAIN MATRICES *****
load time
load h
load in
load out
load wc
load dt
ht=h(:,1)+1i*h(:,2);
int=in(:,1)+1i*in(:,2);
outt=out(:,1)+1i*out(:,2);
figure
subplot(3,1,1)
plot(time(:,1),ht.*conj(ht),'-r', 'LineWidth', 3)
title('|0 1> state in the cavity')
xlabel('time')
subplot(3,1,2)
plot(time(:,1),int.*conj(int),'-b', 'LineWidth', 3)
title('|1 0> input state waveguide')
```

```
xlabel('time')
subplot(3,1,3)
plot(time(:,1),outt.*conj(outt),'-g', 'LineWidth', 3)
title('|1 0> output state waveguide')
xlabel('time')
%% ***** FFT OF TIME MATRICES *****
N=length(ht);
hf=fft(ht,N);
hf=fftshift(hf);
inpf=fft(int,N);
inpf=fftshift(inpf);
outf=fft(outt,N);
outf=fftshift(outf);
frequency=((-N/2):(N/2-1))*1/(N*dt);
figure
subplot(3,1,1)
plot(2*pi*frequency/wc,flipdim(hf.*conj(hf)/N,1),'-r', 'LineWidth', 3)
title('|0 1> state in the cavity')
xlabel('frequency unit wc')
xlim([0 4])
subplot(3,1,2)
plot(2*pi*frequency/wc,flipdim(inpf.*conj(inpf)/N,1),'-b', 'LineWidth',
3)
title('|1 0> input state waveguide')
xlabel('frequency unit wc')
xlim([0 4])
subplot(3,1,3)
plot(2*pi*frequency/wc,flipdim(outf.*conj(outf)/N,1),'-g', 'LineWidth',
3)
```

```
title('|1 0> output state waveguide')
xlabel('frequency unit wc')
xlim([0 4])
%% ***** DFT PART IN CODE *****
% load hf
% load inpf
% load outf
% figure
% subplot(3,1,1)
% plot(frequency(:,1),hf(:,1).^2+hf(:,2).^2)
% xlim([5e5 15e5])
% subplot(3,1,2)
% plot(frequency(:,1),inpf(:,1).^2+inpf(:,2).^2)
% xlim([5e5 15e5])
% subplot(3,1,3)
% plot(frequency(:,1),outf(:,1).^2+outf(:,2).^2)
% xlim([5e5 15e5])
```

FORTRAN SECTION

```
PROGRAM photon
IMPLICIT none
!***** constatnts*****
INTEGER, PARAMETER :: N=1E3, tend=1E5, N1=495, N2=505,fend=1E6
REAL, PARAMETER :: vg=1, dt=0.5E-8, dx=1E-8, wc=1E6, wo=1E6, twidth=1E-
5, pi=3.14159265
!***** variables definition *****
INTEGER j,i,d
REAL gamma,df
REAL, ALLOCATABLE, DIMENSION(:,:) :: time, frequency
```

```
COMPLEX, ALLOCATABLE, DIMENSION(:,:) :: f,fold,h,in,out,hf,outf,inpf
COMPLEX ci,sum,V
ci = cmplx(0.,1.)
V=.01*ci*wc
gamma=.01*wc
df=10
100 format (9999E15.6)
ALLOCATE(f(1,1:N))
ALLOCATE(fold(1,1:N))
ALLOCATE(in(1,1:tend))
ALLOCATE(out(1,1:tend))
ALLOCATE(h(1,1:tend))
ALLOCATE(time(1,1:tend))
ALLOCATE(frequency(1,1:fend))
ALLOCATE(hf(1,1:fend))
ALLOCATE(inpf(1,1:fend))
ALLOCATE(outf(1,1:fend))
!***** initialize variables *****
sum=0
f=0
fold=0
in=0
out=0
h=0
time=0
frequency=0
hf=0
inpf=0
outf=0
```

```
!***** Main loop***************
do i=2,tend
!***** source two pulses at wc and 2wc***************
f(1,2)=EXP(-1*((i*dt-tend*dt/4)**2)/((twidth)**2))*EXP(-
ci*i*wc*dt)+f(1,2)
f(1,2)=f(1,2)+EXP(-1*((i*dt-3*tend*dt/4)**2)/((twidth)**2))*EXP(-
2*ci*i*wc*dt)
!***** Cavity differential equation *****
do j=N1,N2
sum=sum+f(1,j)
enddo
h(1,i)=h(1,i-1)+dt*(-ci*wc*h(1,i-1)-gamma*h(1,i-1)+V*sum)
!***** waveguide differential equation *****
do j=2,N
fold(1,j)=f(1,j)
enddo
do j=2,N
d=0
if (j.le.N2) then
if (j.ge.N1) then
d=1
endif
endif
f(1,j)=fold(1,j)+dt*(-ci*wo*fold(1,j)-vg*(fold(1,j)-fold(1,j-1))/dx-
d*ci*V*h(1,i))
enddo
!***** saving time outputs *****
in(1,i)=f(1,N1-1)
out(1,i)=f(1,N2+1)
```

```
time(1,i)=i*dt
enddo
!***** calculating DFT *****
!do i=1,fend
!do j=1,tend
!sum=f(1,i)
!hf(1,i)=hf(1,i)+h(1,j)*EXP(-ci*2*pi*i*dt*j*df);
!inpf(1,i)=inpf(1,i)+in(1,j)*EXP(-ci*2*pi*i*dt*j*df);
!outf(1,i)=outf(1,i)+out(1,j)*EXP(-ci*2*pi*i*dt*j*df);
!enddo
!hf(1,i)=hf(1,i)*dt/(2*pi);
!inpf(1,i)=inpf(1,i)*dt/(2*pi);
!outf(1,i)=outf(1,i)*dt/(2*pi);
!frequency(1,i)=i*df
!enddo
!***** writing output files *****
OPEN(UNIT=1, file='wc', status='unknown')
 WRITE(1,100) wc
CLOSE(1)
OPEN(UNIT=1, file='dt', status='unknown')
 WRITE(1,100) dt
CLOSE(1)
OPEN(UNIT=1, file='h', status='unknown')
do i=1,tend
 WRITE(1,100) h(1,i)
enddo
CLOSE(1)
```

```
OPEN(UNIT=1, file='in', status='unknown')
do i=1,tend
 WRITE(1,100) in(1,i)
enddo
CLOSE(1)
OPEN(UNIT=1, file='out', status='unknown')
do i=1,tend
 WRITE(1,100) out(1,i)
enddo
CLOSE(1)
OPEN(UNIT=1, file='out', status='unknown')
do i=1,tend
 WRITE(1,100) out(1,i)
enddo
CLOSE(1)
OPEN(UNIT=1, file='time', status='unknown')
do i=1,tend
 WRITE(1,100) time(1,i)
enddo
CLOSE(1)
!OPEN(UNIT=1, file='frequency', status='unknown')
!do i=1,fend
! WRITE(1,100) frequency(1,i)
!enddo
!CLOSE(1)
!OPEN(UNIT=1, file='hf', status='unknown')
!do i=1,fend
! WRITE(1,100) hf(1,i)
!enddo
```

```
!CLOSE(1)
!OPEN(UNIT=1, file='inpf', status='unknown')
!do i=1,fend
! WRITE(1,100) inpf(1,i)
!enddo
!CLOSE(1)
!OPEN(UNIT=1, file='outf', status='unknown')
!do i=1,fend
! WRITE(1,100) outf(1,i)
!enddo
!CLOSE(1)
!***** deallocate variables *****
DEALLOCATE(h)
DEALLOCATE(f)
DEALLOCATE(fold)
DEALLOCATE(in)
DEALLOCATE(out)
DEALLOCATE(time)
DEALLOCATE(frequency)
DEALLOCATE(hf)
DEALLOCATE(inpf)
DEALLOCATE(outf)
END PROGRAM
```

Appendix III

Photon Trapping (Classical CMT model Matlab)

```
clc

close all

clear all

T=0e-12;

write_step=320;

read_step=3000;

carriers=5e18;

index_change=(8.8e-22*carriers+8.5e-18*carriers^.8);

field_absorption_per_meter=.5*14.5e-18*carriers*100;

neff_out=2.4+index_change;

neff=2.4;

neff_in=2.4;

ng=4.3;

R=10E-6;

c=299792458;

dt=.5*ng*pi*R/c;

k_in=.25;

k_out=.25;

k_store=.25;

t_in=sqrt(1-k_in^2);

t_out=sqrt(1-k_out^2);

t_store=sqrt(1-k_store^2);

seperation=.5*pi*R;

lambda_res=pi*R*2.4/(49);

gamma=0;

gamma_in=0;
```

```
gamma_out=0;


time(1:4000)=0;


Ea1_in(1:4000)=0;
Eb1_in(1:4000)=0;
Ec1_in(1:4000)=0;
Ed1_in(1:4000)=0;
Ea2_in(1:4000)=0;
Eb2_in(1:4000)=0;
Ec2_in(1:4000)=0;
Ed2_in(1:4000)=0;


Ea1_out(1:4000)=0;
Eb1_out(1:4000)=0;
Ec1_out(1:4000)=0;
Ed1_out(1:4000)=0;
Ea2_out(1:4000)=0;
Eb2_out(1:4000)=0;
Ec2_out(1:4000)=0;
Ed2_out(1:4000)=0;


Ea1_r1(1:4000)=0;
Eb1_r1(1:4000)=0;
Ec1_r1(1:4000)=0;
Ed1_r1(1:4000)=0;
Ea2_r1(1:4000)=0;
Eb2_r1(1:4000)=0;
```

```
Ec2_r1(1:4000)=0;

Ed2_r1(1:4000)=0;


Ea1_r2(1:4000)=0;

Eb1_r2(1:4000)=0;

Ec1_r2(1:4000)=0;

Ed1_r2(1:4000)=0;

Ea2_r2(1:4000)=0;

Eb2_r2(1:4000)=0;

Ec2_r2(1:4000)=0;

Ed2_r2(1:4000)=0;


phase_r1=neff*(2*pi/lambda_res)*2*pi*R;

phase_r2=neff*(2*pi/lambda_res)*2*pi*R;

phase_in=neff_in*(2*pi/lambda_res)*2*pi*R;

phase_out=neff_out*(2*pi/lambda_res)*2*pi*R;


dlambda=0;

dw=c*2*pi*(1/lambda_res-1/(lambda_res-dlambda));

index_linear_shift=linspace(0,index_change,T/dt);

loss_linear_shift=linspace(0,field_absorption_per_meter,T/dt);

ss=0;

pp=0;

for tt=12:4000

 if tt>=write_step && tt<(write_step+T/dt-1)

        ss=ss+1;

        neff_in=2.40-index_linear_shift(ss);

        phase_in=neff_in*(2*pi/lambda_res)*2*pi*R;
```

```
        gamma_in=loss_linear_shift(ss)*2*pi*R;
%         gamma_in=0;
 end
     if tt>=(write_step+T/dt-1)
        neff_in=2.40-index_change;
        phase_in=neff_in*(2*pi/lambda_res)*2*pi*R;
        gamma_in=field_absorption_per_meter*2*pi*R;
%         gamma_in=0;
     end
if tt>=read_step && tt<(read_step+T/dt-1)
        pp=pp+1;
        neff_out=2.4+index_change-index_linear_shift(pp);
        phase_out=neff_out*(2*pi/lambda_res)*2*pi*R;
        gamma_out=loss_linear_shift(pp)*2*pi*R;
%         gamma_out=0;
end

   if tt>=(read_step+T/dt)
        neff_out=2.40;
        phase_out=neff_out*(2*pi/lambda_res)*2*pi*R;
        gamma_out=field_absorption_per_meter*2*pi*R;
        gamma_out=0;
    end
    Ea1_in(tt)=exp(-(tt*dt-40E-12)^2/(20E-12)^2)*exp(j*dw*tt*dt);
    Eb1_in(tt)=Ed2_in(tt-2)*exp(-gamma_in/2+j*phase_in/2);
    Ec1_in(tt)=t_in*Ea1_in(tt)+j*k_in*Eb1_in(tt);
    Ed1_in(tt)=j*k_in*Ea1_in(tt)+t_in*Eb1_in(tt);
    Ea2_in(tt)=Ec1_r1(tt-1)*exp(j*2.4*(2*pi/lambda_res)*seperation);
```

```
Eb2_in(tt)=Ed1_in(tt-2)*exp(-gamma_in/2+j*phase_in/2);
Ec2_in(tt)=t_in*Ea2_in(tt)+j*k_in*Eb2_in(tt);
Ed2_in(tt)=j*k_in*Ea2_in(tt)+t_in*Eb2_in(tt);


Ea1_r1(tt)=0;
Eb1_r1(tt)=Ed2_r1(tt-2)*exp(-gamma/2+j*phase_r1/2);
Ec1_r1(tt)=t_store*Ea1_r1(tt)+j*k_store*Eb1_r1(tt);
Ed1_r1(tt)=j*k_store*Ea1_r1(tt)+t_store*Eb1_r1(tt);
Ea2_r1(tt)=Ec1_out(tt-1)*exp(.5*j*2.4*(2*pi/lambda_res)*pi*R);
Eb2_r1(tt)=Ed1_r1(tt-2)*exp(-gamma/2+j*phase_r1/2);
Ec2_r1(tt)=t_store*Ea2_r1(tt)+j*k_store*Eb2_r1(tt);
Ed2_r1(tt)=j*k_store*Ea2_r1(tt)+t_store*Eb2_r1(tt);



Ea1_out(tt)=Ec2_r2(tt-1)*exp(.5*j*2.4*(2*pi/lambda_res)*pi*R);
Eb1_out(tt)=Ed2_out(tt-2)*exp(-gamma_out/2+j*phase_out/2);
Ec1_out(tt)=t_out*Ea1_out(tt)+j*k_out*Eb1_out(tt);
Ed1_out(tt)=j*k_out*Ea1_out(tt)+t_out*Eb1_out(tt);
Ea2_out(tt)=0;
Eb2_out(tt)=Ed1_out(tt-2)*exp(-gamma_out/2+j*phase_out/2);
Ec2_out(tt)=t_out*Ea2_out(tt)+j*k_out*Eb2_out(tt);
Ed2_out(tt)=j*k_out*Ea2_out(tt)+t_out*Eb2_out(tt);



Ea1_r2(tt)=Ec2_in(tt-1)*exp(.5*j*2.4*(2*pi/lambda_res)*pi*R);
Eb1_r2(tt)=Ed2_r2(tt-2)*exp(-gamma/2+j*phase_r2/2);
Ec1_r2(tt)=t_store*Ea1_r2(tt)+j*k_store*Eb1_r2(tt);
Ed1_r2(tt)=j*k_store*Ea1_r2(tt)+t_store*Eb1_r2(tt);
```

```
    Ea2_r2(tt)=0;
    Eb2_r2(tt)=Ed1_r2(tt-2)*exp(-gamma/2+j*phase_r2/2);
    Ec2_r2(tt)=t_store*Ea2_r2(tt)+j*k_store*Eb2_r2(tt);
    Ed2_r2(tt)=j*k_store*Ea2_r2(tt)+t_store*Eb2_r2(tt);

    time(tt)=dt*tt;
end

plot(time*1e12,Ea1_in.*conj(Ea1_in),'b')
hold on
plot(time*1e12,Ec1_r1.*conj(Ec1_r1),'r')
plot(time*1e12,Ec2_out.*conj(Ec2_out),'g')

legend('Blue representts tthe input signal','Red representts tthe
sttored signal','Green representts tthe outputt signal')
xlabel('time in picoseconds')
ylabel('Inttensitty a.u.')
figure
hold on
c=299792458;
S1=fft(Ea1_in,16*2048);
f=[-16*2048/2:(16*2048/2-1)]*1/(16*dt*2048);
S1=fftshift(S1);
S1=abs(S1).^2;
S2=fft(Ec1_r1(write_step:read_step),16*2048);
f=[-16*2048/2:(16*2048/2-1)]*1/(16*dt*2048);
S2=fftshift(S2);
S2=abs(S2).^2;
```

```
norm=max(S1);
S3=fft(Ec2_out(read_step:4000),16*2048);
f=[-16*2048/2:(16*2048/2-1)]*1/(16*dt*2048);
S3=fftshift(S3);
S3=abs(S3).^2;
plot(f,S1/norm,'b',f,S2/norm,'r',f,S3/norm,'g')
legend('Blue representts tthe input signal','Red representts tthe
sttored signal','Green representts tthe outputt signal')
xlabel(' frequency in Hz')
ylabel(' power spectrum normalized to the input power')
axis([-1e10 1e10 0 max([S1 S2 S3])/norm])
```

REFERENCES

[1] T. Baba, "Slow light in photonic crystals," *Nature Photonics*, vol. 2, Aug. 2008, pp. 465-473.

[2] L.H. Frandsen, P.I. Borel, Y.X. Zhuang, a Harpøth, M. Thorhauge, M. Kristensen, W. Bogaerts, P. Dumon, R. Baets, V. Wiaux, J. Wouters, and S. Beckx, "Ultralow-loss 3-dB photonic crystal waveguide splitter.," *Optics letters*, vol. 29, Jul. 2004, pp. 1623-5.

[3] T. Baehr-Jones, M. Hochberg, C. Walker, and A. Scherer, "High-Q ring resonators in thin silicon-on-insulator," *Applied Physics Letters*, vol. 85, 2004, p. 3346.

[4] J. Niehusmann, A. Vörckel, P.H. Bolivar, T. Wahlbrink, and W. Henschel, "Ultrahigh-quality-factor silicon-on-insulator microring resonator," *Optics Letters*, vol. 29, 2004, pp. 2861-2863.

[5] C.A. Barrios, Q. Xu, J. Shakya, C. Manolatou, and M. Lipson, "Compact silicon slot-waveguide disk resonator," *CLEO*, 2006, pp. 2-3.

[6] R. Hao, E. Cassan, H. Kurt, X. Le Roux, D. Marris-Morini, L. Vivien, H. Wu, Z. Zhou, and X. Zhang, "Novel slow light waveguide with controllable delay-bandwidth product and utra-low dispersion," *Optics Express*, vol. 18, Mar. 2010, p. 5942.

[7] T.F. Krauss, "Slow light in photonic crystal waveguides," *Journal of Physics D: Applied Physics*, vol. 40, 2007, pp. 2666-2670.

[8] N. Sherwood-droz, H. Wang, L. Chen, B.G. Lee, K. Bergman, and M. Lipson, "Optical 4x4 hitless silicon router for optical Networks-on-Chip (NoC)," *Optics Express*, vol. 16, 2008, pp. 1-3.

[9] G. Ghosh, *Handbook of thermo-optic coefficients of optical materials with applications*, Academic Press,, 1998.

[10] V.R. Almeida and M. Lipson, "Optical bistability on a silicon chip.," *Optics letters*, vol. 29, Oct. 2004, pp. 2387-9.

[11] Q. Lin, O.J. Painter, and G.P. Agrawal, "Nonlinear optical phenomena in silicon waveguides: modeling and applications.," *Optics express*, vol. 15, Dec. 2007, pp. 16604-44.

[12] P.N. Butcher and D. Cotter, *The Elements of Nonlinear Optics*, New York: Cambridge University Press, 1991.

[13] O. Boyraz, T. Indukuri, and B. Jalali, "Self-phase-modulation induced spectral broadening in silicon waveguides," *Opt. Express*, vol. 12, 2004, pp. 829-834.

[14] P.K. Boyraz, V. Raghunathan, and B. Jalali, "All optical switching and continuum generation in silicon 25," *O. waveguides, Opt. Express*, vol. 12, 2004, pp. 4094-4102.

[15] R. Dekker, A. Driessen, T. Wahlbrink, C. Moormann, J. Niehusmann, and M.F. Orst, "Ultrafast Kerr-induced all-optical wavelength conversion in silicon waveguides using 1.55 μ m femtosecond pulses," *Opt. Express*, vol. 14, 2006, pp. 8336-8346.

[16] Q. Xu, "Controlling The Flow of Light on Chip With Microresonator- Based Silicon Photonic Devices," Cornell, 2007.

[17] R. Jacobsen, K. Andersen, P. Borel, J. Fage-pedersen, L. Frandsen, O. Hansen, M. Kristensen, A. Lavrinenko, G. Moulin, H. Ou, C. Peucheret, B. Zsigri, and A. Bjarklev, "Strained silicon as a new electro-optic material," *Nature*, vol. 441, 2006.

[18] R.A. Soref and B.R. Bennett, "Kramers-Kronig analysis of E-O switching in silicon," *SPIE Integrated Optical. Circuit Engineering*, vol. 704, 1986.

[19] C.A. Barrios, V.R. Almeida, and M. Lipson, "Low-power-consumption short-length and high-modulation-depth silicon electrooptic modulator," *IEEE journal of Lightwave Technology*, vol. 21, 2003, pp. 1089-98.

[20] C.A. Barrios, V. Almeida, R. Panepucci, and M. Lipson, "Electrooptic modulation of silicon-on-insulator submicrometer size waveguide devices," *IEEE journal of Lightwave Technology*, vol. 21, 2003, pp. 2332-2339.

[21] C.A. Barrios, "Electrooptic Modulation of multisilicon-on-insulator Photonic Wires," *Lightwave Technology*, vol. 24, 2006, pp. 2146-2155.

[22] W.M. Green, M.J. Rooks, L. Sekaric, and Y. a Vlasov, "Ultra-compact, low RF power, 10 Gb/s silicon Mach-Zehnder modulator.," *Optics express*, vol. 15, Dec. 2007, pp. 17106-13.

[23] N.K. Hon, L. Zhou, and A.W. Poon, "Silicon depletion-type microdisk electro-optic modulators using selectively integrated Schottky diodes," *CLEO*, 2007, pp. 22-23.

[24] S. Manipatruni, Q. Xu, B. Schmidt, J. Shakya, and M. Lipson, "High speed carrier injection 18 Gb/s silicon micro-ring electro-optic modulator," *LEOS*, 2007, pp. 537-538.

[25] G.V. Treyz and P.G. May, "Silicon optical modulators at 1.3 μm based on free-carrier absorption," *IEEE Electron Device Letters*, vol. 12, 1991, pp. 276-278.

[26] M.R. Watts, D.C. Trotter, and R.W. Young, "Maximally Confined High-Speed Second-Order Silicon Microdisk Switches," *OFC*, 2008, pp. 15-17.

[27] Q. Xu, B. Schmidt, S. Pradhan, and M. Lipson, "Micrometre-scale silicon electro-optic modulator.," *Nature*, vol. 435, 2005, pp. 325-7.

[28] Q.F. Xu, P. Dong, and M. Lipson, "Breaking the delay-bandwidth limit in a photonic structure," *Nature Phys.*, vol. 3, 2007, pp. 406-410.

[29] S. Sandhu, M.L. Povinelli, and S. Fan, "Stopping and time reversing a light pulse using dynamic loss tuning of coupled-resonator delay lines," *Optics Letters*, vol. 32, 2007, pp. 3333-3335.

[30] M. Notomi and S. Mitsugi, "Wavelength conversion via dynamic refractive index tuning of a cavity," *Phys. Rev. A*, vol. 73, 2006, p. 051803.

[31] T.J. Johnson, M. Borselli, and O. Painter, "Self-induced optical modulation of the transmission through a high-Q silicon microdisk resonator.," *Optics express*, vol. 14, Jan. 2006, pp. 817-31.

[32] S.F. Preble, Q. Xu, and M. Lipson, "Changing the colour of light in a silicon resonator," *Nature Photonics*, vol. 1, 2007, pp. 293-296.

[33] Z. Gaburro, M. Ghulinyan, F. Riboli, L. Pavesi, A. Recati, and I. Carusotto, "Photon energy lifter," *Opt. Express*, vol. 14, 2006, pp. 7270-7278.

[34] Z. Yu and S. Fan, "Complete optical isolation created by indirect interband photonic transitions," *Nature Photonics*, vol. 3, 2009.

[35] A. Liu, L. Liao, D. Rubin, H. Nguyen, B. Ciftcioglu, Y. Chetrit, N. Izhaky, and M. Paniccia, "High-speed optical modulation based on carrier depletion in a silicon waveguide," *Optics Express*, vol. 15, 2007, pp. 660-668.

[36] N.M. Wright, D.J. Thomson, K.L. Litvinenko, W.R. Headley, a J. Smith, a P. Knights, J.H.B. Deane, F.Y. Gardes, G.Z. Mashanovich, R. Gwilliam, and G.T. Reed, "Free carrier lifetime modification for silicon waveguide based devices.," *Optics express*, vol. 16, Nov. 2008, pp. 19779-84.

[37] A.C. Turner-Foster, M. a Foster, J.S. Levy, C.B. Poitras, R. Salem, A.L. Gaeta, and M. Lipson, "Ultrashort free-carrier lifetime in low-loss silicon nanowaveguides," *Optics Express*, vol. 18, Feb. 2010, p. 3582.

[38] S.F. Preble, Q. Xu, B.S. Schmidt, and M. Lipson, "Ultrafast all-optical modulation on a silicon chip," *Optics letters*, vol. 30, 2005, pp. 2891-2893.

[39] J.E. Heebner, "Nonlinear Optical Whispering Gallery Microresonators for Photonics by," University ofRochester, 2003.

[40] A. Yariv, "Universal relations for coupling of optical power between microresonators and dielectric waveguides," *Electron. Lett.*, vol. 36, 2000, pp. 321-322.

[41] M.S. Dennis, *Electromagnetic Simulation Using the FDTD Method*, New york: IEEE press, 2000.

[42] J.L. O'Brien, A. Furusawa, and J. Vuckovic, "Photonic quantum technologies," *Nature Photonics*, vol. 3, 2009, pp. 687 - 695.

[43] S. Clemmen, K. Phan Huy, W. Bogaerts, R.G. Baets, P. Emplit, and S. Massar, "Continuous wave photon pair generation in silicon-on-insulator waveguides and ring resonators.," *Optics express*, vol. 17, Sep. 2009, pp. 16558-70.

[44] M.A. Nielsen and I.L. Chuang, *Quantum Computation and Quantum Information*, Cambridge University Press, 2000.

[45] W. Tittel, J. Brendel, H. Zbinden, and N. Gisin, "Quantum cryptography using entangled photons in energy-time bell states," *Physical review letters*, vol. 84, May. 2000, pp. 4737-40.

[46] T. Nagata, R. Okamoto, J.L. O'brien, K. Sasaki, and S. Takeuchi, "Beating the standard quantum limit with four-entangled photons.," *Science (New York, N.Y.)*, vol. 316, May. 2007, pp. 726-9.

[47] B.L. Higgins, D.W. Berry, S.D. Bartlett, H.M. Wiseman, and G.J. Pryde, "Entanglement-free Heisenberg-limited phase estimation.," *Nature*, vol. 450, Nov. 2007, pp. 393-6.

[48] Y. Kawabe, H. Fujiwara, R. Okamoto, K. Sasaki, and S. Takeuchi, "Quantum interference fringes beating the diffraction limit.," *Optics express*, vol. 15, Oct. 2007, pp. 14244-50.

[49] an Boto, P. Kok, D. Abrams, S. Braunstein, C. Williams, and J. Dowling, "Quantum interferometric optical lithography: exploiting entanglement to beat the diffraction limit," *Physical review letters*, vol. 85, Sep. 2000, pp. 2733-6.

[50] J.L. O'Brien, "Optical quantum computing.," *Science (New York, N.Y.)*, vol. 318, Dec. 2007, pp. 1567-70.

[51] E. Knill, R. Laflamme, and G.J. Milburn, “A scheme for efficient quantum computation with linear optics.,” *Nature*, vol. 409, Jan. 2001, pp. 46-52.

[52] J.-T. Shen and S. Fan, “Theory of single-photon transport in a single-mode waveguide. I. Coupling to a cavity containing a two-level atom,” *Physical Review A*, vol. 79, 2009, pp. 1-11.

[53] J.-T. Shen and S. Fan, “Theory of single-photon transport in a single-mode waveguide. II. Coupling to a whispering-gallery resonator containing a two-level atom,” *Physical Review A*, vol. 79, 2009.

[54] M. Notomi, T. Tanabe, E. Kuramochi, A. Shinya, and H. Taniyama, “Photonic Crystal Nanocavities : Slow Light , All-optical Processing , Wavelength Conversion , Optical MEMS,” *Group IV Photonics*, 2007.

[55] A.W. Elshaari, A. Aboketaf, and S.F. Preble, “Controlled storage of light in silicon cavities.,” *Optics express*, vol. 18, Mar. 2010, pp. 3014-22.

[56] M.F. Yanik and S. Fan, “Slow light: Dynamic photon storage,” *Nature Phys.*, vol. 3, 2007, pp. 3-5.

[57] Y. Takahashi, H. Hagino, Y. Tanaka, B.S. Song, T. Asano, and S. Noda, “High-Q nanocavity with a 2-ns photon lifetime,” *Optics Express*, vol. 15, 2007, pp. 17206-17213.

[58] J.J. Sakurai, *Modern Quantum Mechanics*, Addison Wesley Longman, 1994.

[59] J.-T. Shen and S. Fan, “Strongly correlated multiparticle transport in one dimension through a quantum impurity,” *Physical Review A*, vol. 76, Dec. 2007.

[60] C.R. Otey, M.L. Povinelli, and S. Fan, “Capturing light pulses into a pair of coupled photonic crystal cavities,” *Applied Physics Letters*, vol. 94, 2009, p. 231109.

[61] J.H. Mathews, *Complex Variables for Mathematics and Engineering*, Wm. C. Brown Publishers, 1988.

[62] A. Taflove and S. Hagness, *Computational Electrodynamics:*, Artech House Publishers, 2005.

[63] B. Lounis and M. Orrit, “Single-photon sources,” *Reports on Progress in Physics*, vol. 68, 2005, pp. 1129-1179.

[64] N.S. Malik, M. Bazin, N. Gregersen, C. Sauvan, P. Lalanne, and J.-michel Ge, “A highly efficient single-photon source based on a quantum dot in a photonic nanowire,” *Nature Photonics*, vol. 4, 2010, pp. 174-177.

[65] H. Fukuda, K. Yamada, T. Shoji, M. Takahashi, T. Tsuchizawa, T. Watanabe, J.-ichi Takahashi, and S.-ichi Itabashi, "Four-wave mixing in silicon wire waveguides," *Opt. Express*, vol. 13, 2005, pp. 4629-4637.

[66] K.-ichi Harada, H. Takesue, H. Fukuda, T. Tsuchizawa, T. Watanabe, K. Yamada, Y. Tokura, and S.-ichi Itabashi, "Generation of high-purity entangled photon pairs using silicon wire waveguide.," *Optics express*, vol. 16, Dec. 2008, pp. 20368-73.

[67] A.C. Turner, M.A. Foster, A.L. Gaeta, and M. Lipson, "Ultra-low power parametric frequency conversion in a silicon microring resonator," *Opt. Express*, vol. 16, 2008, pp. 4881-4887.

[68] M. Ferrera, D. Duchesne, L. Razzari, M. Peccianti, R. Morandotti, P. Cheben, S. Janz, D.-X. Xu, B.E. Little, S. Chu, and D.J. Moss, "Low power four wave mixing in an integrated, micro-ring resonator with Q = 1.2 million.," *Optics express*, vol. 17, Aug. 2009, pp. 14098-103.

[69] L.G. Helt, Z. Yang, M. Liscidini, and J.E. Sipe, "Spontaneous four-wave mixing in microring resonators.," *Optics letters*, vol. 35, Sep. 2010, pp. 3006-8.

[70] S. Zotter, J. Kofler, T. Jennewein, and A. Zeilinger, "Towards on-demand single-photon generation via active multiplexing," *Quantum optics*, 2010, pp. 1-8.

[71] I. Marcikic, H. de Riedmatten, W. Tittel, H. Zbinden, M. Legré, and N. Gisin, "Distribution of Time-Bin Entangled Qubits over 50 km of Optical Fiber," *Physical Review Letters*, vol. 93, 2004, pp. 1-4.

[72] X. Li, P. Voss, J. Sharping, and P. Kumar, "Optical-Fiber Source of Polarization-Entangled Photons in the 1550 nm Telecom Band," *Physical Review Letters*, vol. 94, 2005, pp. 9-12.

[73] H. Search, C. Journals, A. Contact, M. Iopscience, C. Phys, T. Table, and I.P. Address, "A scheme for demonstration of four-photon," *IOP science*, vol. 3549, 2008.

[74] G. Gilbert, M. Hamrick, and Y.S. Weinstein, "Use of maximally entangled N-photon states for practical quantum interferometry," *JOSA B*, vol. 25, 2008, pp. 1336-1340.

[75] David J. Griffith, *Introduction to Quantum Mechanics*, Prentice Hall, .

[76] P. Dong, S. Preble, J. Robinson, S. Manipatruni, and M. Lipson, "Inducing Photonic Transitions between Discrete Modes in a Silicon Optical Microcavity," *Physical Review Letters*, vol. 100, Jan. 2008, pp. 1-4.

[77] B. Julsgaard, J. Sherson, J.I. Cirac, J. Fiurásek, and E.S. Polzik, "Experimental demonstration of quantum memory for light.," *Nature*, vol. 432, Nov. 2004, pp. 482-6.

[78] A. Politi, M.J. Cryan, J.G. Rarity, S. Yu, and J.L. O'Brien, "Silica-on-silicon waveguide quantum circuits.," *Science*, vol. 320, 2008, pp. 646-9.

[79] C.A. Barrios, R.R. Panepucci, and M. Lipson, with Michal Lipson, "All-optical control of light on a silicon chip," *October*, vol. 431, 2004, pp. 1081-1084.

[80] T. Tanabe, M. Notomi, S. Mitsugi, A. Shinya, and E. Kuramochi, "All-optical switches on a silicon chip realized using photonic crystal nanocavities," *Applied Physics Letters*, vol. 87, 2005, p. 151112.

[81] N. Stefanou and A. Modinos, "Impurity bands in photonic insulators," *Physical Review B*, vol. 57, 1998, pp. 127-133.

[82] a Yariv, Y. Xu, R.K. Lee, and a Scherer, "Coupled-resonator optical waveguide: a proposal and analysis.," *Optics letters*, vol. 24, Jun. 1999, pp. 711-3.

[83] F. Xia, L. Sekaric, M. O'Boyle, and Y. Vlasov, "Coupled resonator optical waveguides based on silicon-on-insulator photonic wires," *Applied Physics Letters*, vol. 89, 2006, p. 041122.

[84] D. O'Brien, a Gomez-Iglesias, M. Settle, a Michaeli, M. Salib, and T. Krauss, "Tunable optical delay using photonic crystal heterostructure nanocavities," *Physical Review B*, vol. 76, 2007, pp. 2-5.

[85] J. Upham, Y. Tanaka, T. Asano, and S. Noda, "Dynamic increase and decrease of photonic crystal nanocavity Q factors for optical pulse control.," *Optics express*, vol. 16, Dec. 2008, pp. 21721-30.

[86] X. Yang, M. Yu, D.-L. Kwong, and C. Wong, "All-Optical Analog to Electromagnetically Induced Transparency in Multiple Coupled Photonic Crystal Cavities," *Physical Review Letters*, vol. 102, 2009, pp. 1-4.

[87] C. Manolatou, M.J. Khan, S. Fan, P.R. Villeneuve, H.A. Haus, and J.D. Joannopoulos, "Coupling of modes analysis of resonant channel add-drop filters," *Quantum Electron.*, vol. 35, 1999, pp. 1322-1331.

[88] Q. Xu, S. Manipatruni, B. Schmidt, J. Shakya, and M. Lipson, "12.5 Gbit/s carrier-injection-based silicon micro-ring silicon modulators," *Optics Express*, vol. 15, 2007.

[89] A.W. Elshaari and S.F. Preble, "Active Optical Isolator Using Adiabatic Wavelength Conversion in Microcavities," *FIO*, 2009, pp. 3-4.

[90] C.R. Otey, M.L. Povinelli, S. Fan, and S. Member, “Completely Capturing Light Pulses in a Few Dynamically Tuned Microcavities,” *IEEE journal of Lightwave Technology*, vol. 26, 2009, pp. 3784-3793.

[91] A.W. Elshaari and S.F. Preble, “Nanosecond Tunable Optical Delay using Silicon Cavities,” *FIO*, 2009, pp. 3-4.

[92] J. Cardenas, C.B. Poitras, J.T. Robinson, K. Preston, L. Chen, and M. Lipson, “Low loss etchless silicon photonic waveguides.,” *Optics express*, vol. 17, Mar. 2009, pp. 4752-7.

[93] T. Tanabe, M. Notomi, E. Kuramochi, and H. Taniyama, “Large pulse delay and small group velocity achieved using ultrahigh-Q photonic crystal nanocavities.,” *Optics express*, vol. 15, Jun. 2007, pp. 7826-39.

[94] Z. Gaburro, M. Ghulinyan, F. Riboli, L. Pavesi, A. Recati, and I. Carusotto, “Photon energy lifter.,” *Optics express*, vol. 14, Aug. 2006, pp. 7270-8.

[95] Q. Xu, S. Sandhu, M. Povinelli, J. Shakya, S. Fan, and M. Lipson, “Experimental Realization of an On-Chip All-Optical Analogue to Electromagnetically Induced Transparency,” *Physical Review Letters*, vol. 96, 2006, pp. 1-4.

[96] J.N. Winn, S. Fan, J.D. Joannopoulos, and E.P. Ippen, “Interband transitions in photonic crystals,” *Physical Review B*, vol. 59, 1999, pp. 1551-1554.

[97] A. Khorshidahmad and A.G. Kirk, “Wavelength conversion by dynamically reconfiguring a nested photonic crystal cavity.,” *Optics express*, vol. 18, Apr. 2010, pp. 7732-42.

[98] E. Hach, A. Elshaari, and S. Preble, “Fully quantum-mechanical dynamic analysis of single-photon transport in a single-mode waveguide coupled to a traveling-wave resonator,” *Physical Review A*, vol. 82, Dec. 2010, pp. 1-10.

[99] J. Poon, J. Scheuer, S. Mookherjea, G. Paloczi, Y. Huang, and A. Yariv, “Matrix analysis of microring coupled-resonator optical waveguides.,” *Optics express*, vol. 12, Jan. 2004, pp. 90-103.

[100] A. Taflove and S. Hagness, *Computational Electrodynamics: The Finite-Difference Time-Domain Method*, Artech House Publishers, 2000.

[101] Y. Shoji, H. Yokoi, I.-W. Hsieh, R.M. Osgood, and T. Mizumoto, “Magneto-optical isolator with SOI waveguide,” *OFC/NFOEC 2008 - 2008 Conference on Optical Fiber Communication/National Fiber Optic Engineers Conference*, Feb. 2008, pp. 1-3.

[102] M.W. McCutcheon, A.G. Pattantyus-Abraham, G.W. Rieger, and J.F. Young, "Emission spectrum of electromagnetic energy stored in a dynamically perturbed optical microcavity.," *Optics express*, vol. 15, Sep. 2007, pp. 11472-80.

[103] S. Fan, M.F. Yanik, Z. Wang, S. Sandhu, and M.L. Povinelli, "Advances in Theory of Photonic Crystals," *Journal of Lightwave Technology*, vol. 24, Dec. 2006, pp. 4493-4501.

[104] M. Li, W.H.P. Pernice, C. Xiong, T. Baehr-Jones, M. Hochberg, and H.X. Tang, "Harnessing optical forces in integrated photonic circuits.," *Nature*, vol. 456, 2008, pp. 480-4.

[105] G. Al, O.S. Waveguides, D.J. Ripin, K.-yi Lim, G.S. Petrich, P.R. Villeneuve, S. Fan, E.R. Thoen, S. Member, and J.D. Joannopoulos, "One-Dimensional Photonic Bandgap Microcavities for Strong Optical Confinement in GaAs and," *Journal of Lightwave Technology*, vol. 17, 1999, pp. 2152-2160.

[106] B. Schmidt, Q. Xu, J. Shakya, S. Manipatruni, and M. Lipson, "Compact electro-optic modulator on silicon-on-insulator substrates using cavities with ultra-small modal volumes.," *Optics express*, vol. 15, Mar. 2007, pp. 3140-8.

[107] P. Dong, S. Liao, D. Feng, H. Liang, and D. Zheng, "Low Vpp, ultralow-energy, compact, high-speed silicon electro-optic modulator," *Optics Express*, vol. 17, 2009, pp. 22484-22490.

[108] S. Manipatruni, R.K. Dokania, B. Schmidt, N. Sherwood-Droz, C.B. Poitras, A.B. Apsel, and M. Lipson, "Wide temperature range operation of micrometer-scale silicon electro-optic modulators.," *Optics letters*, vol. 33, Oct. 2008, pp. 2185-7.

[109] Y. Vlasov, W.M.J. Green, and F. Xia, "High-throughput silicon nanophotonic wavelength-insensitive switch for on-chip optical networks," *Nature Photonics*, vol. 2, 2008, pp. 242-246.

[110] D.W. Zheng, B.T. Smith, and M. Asghari, "Improved efficiency Si-photonic attenuator.," *Optics express*, vol. 16, Oct. 2008, pp. 16754-65.

[111] J. Liu, M. Beals, A. Pomerene, S. Bernardis, R. Sun, J. Cheng, L.C. Kimerling, and J. Michel, "Waveguide-integrated, ultralow-energy GeSi electro-absorption modulators," *Nature Photonics*, vol. 2, 2008, pp. 433-437.

[112] "www.Silvaco.com."

[113] J.T. Robinson, K. Preston, O. Painter, and M. Lipson, "First-principle derivation of gain in high-index-contrast waveguides.," *Optics express*, vol. 16, Oct. 2008, pp. 16659-69.

[114] B.H.A. Saleh and M.C. Teich, *Fundamelntals of photonics*, Wiley, 2007.

[115] T. Barwicz, M.R. Watts, M. a Popović, P.T. Rakich, L. Socci, F.X. Kärtner, E.P. Ippen, and H.I. Smith, "Polarization-transparent microphotonic devices in the strong confinement limit," *Nature Photonics*, vol. 1, 2007, pp. 57-60.

[116] W. Zhang, S.H. Brongersma, O. Richard, B. Brijs, R. Palmans, L. Froyen, and K. Maex, "Influence of the electron mean free path on the resistivity of thin metal films," *Microelectronic Engineering*, vol. 76, 2004, pp. 146-152.

[117] Y. Vlasov and S. Mcnab, "Losses in single-mode silicon-on-insulator strip waveguides and bends," *Optics Express*, vol. 12, 2004, pp. 1622-1631.

[118] B.G. Lee, S. Member, A. Biberman, P. Dong, M. Lipson, K. Bergman, and S. Member, "All-Optical Comb Switch for Multiwavelength Message Routing in Silicon Photonic Networks," *IEEE photonics technology letters*, vol. 20, 2008, pp. 767-769.